

**TESTBED IMPLEMENTATION OF A MIMO-OFDM DATA LINK AT SUB 6
GHz FREQUENCY BANDS USING AN SDR PLATFORM**

A THESIS SUBMITTED TO
THE GRADUATE SCHOOL OF NATURAL AND APPLIED SCIENCES
OF
MIDDLE EAST TECHNICAL UNIVERSITY

BY

UFUK TAMER

IN PARTIAL FULFILLMENT OF THE REQUIREMENTS
FOR
THE DEGREE OF MASTER OF SCIENCE
IN
ELECTRICAL AND ELECTRONICS ENGINEERING

AUGUST 2018

Approval of the thesis:

**TESTBED IMPLEMENTATION OF A MIMO-OFDM DATA LINK AT SUB 6
GHz FREQUENCY BANDS USING AN SDR PLATFORM**

submitted by **UFUK TAMER** in partial fulfillment of the requirements for the degree of **Master of Science in Electrical and Electronics Engineering Department, Middle East Technical University** by,

Prof. Dr. Halil Kalıپçilar _____
Dean, Graduate School of **Natural and Applied Sciences**

Prof. Dr. Tolga Çiloğlu _____
Head of Department, **Electrical and Electronics Engineering**

Prof. Dr. Ali Özgür Yılmaz _____
Supervisor, **Electrical and Electronics Eng. Dept., METU**

Examining Committee Members:

Prof. Dr. Yalçın Tanık _____
Electrical and Electronics Engineering Department, METU

Prof. Dr. Ali Özgür Yılmaz _____
Electrical and Electronics Engineering Department, METU

Assist. Prof. Dr. Gökhan Muzaffer Güvensen _____
Electrical and Electronics Engineering Department, METU

Prof. Dr. Buyurman Baykal _____
Electrical and Electronics Engineering Department, METU

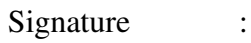
Prof. Dr. Erdal Arıkan _____
Electrical and Electronics Engineering Dept., Bilkent University

Date:

August 9, 2018

I hereby declare that all information in this document has been obtained and presented in accordance with academic rules and ethical conduct. I also declare that, as required by these rules and conduct, I have fully cited and referenced all material and results that are not original to this work.

Name, Last Name: UFUK TAMER

Signature : 

ABSTRACT

TESTBED IMPLEMENTATION OF A MIMO-OFDM DATA LINK AT SUB 6 GHz FREQUENCY BANDS USING AN SDR PLATFORM

Tamer, Ufuk

M.S., Department of Electrical and Electronics Engineering

Supervisor : Prof. Dr. Ali Özgür Yılmaz

August 2018, 102 pages

Studies in recent years concentrate on multiple input multiple output (MIMO) systems because of spectral efficiency and diversity advantages. In MIMO systems, a technique called orthogonal frequency division multiplexing (OFDM) is highly preferred since it turns wideband frequency selective channel into narrowband flat channels. Hence, the signal can be represented in time, frequency, and space with MIMO-OFDM. This brings a huge advantage on both multiplexing and diversity. Because of its popularity in the last decade, people are studying various algorithms for MIMO-OFDM systems and they always need a testbed platform in order to test and validate the algorithms in a real environment. In this study, a testbed for MIMO-OFDM data link is implemented by using software defined radio (SDR) devices working at sub-6 GHz.

First, a physical layer (PHY) for MIMO-OFDM data link is designed including various synchronization, estimation, equalization, and detection algorithms. Additionally, a MIMO-OFDM simulator is implemented in MATLAB in order to test and

verify the performance of PHY in different channel conditions also by taking into account some RF impairments that are modeled in simulation environment.

Second, a MIMO-OFDM testbed is implemented with SDR devices. For transmit signal generation and demodulation operations our MATLAB simulator is used. However, for signal transmission and acquisition with SDRs, GNU Radio software is used in Python environment. Tests have been carried out at 3.5 GHz which is the foremost candidate frequency band in 5G standard. Our MIMO-OFDM data link PHY has been tested in various places including indoor and outdoor environments. Also, the channel at 3.5 GHz was measured for SISO and 2×2 MIMO scenarios in both indoor and outdoor environments. The characterization of the channel in static and dynamic conditions is investigated and discussed.

Keywords: MIMO, OFDM, SDR, testbed, data link, channel analysis

ÖZ

6 GHz ALTI FREKANS BANTLARI İÇİN SDR TABANLI MIMO-OFDM VERİ BAĞI TEST ORTAMI GERÇEKLEMESİ

Tamer, Ufuk

Yüksek Lisans, Elektrik ve Elektronik Mühendisliği Bölümü

Tez Yöneticisi : Prof. Dr. Ali Özgür Yılmaz

Ağustos 2018 , 102 sayfa

Son yıllarda yapılan çalışmalar spektral verimlilik veçeşitleme avantajları sayesinde çok girdili çok çıktılı (MIMO) sistemlerinde yoğunlaşmıştır. MIMO sistemlerinde, dikey frekans bölmeli çoklama (OFDM) teknigi genişbant frekans seçmeli kanalı darbant düz kanallara dönüştürdüğü için oldukça tercih edilen bir modülasyondur. Böylece, MIMO-OFDM ile sinyal zaman, frekans ve uzayda temsil edilebilmektedir. Bu durum çoğullama veçeşitleme üzerinde büyük bir avantaj getirir. Son on yıl içe-risinde MIMO-OFDM sistemlerinin popüler olması sebebiyle bu sistemler için farklı algoritmalar çalışılmakta ve gerçek ortamda test edilip doğrulanması için test ortamlarına ihtiyaç duyulmaktadır. Bu çalışmada 6-GHz altı frekans bandında çalışan SDR tabanlı bir MIMO-OFDM veri bağı test ortamı gerçeklenmiştir.

İlk olarak, MIMO-OFDM veri bağına ait, çeşitli senkronizasyon, kestirim, denkleş-tirme ve sezim algoritmaları içeren bir fiziksel katman (PHY) tasarlanmıştır. Ayrıca, farklı kanal koşullarında simülasyon ortamında modellenen bazı RF bozulmalarını da dikkate alarak PHY başarısını test etmek ve doğrulamak için MATLAB programında

bir MIMO-OFDM simülatörü gerçekleştirmiştir.

İkinci olarak, SDR cihazları kullanılarak bir MIMO-OFDM test ortamı gerçeklenmiştir. Sinyal üretimi ve demodülasyon işlemleri için MATLAB simülatörümüz kullanılmıştır. SDR'lar ile sinyal iletimi ve kayıt işlemleri için ise GNU Radio yazılımı Python ortamında kullanılmıştır. Testler 5G standardizasyonunda onde gelen aday frekans bantlarından 3.5 GHz'de gerçekleştirilmiştir. Tasarladığımız MIMO-OFDM veri bağı fiziksel katmanı kapalı ve açık olmak üzere farklı ortamlarda test edilmişdir. Ayrıca, 3.5 GHz frekans bandındaki kanal SISO ve 2×2 MIMO senaryoları için kapalı ve açık alanlarda ölçülmüştür. Kanalın durgun ve hareketli durumlardaki karakterizasyonu incelenmiştir ve tartışılmıştır.

Anahtar Kelimeler: MIMO (Çok Girdili Çok Çıktılı), OFDM (Dikey Frekans Bölmeli Çoklama), SDR (Yazılım Tanımlı Rado), veri bağı, kanal analizi

to my family

"ipse se nihil scire id unum sciat"

Socrates

ACKNOWLEDGMENTS

Foremost, I would like to express my special thanks to Prof. Ali Özgür Yılmaz not only for his smart ideas, wisdom and support but also his friendly attitude throughout this study. It was a great opportunity for me to work with him both in academia and industry. Without his guidance, I would not have such a career.

I would like to thank my thesis committee members: Prof. Yalçın Tanık, Asist. Prof. Gökhan Muzaffer Güvensen, Prof. Buyurman Baykal and Prof. Erdal Arıkan for their advisable comments and suggestions.

I would like to thank my previous company Anketek for providing a great working environment and also supporting me during this thesis. Besides, I thank Mehmet Ali Öztürk who manufactured the antennas for this study.

I would also like to thank my current company SDT for supporting my thesis study especially with measurement equipment and test environments. I am also thankful to my colleagues Mehmet Kabasakal, Türker Dolapçı, Handan Ağırman and Serkan Karakütük for their valuable comments and continuous encouragements during my thesis process.

My deepest thanks go to my dear wife Elif for her endless support, understanding and love. I am truly grateful to have her in my life.

Last but not least, I would like to express my sincere gratitude to my parents for their unfailing support and peerless encouragement throughout my life. I owe all of my success to them.

TABLE OF CONTENTS

ABSTRACT	v
ÖZ	vii
ACKNOWLEDGMENTS	x
TABLE OF CONTENTS	xi
LIST OF TABLES	xv
LIST OF FIGURES	xvi
LIST OF ALGORITHMS	xxi
LIST OF ABBREVIATIONS	xxii
CHAPTERS	
1 INTRODUCTION	1
1.1 Thesis Approach	2
1.2 Thesis Outcomes	3
1.3 Thesis Outline	4
2 BACKGROUND	5
2.1 OFDM	5
2.1.1 MIMO-OFDM	8
2.1.2 802.11ac	9

2.2	SDR Technology	10
2.3	GNU Radio	12
3	PHYSICAL LAYER DESIGN OF THE MIMO-OFDM TESTBED . .	15
3.1	Data Link Physical Layer Specifications	15
3.2	Frame Structure	16
3.2.1	STF	17
3.2.2	LTF	18
3.3	Transmitter	19
3.3.1	Padding	19
3.3.2	Scrambler	20
3.3.3	Channel Encoder	20
3.3.3.1	Puncturing	20
3.3.4	Interleaver and Stream Parser	21
3.3.5	Modulator	22
3.3.6	OFDM Modulator	22
3.3.6.1	Pilot Subcarriers	23
3.3.7	Preamble Generator	24
3.4	Receiver	26
3.4.1	Signal Detector	26
3.4.2	Time Synchronizer	29
3.4.2.1	Fractional Time Estimator	31
3.4.3	Frequency Synchronizer	31
3.4.3.1	Coarse Estimator	32

3.4.3.2	Fine Estimator	33
3.4.4	Channel Estimator	36
3.4.4.1	Least Squares Estimator	37
3.4.4.2	TDT Estimator	38
3.4.4.3	Maximum Channel Delay Spread Estimator	40
3.4.5	MIMO Equalizer	40
3.4.5.1	ZF	41
3.4.5.2	MMSE	41
3.4.6	Residual Phase Offset Estimator	42
3.4.7	Demodulator	43
3.4.8	Deinterleaver and Stream Deparser	45
3.4.9	Channel Decoder	46
3.4.10	Descrambler and Padding Removal	47
4	MIMO-OFDM DATA LINK SIMULATOR IMPLEMENTATION AND PERFORMANCE RESULTS	49
4.1	Data Link Simulator Design	49
4.1.1	MATLAB Configuration	49
4.1.2	RF Impairments	50
4.1.3	Channel Models	54
4.2	Data Link Simulator GUI	55
4.3	Simulation Results	58
5	TESTBED IMPLEMENTATION	65
5.1	Testbed Setup	65

5.2	USRP B210	66
5.3	3.5 GHz Antennas	67
5.4	Signal Transmission/Acquisition with GNU Radio	70
	5.4.1 Transmitter Flow-graph	70
	5.4.2 Receiver Flow-graph	71
6	TESTBED WORK	73
6.1	Data Link Tests on SDR Platform	74
6.2	2×2 MIMO Channel Analysis	76
	6.2.1 Indoor Channel Analysis	79
	6.2.2 Outdoor Channel Analysis	82
	6.2.3 Summary	89
7	SUMMARY, CONCLUSIONS AND FUTURE WORK	93
	REFERENCES	97

LIST OF TABLES

TABLES

Table 3.1	PHY Specifications of Testbed Data Link	16
Table 3.2	Code rates with corresponding puncturing patterns	21
Table 3.3	BPSK Modulated Pilot Values for SISO, 2×2 MIMO and 4×4 MIMO scenarios	24
Table 3.4	Orthogonal space-time matrices for MIMO scenario	24
Table 3.5	Cyclic Shift Values for Preamble	25
Table 5.1	Specifications of USRP B210 Board	67
Table 6.1	MIMO-OFDM Data Link Testbed Configuration	76
Table 6.2	Testbed channel analysis GUI results for the outdoor NLOS and LOS tests	87

LIST OF FIGURES

FIGURES

Figure 2.1 OFDM Block Diagram	6
Figure 2.2 Spectrum Usage: OFDM vs FDM	7
Figure 2.3 Cyclic Prefix in an OFDM symbol	7
Figure 2.4 MIMO Methods	8
Figure 2.5 MIMO-OFDM signal dimensions	9
Figure 2.6 Multi User MIMO (MU-MIMO) Scenario in 802.11ac standard . .	10
Figure 2.7 Typical SDR Block Diagram	11
Figure 2.8 SDR Examples	12
Figure 2.9 GNU Radio Application: FM Receiver	13
Figure 3.1 Testbed Data Link Frame Structure	16
Figure 3.2 STF Waveform in frequency and time domain	17
Figure 3.3 LTF Waveform in frequency and time domain	18
Figure 3.4 Data Link Transmitter Block Diagram	19
Figure 3.5 Scrambler	20
Figure 3.6 BCC Encoder Structure	21
Figure 3.7 De/Interleaving example for one OFDM symbol	22

Figure 3.8 16-QAM Modulator constellation diagram	22
Figure 3.9 CSD performance	25
Figure 3.10 Data Link Receiver Block Diagram	26
Figure 3.11 Correlator Based Signal Detector Structure	27
Figure 3.12 Simulation results for the probability of detection ($E\{w[n]^2\} = 1$) .	28
Figure 3.13 Simulation results for the probability of false alarm ($E\{w[n]^2\} = 1$)	28
Figure 3.14 Ten consecutive peaks from the output of the correlator	29
Figure 3.15 Time Synchronizer performance plot	30
Figure 3.16 Fractional time synchronizer block diagram	31
Figure 3.17 ICI problem caused by CFO	32
Figure 3.18 Performance of the coarse estimator	33
Figure 3.19 SIR vs. CFO plot	35
Figure 3.20 Performance of the fine estimators	36
Figure 3.21 Comparison between ML and ML+LS estimator	38
Figure 3.22 Performance of the channel estimators	39
Figure 3.23 Noise Enhancement Problem in ZF (a) and MMSE (b) Equalizers .	42
Figure 3.24 BER performance comparison between LLR and HD for 16-QAM symbols under AWGN	44
Figure 3.25 BER performance comparison between MIMO Detectors in 4- QAM 4×4 Communication Scenario	46
Figure 4.1 Data Link Simulator Software Functions Hierarchy	51
Figure 4.2 Data Link Simulator Process Diagram	52

Figure 4.3 Phase Noise Model block diagram	53
Figure 4.4 The spectrum of tone signal under the effect of phase noise model . .	53
Figure 4.5 Data Link Simulator GUI software snapshot	57
Figure 4.6 Data Link Simulator GUI software snapshot (Image sender is active) .	58
Figure 4.7 Simulation results for the BER performance of our data link in different modulation orders under Rayleigh channel model	59
Figure 4.8 Simulation results for the performance of MIMO spatial multiplexing scenarios under flat fading Rayleigh channel model	60
Figure 4.9 Performance of MIMO scenarios under frequency selective Rayleigh channel model	61
Figure 4.10 Performance of MIMO scenarios under flat fading Rician channel ($\kappa = 5$) model	62
Figure 4.11 Performance of different modulation types with channel coding at SISO scenario under flat fading Rician channel ($\kappa = 9$)	62
Figure 4.12 Performance of MIMO Scenarios with channel coding under flat fading Rayleigh channel	64
Figure 4.13 Performance of MIMO Scenarios under flat fading Rayleigh channel with MIMO-ML detector	64
Figure 5.1 Testbed Setup Diagram	66
Figure 5.2 The general block diagram of the USRP B210 board	67
Figure 5.3 3D Gain radiation pattern of 3.5 GHz rectangular microstrip patch antenna	68
Figure 5.4 Manufactured microstrip patch antennas (Female type SMA Connector is soldered to the feeding point and connected to the B210 with L type Male-Male SMA connector)	69

Figure 5.5 Measured S11 values of the manufactured microstrip patch antennas	69
Figure 5.6 Transmitter Flow-graph python script usage	71
Figure 5.7 Receiver Flow-graph python script usage	72
Figure 6.1 The testbed setup platform for one side	73
Figure 6.2 An example of the indoor data link testbed scenarios	74
Figure 6.3 A snapshot from the data link testbed GUI running 16-QAM 2×2 MIMO-OFDM scenario	75
Figure 6.4 Testbed configuration file	76
Figure 6.5 Indoor Channel Analysis Scenarios	80
Figure 6.6 A snapshot from the testbed channel analysis GUI running 4-QAM 2×2 MIMO-OFDM indoor NLOS scenario.	81
Figure 6.7 A snapshot from the testbed channel analysis GUI running 4-QAM 2×2 MIMO-OFDM indoor LOS scenario.	81
Figure 6.8 Indoor dynamic and static channel capacity performance in the NLOS condition	82
Figure 6.9 Outdoor test environment #1	83
Figure 6.10 Dynamic and static channel capacity performance in the outdoor environment #1 (Average SNR is measured as 24 dB in static cases.)	84
Figure 6.11 Outdoor test environment #2	85
Figure 6.12 Dynamic and static channel capacity performance in the outdoor environment #2	85
Figure 6.13 Outdoor test environment # 2: MIMO channel analysis tests for LOS and NLOS conditions	86

Figure 6.14 A snapshot from the testbed channel analysis GUI running 4-QAM 2×2 MIMO-OFDM outdoor NLOS scenario	87
Figure 6.15 A snapshot from the testbed channel analysis GUI running 4-QAM 2×2 MIMO-OFDM outdoor LOS scenario	88
Figure 6.16 MIMO channel performance in the mobile measurement scenario .	89
Figure 6.17 Outdoor environment # 2: Mobile measurement scenario walking trajectory plan	90

LIST OF ALGORITHMS

ALGORITHMS

- Algorithm 1 Pseudo code for time synchronization algorithm. 30

LIST OF ABBREVIATIONS

API	Application Programming Interface
AWGN	Additive White Gaussian Noise
BCC	Binary Convolutional Codes
BER	Bit Error Rate
BPSK	Binary Phase Shift Keying
CIR	Channel Impulse Response
CFO	Carrier Frequency Offset
CP	Cyclic Prefix
DVB-T	Digital Video Broadcasting-Terrestrial
DFT	Discrete Fourier Transform
DSP	Digital Signal Processing
EVM	Error Vector Magnitude
FBMC	Filter Bank Multi-carrier
FDM	Frequency Division Multiplexing
FFT	Fast Fourier Transform
f-OFDM	Filtered Orthogonal Frequency Division Multiplexing
FPGA	Field Programmable Gate Array
GUI	Graphical User Interface
ICI	Inter Carrier Interference
IDFT	Inverse Discrete Fourier Transform
IFFT	Inverse Fast Fourier Transform
IID	Independent and Identically Distributed
ISI	Inter Symbol Interference
LLR	Log-likelihood Ratio
LOS	Line of Sight
LS	Least Squares
LTF	Long Training Field
MIMO	Multiple Input Multiple Output
ML	Maximum Likelihood
MMSE	Minimum Mean Square Error
M-QAM	M-ary Quadrature Amplitude Modulation
MU-MIMO	Multi User Multiple Input Multiple Output

NLOS	None Line of Sight
OFDM	Orthogonal Frequency Division Multiplexing
PAPR	Peak to Average Power Ratio
PHY	Physical Layer
QoS	Quality of Service
RMSE	Root Mean Square Error
SDR	Software Defined Radio
SIR	Signal to Interference Ratio
SISO	Single Input Single Output
SMA	Sub Miniature version A
SNR	Signal to Noise Ratio
SSH	Secure Shell
STF	Short Training Field
SVD	Singular Value Decomposition
TDT	Time Domain Truncation
UHD	USRP Software Driver
USRP	Universal Software Radio Peripheral
VNA	Vector Network Analyzer
WLAN	Wireless Local Area Network
ZF	Zero Forcing
5G	Fifth Generation

CHAPTER 1

INTRODUCTION

Over the last decades, wireless communications has become the rapid growing technology in the telecommunications field. It is used in many applications including the fields of consumer electronics, military, aerospace etc. At the beginning of 1990's, with the advent of Internet [1] and digital communication [2] technologies, it started to be an indispensable part of our daily lives. Today, majority of the people use wireless technology everyday with many services including cellular systems (2G/3G/4G), WLANs (802.11a/b/g/n/ac), digital-TV (DVB-T) etc. With the advancing technology on these services, customers demand for better QoS (Quality of Service) and higher data rates (with higher spectral efficiencies) which require new techniques and standards for wireless communication systems. One mature technique to achieve these requirements is Orthogonal Frequency Division Multiplexing (OFDM) [3]. It is basically a multi-carrier communication technique where modulation is performed in orthogonal sub-carriers in the available spectrum. Another technology increasing the spectral efficiency and diversity is multiple input multiple output (MIMO) systems. It is the use of multiple antennas at both sides of the wireless link. With MIMO, linear increase in data rate can be achieved by spatial multiplexing and diversity can be increased by space-time coding [4]. The good news is that OFDM works well with MIMO technology [5]. Hence MIMO-OFDM is commonly used in current communication systems such as LTE [6] (4G cellular standard), 802.11ac [7] (WLAN standard) and also a candidate waveform for the next generation wireless standards, e.g., 5G [8].

In both academia and industry, researchers and engineers are studying new algorithms

for wireless communication systems in the simulation environment. But as to validate the algorithms on hardware, a myriad of problems are encountered including issues related to cost, time, and effort. Today, Software Defined Radio (SDR) brings a new concept to communication technology that people can modify and operate wireless systems completely just by software instead of hardware [9]. Thus, new algorithms and concepts can be implemented on hardware in a flexible way through SDR.

In order to test and validate algorithms for research purposes in field trials, testbed platforms are used. In the literature, OFDM testbed studies have been carried out commonly. While some of them are based on testbed studies for MIMO-OFDM systems [10] [11] [12], some are only for SISO-OFDM systems [13] [14] [15]. Also, in some studies the testbed platform is implemented by using SDR devices due to its flexible design environment. These approaches motivate us to implement a MIMO-OFDM data link testbed platform on an SDR hardware.

In this thesis, first we design a data link simulator to implement, test, and verify algorithms for MIMO-OFDM systems. Then a testbed platform is implemented by using USRP B210 [16] (an SDR device) to validate our algorithms and data link performance at 3.5 GHz which is the foremost candidate frequency band in 5G standard [17]. Additionally, by using our testbed platform, we measure the 2×2 MIMO channel characteristics at indoor and outdoor environments in the case of static and dynamic scenarios.

1.1 Thesis Approach

The items listed below are our strategies to reach the goals of this thesis study:

- Specify the requirements for the physical layer design
- Design the frame structure of a MIMO-OFDM data link
- Implement and test the algorithms for all signal processing blocks in the MIMO-OFDM communication link
- Implement various algorithms for frequency synchronization, channel estimation, equalization and detection blocks, and compare their performance

- Implement a simulator for our MIMO-OFDM data link, add different channel models and hardware impairments for verifying the MIMO-OFDM data link structure on a more realistic platform
- Run MIMO-OFDM simulation including hardware impairments in different channels and configurations
- Implement a testbed platform by using an SDR hardware
- Test MIMO-OFDM data link in testbed and verify algorithms in real environment
- Perform a channel characteristic analysis by using our testbed and obtain results for the performance of a 2×2 MIMO channel in different environments at 3.5 GHz

1.2 Thesis Outcomes

With this study, following two main items are achieved:

- We designed a MIMO-OFDM data link simulator in MATLAB. This tool can be used to test and verify the performance of MIMO-OFDM waveform in different configurations. We can upgrade it by adding new models for hardware impairments, channels or new algorithms such as synchronization, channel estimation.
- We implemented a MIMO-OFDM testbed platform by using an SDR (USRP B210) hardware. It provides you an easy deployment of MIMO-OFDM data link and channel analysis testbed structure for sub 6 GHz applications. Any algorithms implemented on simulation environment can be directly tested and verified with our testbed.

1.3 Thesis Outline

The rest of this thesis study is organized as follows:

- Chapter 2 covers the background information on MIMO, OFDM and SDR technologies with their historical progress and applications.
- In Chapter 3, we present the physical layer (PHY) design of the MIMO-OFDM testbed data link including all signal processing blocks for both transmitter and receiver.
- In Chapter 4, the design of our data link simulator and its simulation results are presented.
- Chapter 5 gives our testbed implementation on an SDR platform.
- Chapter 6 data link tests and 2×2 MIMO channel analysis at 3.5 GHz are presented in detail.
- Final Chapter 7 includes conclusion remarks and future tasks.

CHAPTER 2

BACKGROUND

2.1 OFDM

Orthogonal Frequency Division Multiplexing (OFDM) is a digital multi-carrier modulation technique in which the spectrum is divided into adjacent orthogonal (narrowband) channels (subcarriers), and single carrier communication is performed on each subcarrier independently [18]. Thus, subcarriers can be modulated with different types of modulation schemes. Although multi-carrier modulation was found in the 1960's, the system was too complex and costly to design and implement for communication purposes due to the need for modulator and demodulator of each subcarrier separately. Around 1990's, thanks to the advances in semiconductor technology, engineers produced electronic chips that effectively perform discrete Fourier and inverse discrete Fourier transformations (DFT/IDFT). As a result, this technique started to be used in the communication industry. Nowadays, with the huge improvements in integrated circuit design, OFDM became one of the most popular communication techniques preferred in many communications standards.

In OFDM, data bits are mapped to each subcarrier and IDFT is applied to the modulated symbols so as to produce orthogonal multi-carrier signals in time domain. On the receiver side, inverse procedures are applied to the received signal for demodulation (Figure 2.1). Thus, DFT is performed to extract each modulated subcarrier signal. Instead of DFT and IDFT operations, FFT (Fast Fourier Transform) and IFFT (Inverse Fast Fourier Transform) are preferred to be used in the applications due to computational complexity advantages [19].

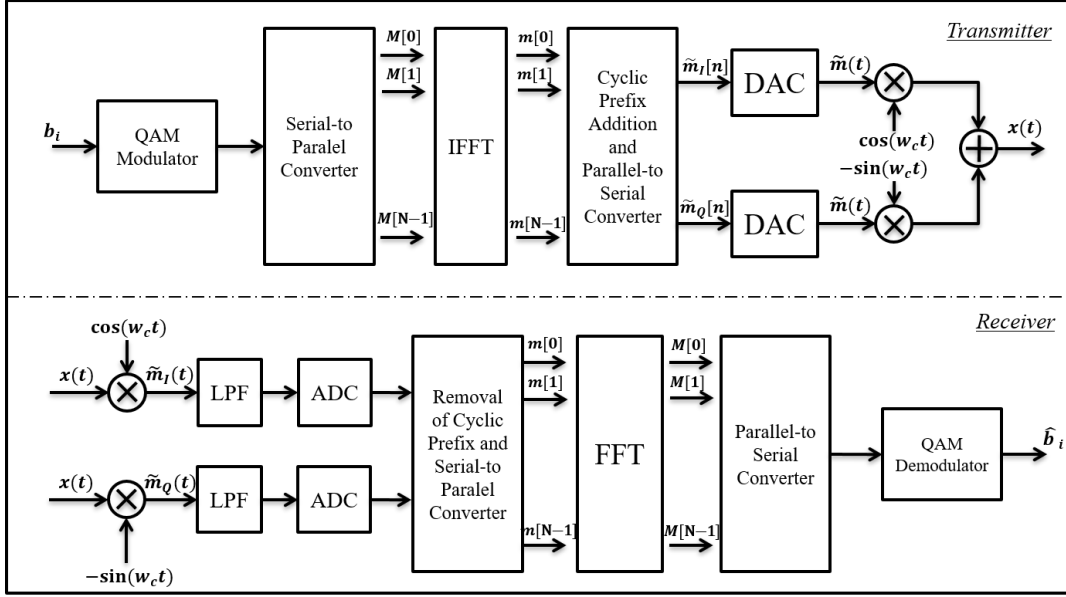


Figure 2.1: OFDM Block Diagram

In single-carrier communication systems, symbols are transmitted in series through a single carrier. Such communication systems are less sensitive to frequency shifts, phase noise and peak-to-average power ratio (PAPR) compared to multi-carrier communication systems like OFDM. Even so, the effects of these factors can be compensated by using various methods.

In another multi-carrier communications system called Frequency Division Multiplexing (FDM), subcarriers are separated from each other with guard band intervals in order to prevent inter carrier interference (ICI). But, a large majority of the spectrum is wasted in that case (Figure 2.2). On the other hand, in OFDM, successive subcarriers orthogonally overlap with each other; hence, it both prevents ICI problem and uses the spectrum more efficiently. Additionally, filters for each subcarrier are needed in FDM systems, but there is no need for them in OFDM which simplifies the transmitter structure. Besides all these advantages, OFDM signals are more sensitive to frequency shifts. Therefore, a minor shift in frequency results in non-orthogonal subcarriers and creates ICI problem. More robust frequency synchronizers are used in OFDM systems for this reason. For example, one may have to be careful in using OFDM for high-speed vehicle communication systems due to frequency shifts caused by the Doppler effect [20].

As modulated data is sent in parallel in frequency domain over one OFDM symbol

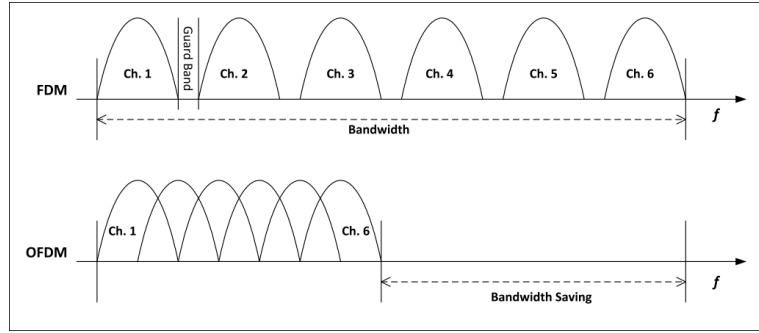


Figure 2.2: Spectrum Usage: OFDM vs FDM [21]

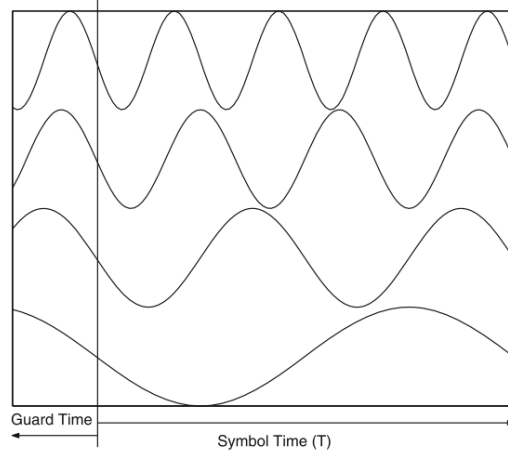


Figure 2.3: Cyclic Prefix in an OFDM symbol (Thanks to the CP, it saves the circularity of channel response in time domain so that subcarriers stay orthogonal in frequency.)

period, the symbol rate is reduced so that the interference caused between successive symbols (ISI) is decreased too. Also, in order to prevent ISI effect, a special type of guard interval called cyclic prefix (CP) is used at each OFDM symbol (Figure 2.3). This prefix turns the linear convolution model between the channel and signal into circular, hence it recovers the orthogonality of each subcarrier in frequency domain. In this way, channel estimation and equalization problems can be solved easily on the receiver side.

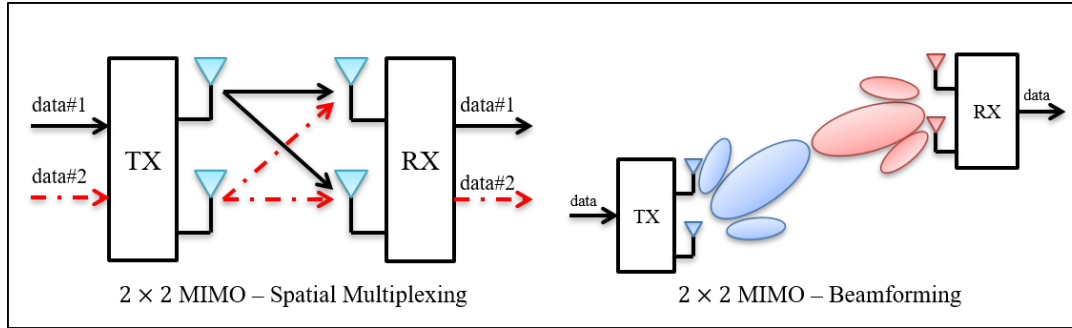


Figure 2.4: MIMO Methods

2.1.1 MIMO-OFDM

MIMO or Multiple Input Multiple Output can be referred to the use of multiple antennas at the receiver and transmitter. This concept is used to increase the data rate with spatial multiplexing or to achieve diversity with beamforming and diversity coding methods (Figure 2.4). In spatial multiplexing, the signal is split into multiple streams and they are transmitted concurrently. On the receiver side, multiple streams are processed with the use of estimated channel knowledge. In this way, capacity is increased approximately linearly with the number of antennas used in MIMO communication [22]. Beamforming and diversity coding methods are performed by using a single stream. In diversity coding, various precoding techniques are applied to the signal in space or space-time and then it is transmitted from multiple antennas [23]. Hence, this exploits the independent fading of MIMO channels by increasing the diversity of the link. In beamforming, a single stream is multiplied with a steering vector creating the beam at the desired direction and transmitted from antennas. The same procedure is applied in receiver, and streams are added up constructively after multiplying with a steering vector so that the link achieves diversity gain in both transmitter and receiver. With these advantages, the MIMO technique has become popular in the last decades and it has been widely used in different platforms.

Although, MIMO can be used in any type of modulation, OFDM works with MIMO very well because of the fact that it represents the signal with frequency-time blocks and each subcarrier falls into near-flat fading instead of frequency selective. Beside these, MIMO brings this platform a third dimension, space, so that the signal can be represented in space-time-frequency blocks (Figure 2.5). Communication will be

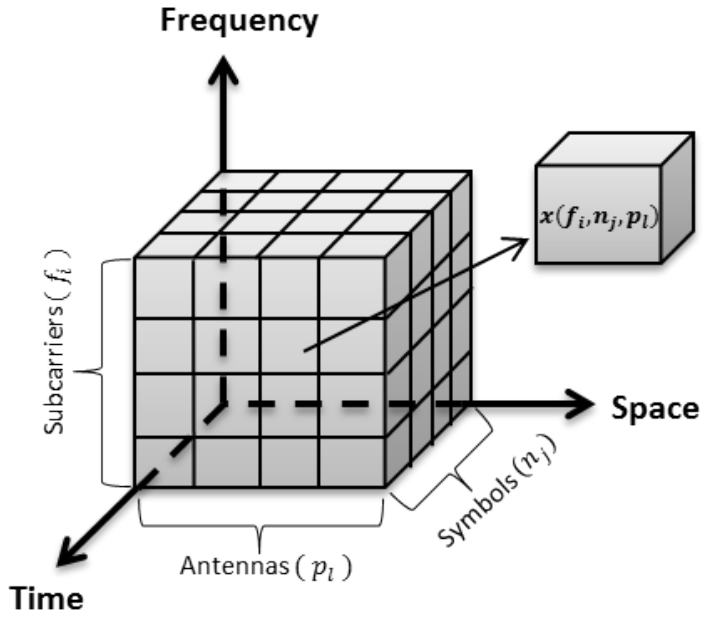


Figure 2.5: MIMO-OFDM signal dimensions

performed in this three dimensional grids independently for each-subcarrier at each OFDM symbol period. In such a way, MIMO-OFDM systems are easily modeled for use in modern communication standards such as 802.11ac [7], LTE [24], etc.

2.1.2 802.11ac

802.11ac is a member of 802.11 family standard, including MIMO-OFDM structure in its physical layer. Its development started in 2008 and the first version was published in 2013. The main target with this standard was to provide high rate throughput at sub-6 GHz frequency band. In this manner, the core technologies coming with 802.11ac are

- MIMO-OFDM (up to 8 streams),
- Higher bandwidths (up to 160 MHz),
- Spatial multiplexing and beamforming techniques,
- High order modulations (e.g., 256 QAM),
- Multi User MIMO (only for downlink) (Figure 2.6).

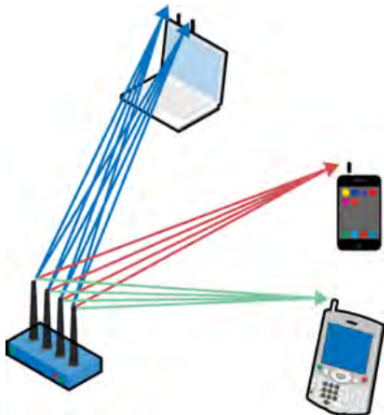


Figure 2.6: Multi User MIMO (MU-MIMO) Scenario in 802.11ac standard [25]

With the above features, this standard provides gigabit (up to 6933 Mbit/s [25]) data rates to its users with high spectral efficiencies. In this study, 802.11ac was taken as a reference for some physical layer structures of the testbed data link.

2.2 SDR Technology

Software defined radio (SDR) is a communication concept which states the radio can be almost totally controlled and run by software instead of hardware. So a typical SDR device, as shown in Figure 2.7, may include amplifiers, mixers, filters, A/D and D/A converters followed by FPGAs or DSPs for controlling and building a digital data bridge between software and hardware on the system. The rest of the work covering all signal processing algorithms related with physical layer are performed in software. The term *Software Radio* is firstly introduced by a research team working at E-Systems Inc. in 1984. They developed a digital baseband receiver in the laboratory as a proof-concept for an application of *Software Radio* [26]. Although this concept is not new, technological improvements of digital electronics open the way of using SDRs in real life rather than in research environments. General use cases of SDRs are:

- **Research and Development:** SDRs can easily be used to test various waveforms, communication protocols and different algorithms in software. For such purposes they are mostly preferred in universities and R&D labs of companies.

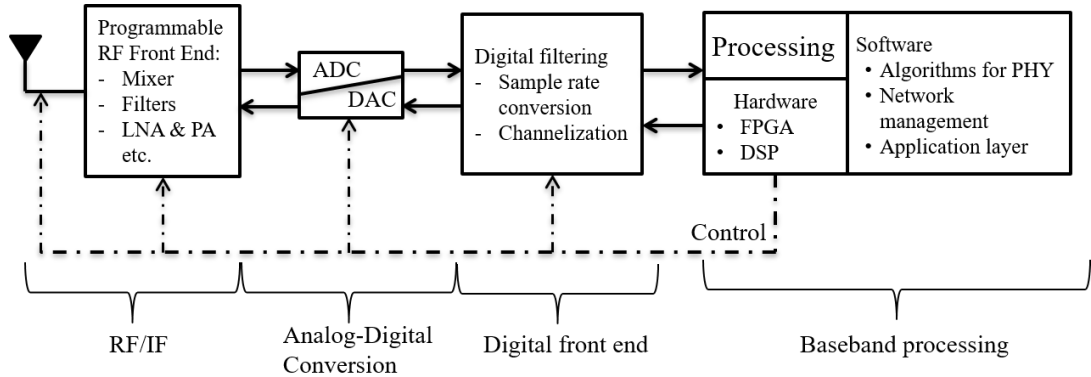


Figure 2.7: Typical SDR Block Diagram

- **Military Communications:** A radio that can change all its features easily is a vital advantage for military communication systems for providing a secure environment against enemy attacks. SDR based radio is able to change its modulation type, bandwidth, operating frequency, encryption etc. just by programming its software.
- **Civilian Communications:** The cost of building new base stations may be large in the civilian communications world. Since new standards are coming out continuously, network providers have to rebuild the base stations with the new standard communication requirements. However, if the existing base station infrastructure is a type of SDR, the cost can be minimized because of changing only software instead of hardware.
- **Test & Analysis:** SDRs can be used for numerous type of test applications because of fast signal generation and analysis capabilities. Additionally, they are used for spectrum monitoring, signal simulator applications due to the same reasons.

Because of the use cases mentioned above, SDRs are becoming very popular nowadays. Big companies such as Analog Devices and Lime Microsystems design SDR transceiver chips to encourage companies to produce SDR type modems, test equipments and other signal processing applications. Some companies, such as Ettus Research and Epiq Solutions, have powerful products using SDR transceiver chips (Figure 2.8).

Other than these, some SDRs are also produced for people who are interested in

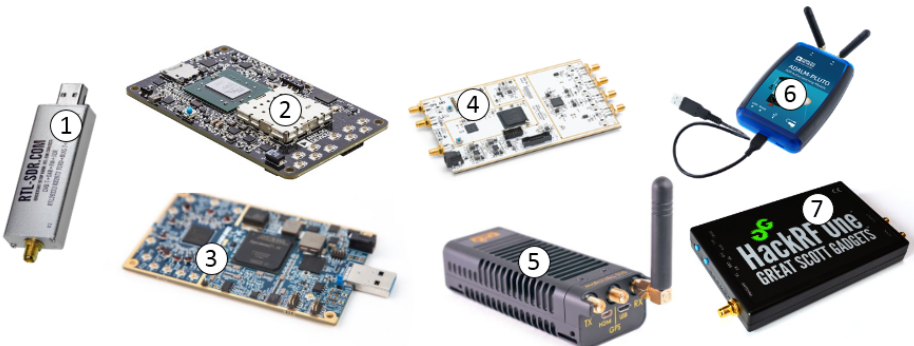


Figure 2.8: SDR Examples: RTL-SDR (#1), ADRV9361 by Analog Devices AD9361 SDR Module (#2), LimeSDR by Lime Microsystems SDR including LMS7002M (#3), USRPB210 by Ettus Research SDR including AD9361 (#4), Matchstiq by Epiq Solutions including AD9364 (#5), ADALM-PLUTO SDR (#6), HackRF One (#7)

amateur radio applications or use for educational purposes. As shown in Figure 2.8, some examples are RTL-SDR using Realtek RTL2832U controller/tuner, HackRF One from Great Scott Gadgets and ADALM-PLUTO SDR from Analog Devices.

2.3 GNU Radio

Since there are a lot of SDRs on the market, some software packages should be provided to control and use such products. Other than specific software libraries offered from SDR companies itself, there are some platforms supporting a bunch of SDR devices, providing a development environment to its users. Some examples are MATLAB [27], LabVIEW [28] and GNU Radio [29]. Unlike MATLAB and LabView which are commercial, GNU Radio is an open-source platform providing signal processing blocks for implementing SDR based applications. Most of SDR products are supported by GNU Radio and it is growing rapidly due to its open-source structure.

In GNU Radio:

- You can build your own radio protocol by using blocks/functions of GNU Radio,
- You can create your own signal processing blocks to test your specific algorithm,

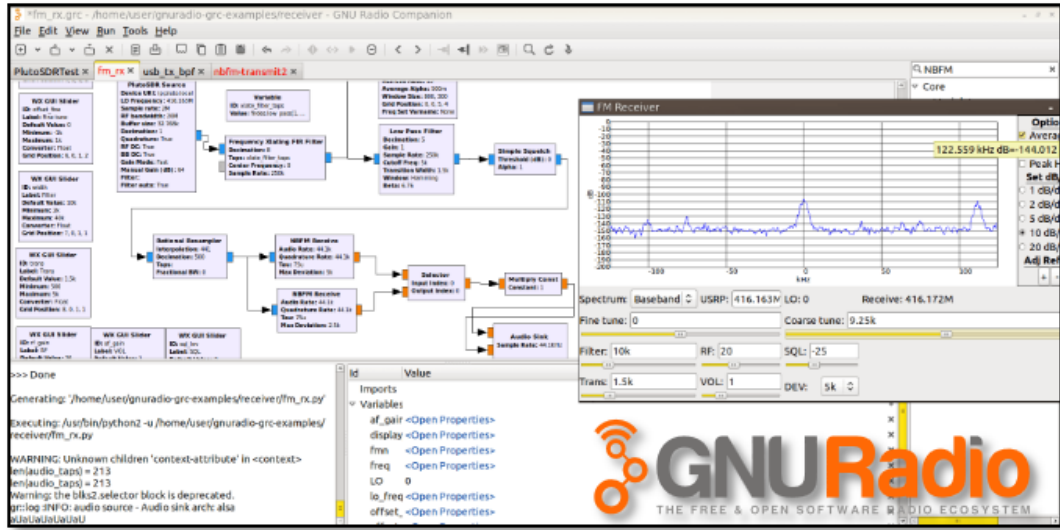


Figure 2.9: GNU Radio Application: FM Receiver [30]

- You can easily create your real-time test setup with SDRs,
- You can perform all other tasks related with generation of various signal waveforms or processing of RF signals (e.g. Figure 2.9).

In this study, we used GNU Radio software in conjunction with USRP B210 SDR devices for data acquisition and transmission purposes of the MIMO-OFDM testbed application.

CHAPTER 3

PHYSICAL LAYER DESIGN OF THE MIMO-OFDM TESTBED

In this chapter, we will present the physical layer (PHY) design of the testbed data link. Initially, we will give the PHY specifications. In the second section, the frame structure will be presented. Following sections will give detailed explanations for transmitter and receiver structures respectively.

3.1 Data Link Physical Layer Specifications

In this study, our aim is to establish a generic testbed data link hardware/software system using MIMO-OFDM technique which performs high speed communication and provides MIMO channel analysis applications. Hence, we determine the specifications of testbed PHY by considering our requirements. While determining the specifications of testbed PHY, 802.11ac standard has been taken as reference.

Physical layer specifications used in our testbed are shown in Table 3.1. As it is seen, SISO and MIMO spatial multiplexing scenarios are provided in this PHY. The spectrum is divided into 64 subcarriers. While 52 out of 64 are filled by data; 4 of them are used for pilots and the rest, DC and higher/lower edge subcarriers, are left blank to avoid DC related problems in OFDM waveform [31] and to prevent interference from adjacent channels. Data subcarriers are modulated with M-ary QAM with $M = 4/16/64/256$ options. Additionally, preamble duration depends on the number of spatial streams (N_{SS}) used for MIMO scenario.

Table 3.1: PHY Specifications of Testbed Data Link

Parameter	Value
Technique	SISO & MIMO (up to 8 streams) with Spatial Multiplexing
Modulation	OFDM
Subcarrier Modulation	M-QAM (M=4/16/64/256)
FFT Length (Subcarriers)	64
Data Subcarriers	52
Number of Pilots	4
Total Number of Subcarriers	56
Non-zero Subcarrier Index	$\pm (1, 2, \dots, 28)$
OFDM Symbol Duration	3.2usec ¹
Guard Interval	0.8usec
OFDM Symbol Period	4usec ¹ (3.2+0.8)
Preamble Duration	$\geq 12\text{usec}^1 (8+4xN_{SS})$
Signal Bandwidth	5/10/20 MHz
Packet Length	$\leq 1\text{ms}$

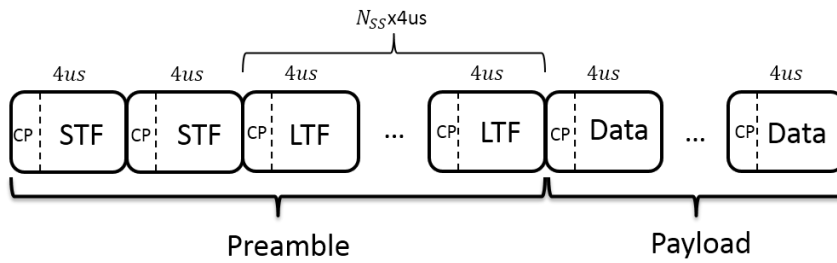


Figure 3.1: Testbed Data Link Frame Structure

3.2 Frame Structure

The frame structure of our testbed PHY shown in Figure 3.1 is actually a simplified version of 802.11ac's frame structure with some tiny differences. It is composed of preamble and payload. In the preamble part, there are short training field (STF) and long training field (LTF) symbols². In the payload part, only data symbols exist. Additionally, each symbol has a cyclic prefix (CP) part at the beginning of the OFDM symbol.

¹ Parameter values are calculated by assuming OFDM bandwidth as 20 MHz. Although this PHY supports lower bandwidth options, 20MHz bandwidth option will be taken as reference in the rest of this thesis.

² These terms are used in 802.11ac standard. They have specific type of waveforms to be used as preamble in OFDM based applications so that we preferred to use them in our frame structure.

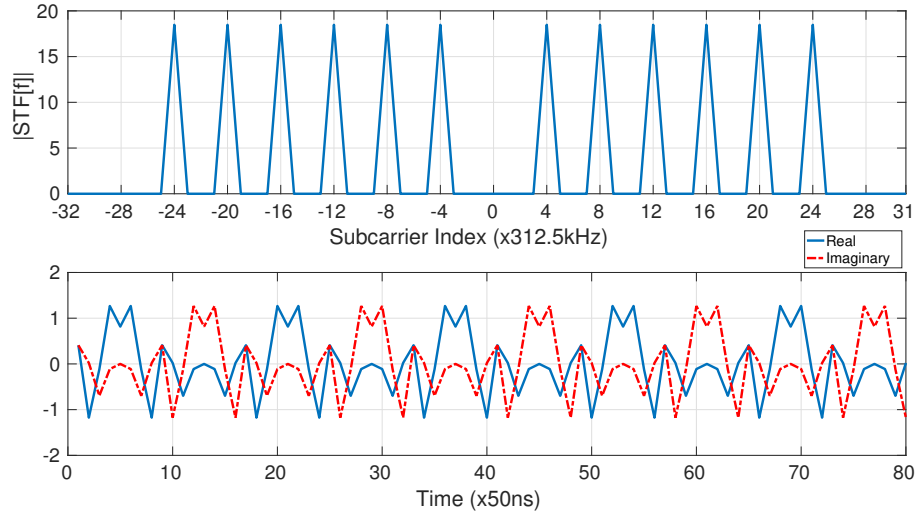


Figure 3.2: STF Waveform in frequency and time domain

3.2.1 STF

Two STF symbols are used in preamble for time synchronization and frequency offset correction operations. The STF symbol can be defined in frequency domain as

$$STF_{-28,28} = \sqrt{\frac{1}{2}} \{ 0, 0, 0, 0, 1 + j, 0, 0, 0, -1 - j, 0, 0, 0, 1 + j, 0, 0, 0, -1 - j, 0, 0, \\ 0, -1 - j, 0, 0, 0, 1 + j, 0, 0, 0, 0, 0, 0, -1 - j, 0, 0, 0, -1 - j, \\ 0, 0, 0, 1 + j, 0, 0, 0, 1 + j, 0, 0, 0, 1 + j, 0, 0, 0, 1 + j, 0, 0, 0, 0 \}. \quad (3.1)$$

The subscript shows the subcarrier index values for OFDM symbol. The corresponding STF waveform in time and frequency is shown in Figure 3.2. As it is seen, out of 64 subcarriers only 12 of them are used and the waveform becomes periodic (5 repetitive sequences in one STF symbol) in time domain. This characteristic will be useful for signal detection and frequency synchronization operations.

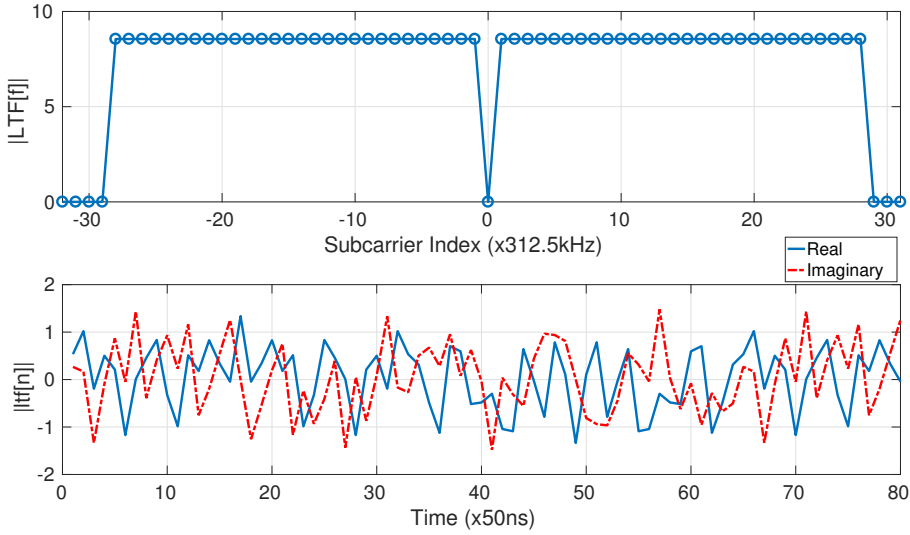


Figure 3.3: LTF Waveform in frequency and time domain

3.2.2 LTF

Channel estimation will be performed by using LTF symbols. The number of spatial streams (antennas) used in data link scenario will determine the number of LTF symbols in the preamble part. For example, in MIMO scenario with 2 antennas on transmitter and receiver (2×2), two LTF symbols are used. It can be represented in frequency domain as

$$\begin{aligned}
 LTF^- &= \{1, 1, -1, -1, 1, 1, -1, 1, -1, 1, 1, 1, 1, 1, -1, -1, 1, 1, 1, -1, 1, 1, 1, 1, 1\} \\
 LTF^+ &= \{1, -1, -1, 1, 1, -1, 1, -1, 1, -1, -1, -1, -1, -1, 1, 1, -1, \\
 &\quad -1, 1, -1, 1, -1, 1, 1, 1, 1, 1\} \\
 LTF_{-28,28} &= \{1, 1, LTF^-, 0, LTF^+, -1, -1\}.
 \end{aligned} \tag{3.2}$$

All subcarriers except the ones that are not used for data and pilot are filled in LTF part. In Figure 3.3, the LTF waveform is shown in frequency and time domain.

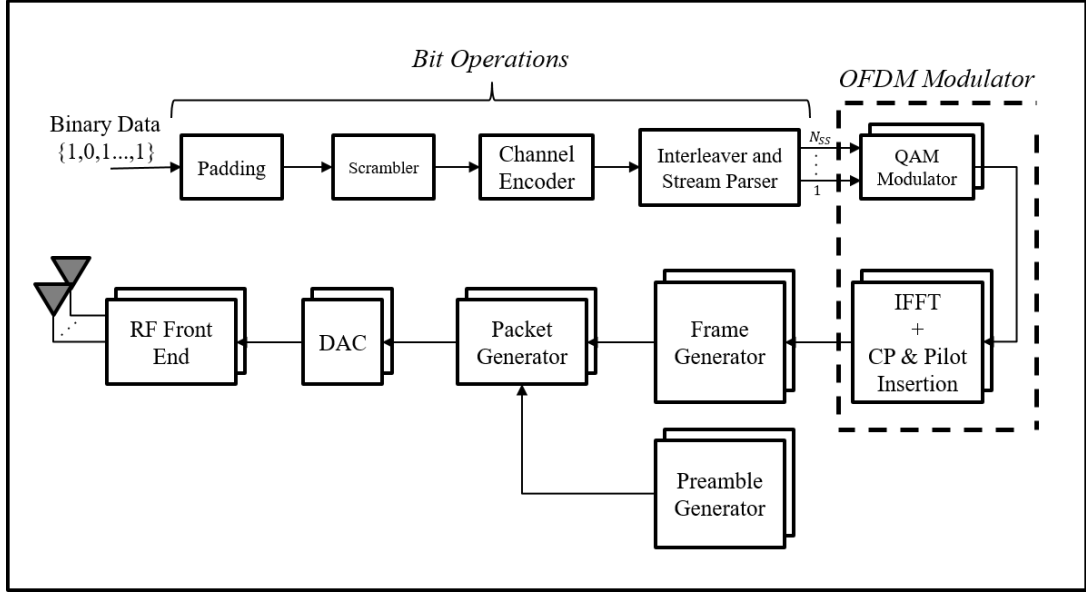


Figure 3.4: Data Link Transmitter Block Diagram

3.3 Transmitter

Figure 3.4 highlights the block diagram of the transmitter. As can be seen, after a series of binary operations, message bits are modulated and OFDM waveform is obtained. Also, it is to be observed that blocks are multiplexed for the MIMO scenario.

3.3.1 Padding

The first operation performed on the transmitter PHY is padding. Here, redundant zero bits are added to the bits coming from application layer in order to match the number of data bits carried in one packet. Thus, the number of OFDM symbols in payload can be selected as an integer number. Padding bits are calculated as

$$N_{PAD} = N_{SYM}N_{DBPS} - N_{APPDB} \quad (3.3)$$

$$N_{DBPS} = N_{DSC} \log_2(M) \quad (3.4)$$

where N_{PAD} is the number of padding bits, N_{SYM} is the number of OFDM symbols in payload, N_{DBPS} is the number of data bits per one OFDM symbol and N_{APPDB} is the number of application layer bits. Also, N_{DBPS} is found by multiplying the number of data subcarriers in one OFDM symbol (N_{DSC}) with the number of bits ($\log_2(M)$) used in one subcarrier. M denotes the modulation order.

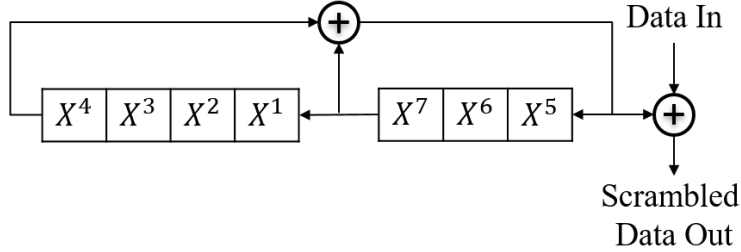


Figure 3.5: Scrambler

3.3.2 Scrambler

There may be long series containing only 1 or 0 in the data received from the application layer. In such cases, undesired spectral components of performance losses are observed during decoding operation on the receiver side. For this purpose, the long bit pattern carrying the same value will be changed by scrambling the data. The polynomial used in the scrambler is shown in (3.5) and depicted in Figure 3.5. On the receiver side, the actual bit pattern can be recovered using descrambler which has actually the same structure with the scrambler.

$$S(z) = 1 + z^{-4} + z^{-7} \quad (3.5)$$

3.3.3 Channel Encoder

The purpose of channel encoding is to increase the reliability of the message bits by inserting redundant bit patterns. In our testbed, binary convolutional codes (BCC) are preferred. The block diagram of BCC encoder is shown in Figure 3.6. As seen, constraint length (K) is 7 and generator polynomials are [133 171] with 1/2 coding rate.

3.3.3.1 Puncturing

In order to provide different code rate values, puncturing is used. With this method, some part of the 1/2 rate encoded bits are removed and the encoder can work with higher coding rates. This removal operation is performed by using a pre-determined

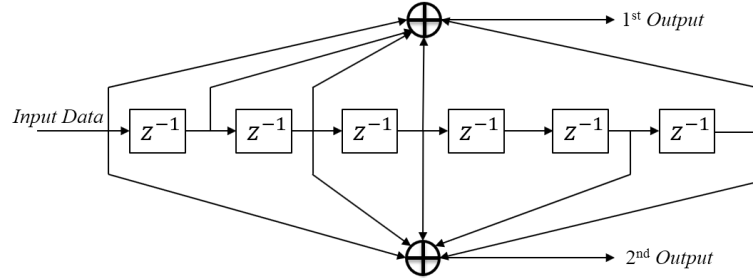


Figure 3.6: BCC Encoder Structure

Table 3.2: Code rates with corresponding puncturing patterns

<i>Code Rate</i>	<i>Puncturing Pattern</i>
$2/3$	[1, 1, 0, 1]
$3/4$	[1, 1, 0, 1, 1, 0]
$5/6$	[1, 1, 0, 1, 0, 1, 0, 1, 0, 1]

puncturing pattern so that the receiver knows which bits are erased. Table 3.2 shows achieved code rates with the corresponding puncturing patterns [32].

3.3.4 Interleaver and Stream Parser

Channel encoders are traditionally designed to operate in uncorrelated AWGN (Additive White Gaussian Noise) channels. However, in reality, noise or channel gains are correlated in time and frequency so that the channel introduces burst type errors with memory instead of independent random errors. One way to cope with these type of channels is to spread out the burst errors so as to make them pseudo-random. This operation is called interleaving. It is performed by shuffling data bits at transmitter and recovering them on receiver with reverse operation of shuffling (Figure 3.7). In our testbed, block type interleavers, taken from the 802.11 standard for OFDM type applications [7], are preferred.

After interleaving series of bits, they re-arranged into parallel streams with stream parsing. It simply distributes series of bits in order into the number of spatial streams (N_{SS}) parallel blocks to be used in MIMO scenario. With stream parsing, diversity gain is achieved in transmitter side when it is used with channel coding together.

Transmitted Bits	11000010000001001100001011000001001011010011100110010110001010101110100110111110010001110010010111011
Received Bits	1011001000111011000011110000011001101100000111100eeeeeeeeee11101001011010101010001011001000111101001
De-Interleaving	1100e0100000e1001100e0101100e0010010e1010011e0011001e1110001e10101110100110111110e1000111e0100101e1011

Figure 3.7: De/Interleaving example for one OFDM symbol

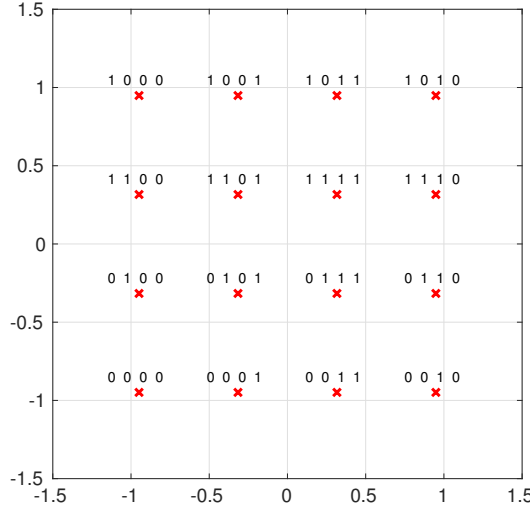


Figure 3.8: 16-QAM Modulator constellation diagram

3.3.5 Modulator

Encoded and interleaved data bits are mapped to QAM constellation points in a modulator. In the testbed PHY, 4/16/64/256 QAM types are used with Gray coding. An example of 16-QAM constellation diagram is shown in Figure 3.8. For MIMO operation, each spatial stream is modulated separately.

3.3.6 OFDM Modulator

After the modulator maps data bits to M-QAM symbols, the OFDM waveform is generated here. The discrete time model of OFDM symbol in frequency domain is shown as

$$X[k] = \begin{cases} D[k], & k = i_{DSC} \\ P[k], & k = i_{PSC} \end{cases} \quad (3.6)$$

where i_{DSC} and i_{PSC} shows the subcarrier index values for data and pilot subcarriers respectively, $D[k]$ is the M-QAM symbols for data and $P[k]$ is the BPSK modulated symbols for pilot. The rest of them, DC and guard subcarriers, are nulled. Then, IFFT algorithm converts the frequency components through OFDM symbol into time samples $x[n]$.

$$x[n] = \frac{1}{\sqrt{N}} \sum_k X[k] e^{j2\pi nk/N} \quad (3.7)$$

As seen in (3.7), signal contains the sum of $D[k]$ and $P[k]$ symbols each modulated by carrier frequency $e^{j2\pi nk/N}$. The total number of subcarriers is N which is 64 for our application. Lastly, a cyclic prefix is added to the sequence $x[n]$ so that

$$x[l - L] = x[l + N - L], \quad l = 0, 1, \dots, L - 1 \quad (3.8)$$

where L is the cyclic prefix length which accounts for %25 of the OFDM symbol. Therefore, resulting time samples have length of $N + L$. In MIMO scenario, OFDM symbols are generated for each spatial stream separately in the same way except pilot sequences.

3.3.6.1 Pilot Subcarriers

On each OFDM symbol, some subcarriers are used as pilots for frequency synchronization, residual phase offset correction, and channel estimation operations. In our testbed, BPSK modulated sequence is used with $i_{PSC} = \{\pm 7, \pm 21\}$ frequency index values for pilots. If the same pilot sequence is used for all OFDM symbols, there will be spectral lines in the generated OFDM waveform. To prevent this, pilot sequence is cyclically rotated over symbols. For MIMO scenario, different patterns are used for each spatial stream to prevent unintentional beamforming. (3.9) shows the generation of pilot sequences for each symbol on each spatial stream:

$$\mathbf{p}_{(i_{SS}, m)}^{i_{PSC}} = \{\Omega_{(i_{SS}, m \oplus 4)}, \Omega_{(i_{SS}, (m+1) \oplus 4)}, \Omega_{(i_{SS}, (m+2) \oplus 4)}, \Omega_{(i_{SS}, (m+3) \oplus 4)}\}. \quad (3.9)$$

Here, i_{SS} shows the index of spatial stream, m is the index for OFDM symbol and Ω is the BPSK modulated pilot value. In Table 3.3, corresponding Ω values are given.

Table3.3: BPSK Modulated Pilot Values for SISO, 2×2 MIMO and 4×4 MIMO scenarios

N_{SS}	i_{SS}	$\Omega_{(i_{SS},0)}$	$\Omega_{(i_{SS},1)}$	$\Omega_{(i_{SS},2)}$	$\Omega_{(i_{SS},3)}$
1	1	1	1	1	-1
2	1	1	1	-1	-1
2	2	1	-1	-1	1
4	1	1	1	1	-1
4	2	1	1	-1	1
4	3	1	-1	1	1
4	4	-1	1	1	1

Table3.4: Orthogonal space-time matrices for MIMO scenario

N_{SS}	2	4	8
Space-time Matrix $\mathbf{P}_{LTF}^{N_{SS}}$	$\begin{bmatrix} 1 & -1 \\ 1 & 1 \end{bmatrix}$	$\begin{bmatrix} 1 & -1 & 1 & 1 \\ 1 & 1 & -1 & 1 \\ 1 & 1 & 1 & -1 \\ -1 & 1 & 1 & 1 \end{bmatrix}$	$\begin{bmatrix} \mathbf{P}_{LTF}^4 & -\mathbf{P}_{LTF}^4 \\ \mathbf{P}_{LTF}^4 & \mathbf{P}_{LTF}^4 \end{bmatrix}$

3.3.7 Preamble Generator

Preamble is used for signal detection, synchronization, and channel estimation operations. As shown in Figure 3.1, it includes two STF and N_{SS} LTF symbols. In case of the MIMO scenario, the LTF part is multiplied with a space-time orthogonal matrix so that the receiver can estimate the each channel coefficients. In Table 3.4, orthogonal matrices used for different MIMO scenarios are given where columns represent spatial streams and rows represent the time. Thus, generated LTF waveforms can be computed as

$$\mathbf{s}_{LTF} = LTF \times \mathbf{P}_{LTF}^{N_{SS}} . \quad (3.10)$$

Multiplication is performed over symbols. For example, \mathbf{s}_{LTF} for $N_{SS} = 2$ is

$$\mathbf{s}_{LTF} = \begin{bmatrix} LTF & -LTF \\ LTF & LTF \end{bmatrix} . \quad (3.11)$$

If the same preamble is used for each spatial stream in a MIMO scenario, the received signal can suffer from unintended beamforming that is the preamble part may diminish. To prevent this problem, cyclic shifts are applied to each spatial stream.

Table 3.5: Cyclic Shift Values for Preamble

N_{SS}	Cyclic shifts for each spatial stream in MIMO scenario (i_{SS})							
	1	2	3	4	5	6	7	8
1	0	-	-	-	-	-	-	-
2	0	-8	-	-	-	-	-	-
4	0	-8	-4	-6	-	-	-	-
8	0	-8	-4	-6	-7	-13	-2	-15

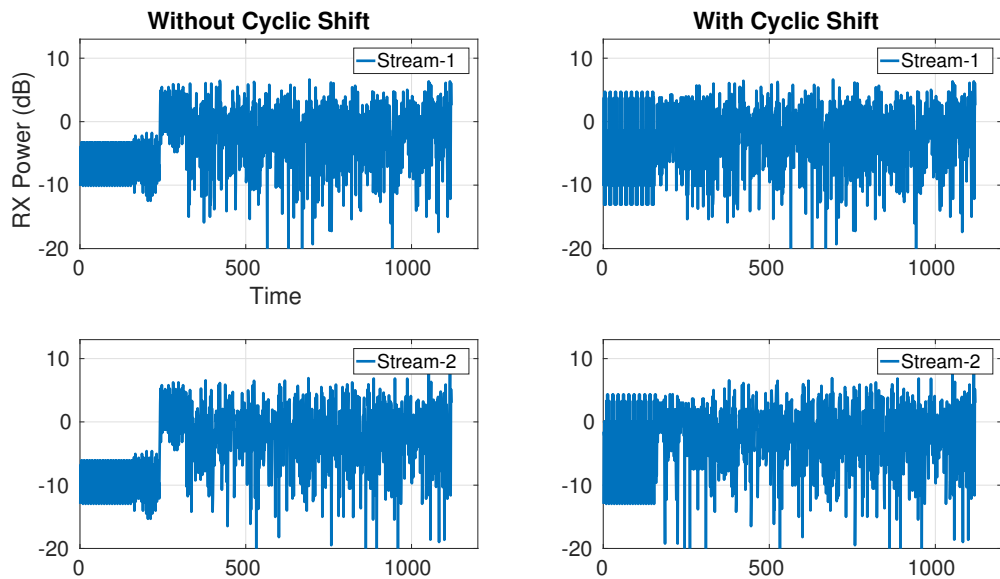


Figure 3.9: CSD performance

Corresponding shift values are shown in Table 3.5.

Cyclic shift values show the number of samples to be shifted cyclically for each OFDM symbol in the preamble part. By doing so, the correlation between spatial streams are minimized and destructive effects due to beamforming are prevented. Figure 3.9 highlights a comparison example of 2×2 MIMO scenario showing the effect of using cyclic shift operation. As seen from the figure, once the cyclic shift operation is applied to the signal, the received signal power is saved from destructive beamforming. Whereas the signal power diminishes dramatically when it is not used.

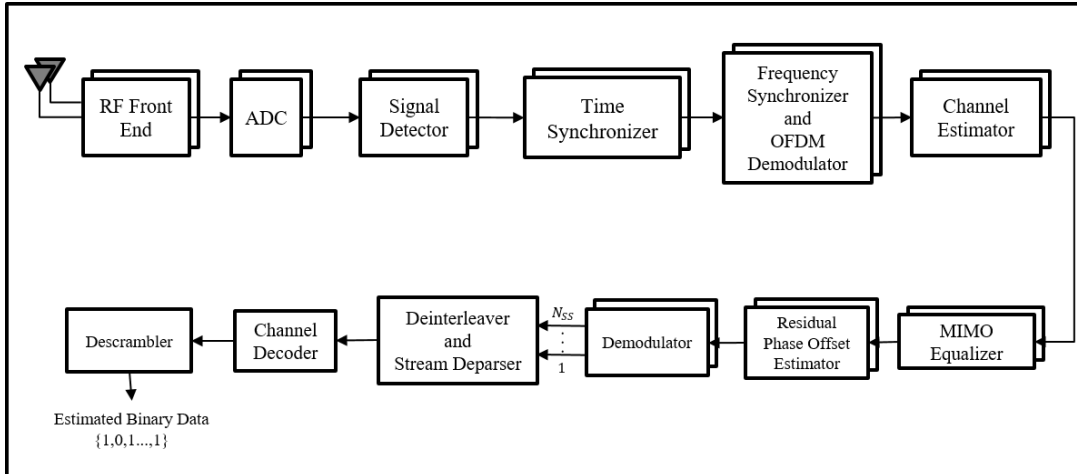


Figure 3.10: Data Link Receiver Block Diagram

3.4 Receiver

In this section, algorithms used in our receiver PHY will be given. Figure 3.10 shows the general block diagram of the receiver. As it is seen, after the signal is digitized in analog to digital converter, OFDM packets are detected first. Then, synchronization algorithms are performed with OFDM demodulation process including FFT and cyclic prefix removal operations. Next, the channel response is estimated and equalized from received packet for each subcarrier so that QAM modulated symbols are achieved. In the following steps, symbols are demodulated and bit operations are performed in the reverse order of the transmitter side in order to find the estimated data bits at the end.

3.4.1 Signal Detector

The first PHY operation on the receiver side is to detect the OFDM signal and synchronize in time. OFDM burst signals can be detected with various methods including correlation [33] [34] [35]. In our testbed, correlation based signal detection algorithm is implemented. STF part of the preamble which is saved on the receiver is used as matched filter to calculate the decision metric for the detection algorithm. Figure 3.11 depicts the correlator based signal detector structure for SISO scenario. As seen, decision metric $d[n]$ is the output of the matched filter. Under AWGN, detector system

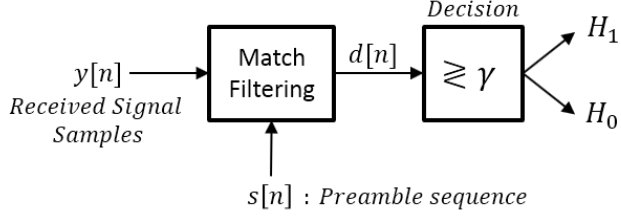


Figure 3.11: Correlator Based Signal Detector Structure

model can be written as,

$$y[n] = \begin{cases} \sqrt{E_s}s[n] + w[n], & H_1 \\ w[n], & H_0 \end{cases} \quad (3.12)$$

Periodic sequence in STF symbol will be used to calculate the decision metric. Once correlation is performed, $d[n]$ is found as,

$$d[n] = \begin{cases} \sum_{k=0}^{L-1} (\sqrt{E_s}s[k] + w[k])p_{STF}[n-k]^* = \sqrt{E_s} + \tilde{w}[n], & H_1 \\ \sum_{k=0}^{L-1} w[k]p_{STF}[n-k]^* = \tilde{w}[n], & H_0 \end{cases} \quad (3.13)$$

where $p_{STF}[n]$ is periodic sequence match filter with $\|p_{STF}[n]\| = \frac{1}{\sqrt{L}}$, L is the length of periodic sequence which is 16 for our case, $\sqrt{E_s}$ is the square root of the received signal energy and $\tilde{w}[n]$ is i.i.d. Gaussian samples. Decision is made by comparing the metric $d[n]$ to a threshold. In Figure 3.12 and Figure 3.13, Monte Carlo simulation is performed to show the probability of detection and false alarm for different threshold values in various SNR conditions. By using these plots, a threshold value can be chosen for suitable detection.

For MIMO case, since cyclic shift delays are applied in each stream, decision metric is computed as,

$$d[n]_{MIMO} = \sum_{i=0}^{N_{SS}} \sum_{j=0}^{N_{SS}} y_j[n] * p_{STF}^i[n]^* \quad (3.14)$$

p_{STF}^i is the periodic sequence of the i^{th} transmitted stream STF symbol and $y_j[n]$ is the j^{th} stream of received signal samples.

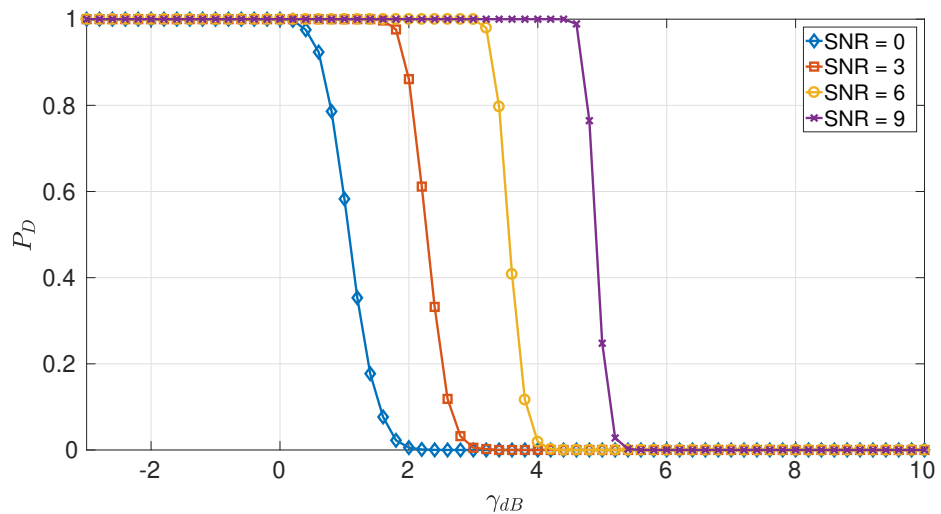


Figure 3.12: Simulation results for the probability of detection ($E\{w[n]^2\} = 1$).

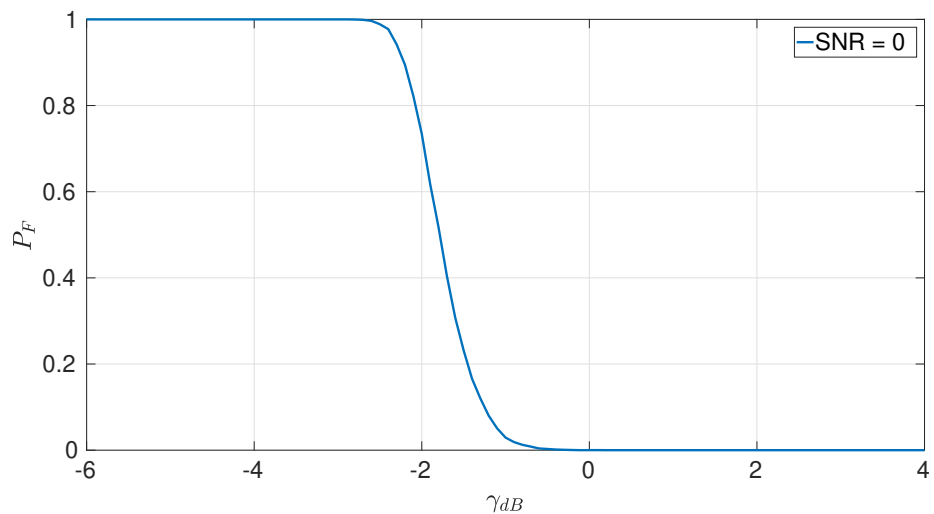


Figure 3.13: Simulation results for the probability of false alarm ($E\{w[n]^2\} = 1$)

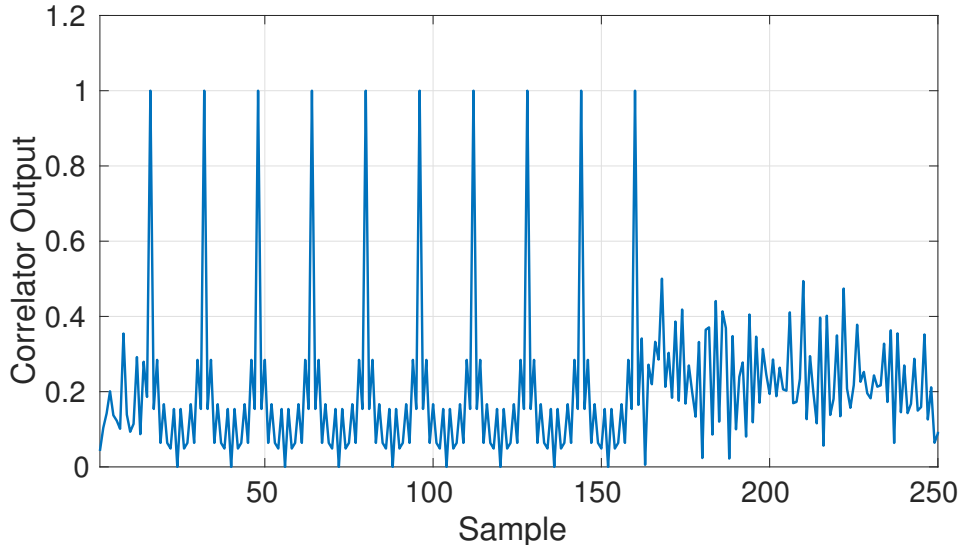


Figure 3.14: Ten consecutive peaks from the output of the correlator

3.4.2 Time Synchronizer

OFDM time synchronization is performed by estimating the beginning point of the packet. Similar to signal detection, the correlation method is used to compute the estimator metric in our synchronizer algorithm. Since there are two STF symbols in the preamble, correlator output yields 10 consecutive peaks that can be counted for synchronization (Figure 3.14).

For peak detection, algorithm first computes the detected signal power and updates the threshold value which was used before for the signal detector. A new threshold value is calculated as $\gamma_{new} = \sqrt{P_s}/2$, that is $\gamma_{new} = 0.5$ for the case in Figure 3.14. Once the first peak point is found, synchronizer calculates only the possible peak output values and compares with the threshold until peak counter reaches 10. The synchronizer is described in Algorithm 1. For MIMO scenario, the same decision metric as in signal detector (3.14) is used.

The performance of time synchronizer is shown in Figure 3.15 under Rayleigh fading channel condition. Monte Carlo trials are performed at each SNR and the algorithm performance is computed accordingly. The plot indicates that synchronizer works successfully at almost %90 of the total channel conditions for 10 dB average SNR

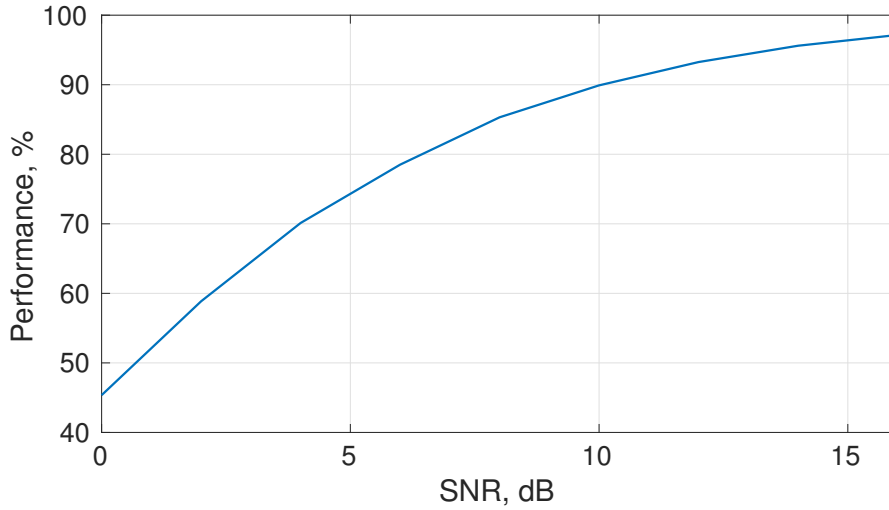


Figure 3.15: Time Synchronizer performance plot

and the performance increases for higher SNR values.

```

while scan detected signal do
    initialization;
    measure signal power;
    update threshold;
    while counter<10 do
        save next possible periodic sequence;
        correlate;
        if compare correlator output then
            | counter++;
        else
            | break;
        end
    end
    if counter=10 then
        | time synchronization is successfull
    end
end

```

Algorithm 1: Pseudo code for time synchronization algorithm.

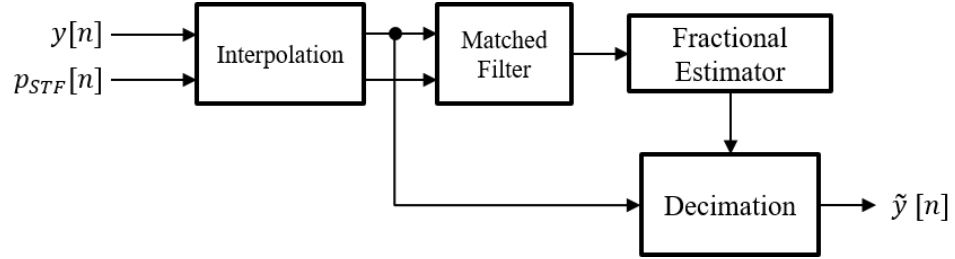


Figure 3.16: Fractional time synchronizer block diagram

3.4.2.1 Fractional Time Estimator

Since clocks are different for transmitter and receiver, fractional time offset can occur for received signal samples. To fix this problem, an interpolation based timing estimator is used [36]. The algorithm block diagram is shown in Figure 3.16. After time synchronization, the signal is interpolated first. An interpolation factor by 4 in our testbed determines the estimator resolution. Interpolated signal samples are matched filtered for finding the fractional time offset. Lastly, decimation occurs from synchronized samples to return to the original sampling rate.

For MIMO case, assuming that the time offset is the same between all transmitter and receiver streams, the output of the matched filter is summed up for all received streams and the fractional time offset is found from that metric.

3.4.3 Frequency Synchronizer

Doppler frequency shift and inconsistencies between local oscillators of transmitter and receiver cause carrier frequency offset (CFO) problem in communication systems. Due to this, the orthogonal positions of adjacent subcarriers in the OFDM system are distorted, creating ICI (Inter Carrier Interference). ICI affects the OFDM performance substantially by adding interference to each subcarrier symbol [37]. For this reason, estimating the introduced frequency offset at the receiver side is very important. The system model under CFO can be shown as,

$$y[n] = (h[n] * s[n])e^{j\frac{2\pi n}{N}\epsilon} + w[n] \quad (3.15)$$

where ϵ is the normalized CFO³ and N is the FFT length in OFDM symbol. Figure 3.17 highlights an ICI problem caused by a CFO of ϵ . It is observed that fre-

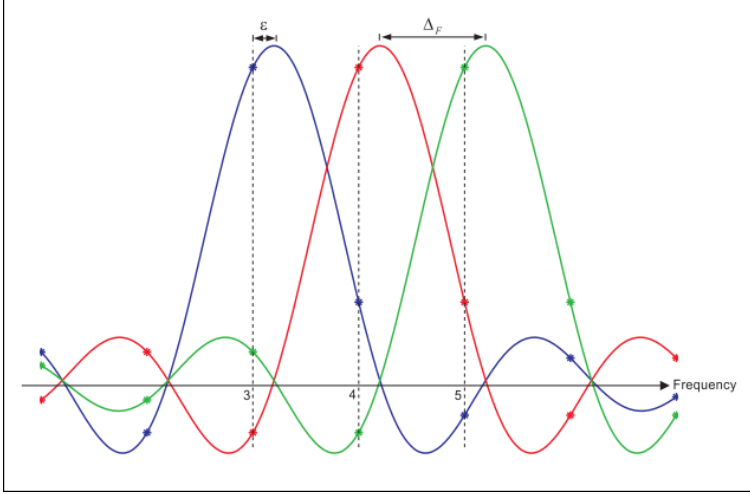


Figure 3.17: ICI problem caused by CFO [38]

frequency shift breaks the orthogonality condition between subcarriers. In our testbed, coarse and fine frequency estimators are designed. While coarse estimator uses only the preamble part, fine frequency synchronizer estimates the CFO from the whole OFDM packet.

3.4.3.1 Coarse Estimator

CFO is coarsely estimated by using STF part of the preamble in the time domain. As known, there are two STF symbols in OFDM packet structure and one STF symbol includes 5 consecutive short sequences. The estimator algorithm finds the CFO by calculating the phase offset between these repetitive sequences [39]. The mathematical model for the coarse estimator can be written as follows,

$$\hat{\phi}_{Coarse} = \frac{1}{DL} \arg \left\{ \sum_{k=0}^{N_{stf}-D-1} \sum_{n=0}^{L-1} y[n + kL] y^*[n + (k+D)L] \right\} \quad (3.16)$$

$$\hat{\phi}_{Coarse} = \frac{2\pi\epsilon}{N} \quad (3.17)$$

$$\hat{\epsilon} = \frac{\hat{\phi}_{Coarse} N}{2\pi} \quad (3.18)$$

where N_{stf} is the number of periodic sequences for two STF symbols which is 10 for our structure, D is the delay parameter representing which repetitive sequences will be used for phase offset calculation. In our testbed, we set $D = 3$ so that estimator calculates the phase offset with sequences whose order numbers are 1-4, 2-5, ..., 7-10.

³Normalized CFO is the ratio between CFO and subcarrier frequency spacing, $\frac{f_{CFO}}{\Delta f_{SC}}$

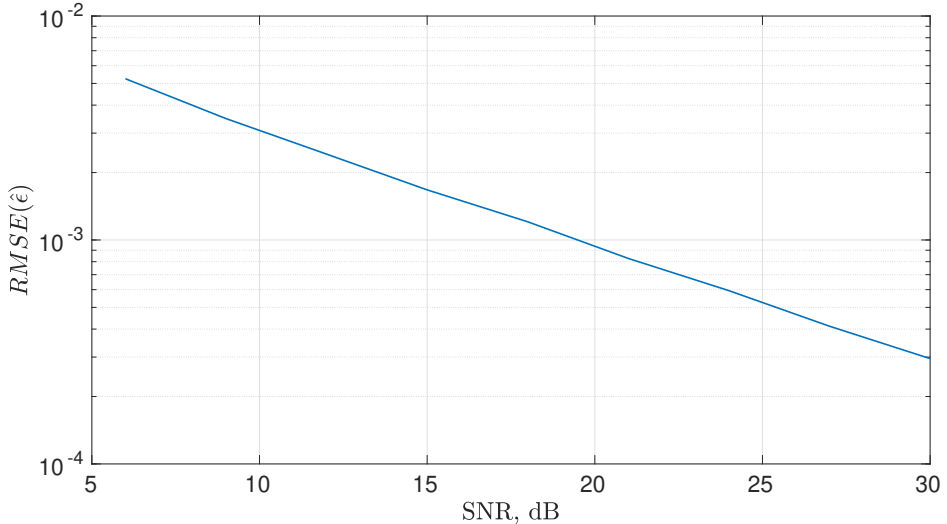


Figure 3.18: Performance of the coarse estimator

For MIMO case, $\arg\{\cdot\}$ term is summed in complex for all streams and $\hat{\phi}_{Coarse}$ is found as the phase estimate in radians.

Since this algorithm estimates the frequency from phase shift in time, the ambiguity occurs outside of $\pm\pi$. That is, the algorithm can estimate the maximum CFO as $\hat{\phi}_{Coarse} = \frac{\pm\pi}{DL}$ resulting $|f_{CFO}| \leq \frac{0.5f_s}{DL}$. For 20 MHz bandwidth scenario, $|f_{CFO}| \leq 208.33$ kHz can be estimated. According to the IEEE802.11ac standard [7], the deviation of transmitter center frequency cannot exceed ± 20 ppm. Therefore, frequency offset caused by local oscillators is limited with the standard as ± 40 ppm or $f_{CFO,max} = 138$ kHz at the carrier frequency of 3.45 GHz if the same tolerance is valid for receiver too.

Figure 3.18 illustrates performance of the 2×2 MIMO coarse estimator under AWGN. $RMSE(\hat{\epsilon})$ is computed for each SNR value. ϵ is taken as $1/3$. As seen, $RMSE(\hat{\epsilon})$ is linearly decreasing as SNR increases.

3.4.3.2 Fine Estimator

After frequency is coarsely synchronized, residual CFO still degrades demodulation performance due to high frequency sensitivity of OFDM waveform [40]. Therefore, fine estimator is used after coarse frequency synchronization step. In the literature,

for fine estimation of the CFO in OFDM systems, there are different methods suggested in both time and frequency domains [41]. We implemented two methods in our testbed: CP and pilot based.

Similar to the coarse estimator, CFO can be estimated by using CP portion of an OFDM symbol which is a repetitive length- L sequence in one symbol duration [42]. Since each symbol includes CP, estimator uses the whole packet for fine estimation of CFO. The system model can be written as

$$\hat{\phi}_{fine} = \frac{1}{N} \arg \left\{ \sum_{i=1}^{N_{SYM}} \sum_{j=0}^{L-1} y_i[j] y_i^*[j+N] \right\} \quad (3.19)$$

where y_i is the i^{th} OFDM symbol in a packet.

Pilots at each OFDM symbol can be used for fine frequency estimation. The phase offset contributed from CFO can also be related between pilots in the frequency domain [43]. We can write the system model with CFO under AWGN as,

$$y_l[n] = \frac{1}{N} \sum_k X_l[k] e^{j2\pi n(k+\epsilon)/N} + w_l[n]. \quad (3.20)$$

If FFT is applied to l^{th} and $(l+D)^{th}$ symbols,

$$Y_l[k] = \tilde{X}_l[k] + I_l[k] + W_l[k], \quad (3.21)$$

$$Y_{l+D}[k] = \tilde{X}_{l+D}[k] e^{j2\pi D\epsilon} + I_{l+D}[k] + W_{l+D}[k], \quad (3.22)$$

$$I_l[k] = \sum_n X[n] \frac{\sin(\pi\epsilon)}{N \sin(\pi(l-k+\epsilon)/N)} e^{j\pi\epsilon(N-1)/N} e^{-j\pi(l-k)/N}, \quad (3.23)$$

where $I_l[k]$ is the ICI term contributed due to CFO. Since BPSK modulated pilots are cyclically shifted over symbols, estimator metric uses crosscorrelation in order to align the phase values of pilots. The metric can be written for SISO scenario as,

$$\hat{\phi}_{fine} = \frac{1}{D(N+L)} \arg \left\{ \sum_k \sum_{l=1}^{N_{SYM}-D} Y_{l+D}[k] Y_l^*[k] X_{l+D}^*[k] X_l[k] \right\} \quad (3.24)$$

where $X_l[k]$ is the pilot symbols saved on receiver, D is the delay parameter that determines symbol couples compared for phase offset calculation. Similar to the parameter used in the coarse estimator, this limits the maximum frequency that can be estimated with this algorithm. Also, even in the absence of AWGN, performance of the estimator can be affected from ICI. Upper bound is calculated for the variance of ICI in [43] as,

$$E[I[k]^2] \leq 0.5947 |X|^2 \sin(\pi\epsilon)^2, \quad |\epsilon| \leq 0.5 \quad (3.25)$$

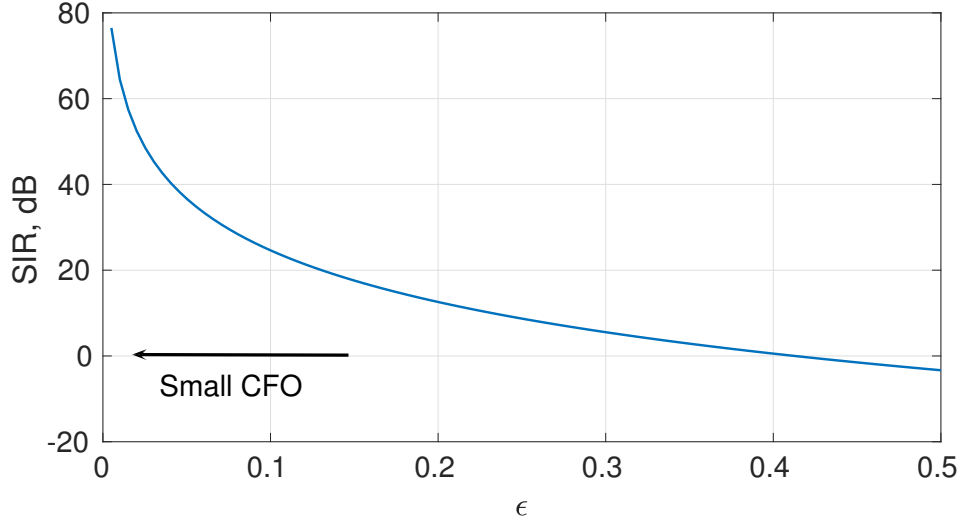


Figure 3.19: SIR vs. CFO plot

Figure 3.19 shows SIR plot ($\frac{E[\tilde{X}[k]^2]}{E[I[k]^2]}$) using the upper bound calculated in Equation 3.25. For small values of ϵ , ICI does not dominate the signal of interest as seen. However, for higher values, SIR dramatically decreases even below 0 for $\epsilon > 0.4$. Since we use this algorithm after coarse estimation of CFO, ICI does not affect the performance of the estimator compared to CP based method that does not include any ICI.

In MIMO scenario, similar to coarse estimator metric, $\arg\{\cdot\}$ term is summed in complex for all streams. That is, $\hat{\phi}_{fine}^{CP}$ and $\hat{\phi}_{fine}^{pilot}$ are written as

$$\hat{\phi}_{fine}^{CP} = \frac{1}{N} \arg \left\{ \sum_{m=1}^{N_{SS}} \sum_{i=1}^{N_{SYM}} \sum_{j=0}^{L-1} y_{i,m}[j] y_{i,m}^*[j+N] \right\} \quad (3.26)$$

$$\hat{\phi}_{fine}^{pilot} = \frac{1}{D(N+L)} \arg \left\{ \sum_{m=1}^{N_{SS}} \sum_k \sum_{l=1}^{N_{SYM}-D} Y_{l+D,m}[k] Y_{l,m}^*[k] X_{l+D,m}^*[k] X_{l,m}[k] \right\} \quad (3.27)$$

Figure 3.20, highlights the performance of the estimators for different CFO values in 2×2 MIMO scenario. Delay parameter D of pilot based estimator is taken as 2 for $\epsilon = 0.15$ and 20 for $\epsilon = 0.016$. As seen from the figure, for higher CFO, CP based estimator outperforms the pilot estimator only for higher values of SNR due to the existence of ICI for pilot estimator. But for small values of CFO, the performance of pilot based estimator is much better compared to the CP based algorithm. Note that, as SNR increases more, CP curve still remains linear but the pilot curve has an asymptotic limit caused by ICI. As a consequence of this, CP based algorithm will be better at some point where SNR and ICI are high. Also, the amount of CFO does not affect the $RMSE$ performance of CP based estimator as seen. Based on these results,

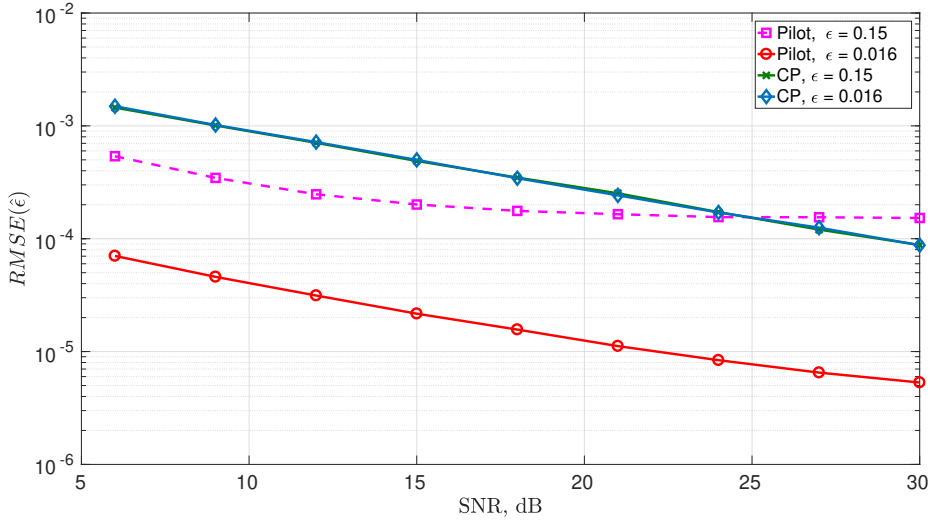


Figure 3.20: Performance of the fine estimators

we have used pilot based fine frequency estimator rather than CP based algorithm in our testbed.

3.4.4 Channel Estimator

MIMO OFDM channel estimation is performed by using LTF symbols in the preamble. Maximum Likelihood (ML) estimator is used for each subcarrier in the frequency domain [44]. $N_t \times N_r$ MIMO system model can be shown in the time domain as,

$$\mathbf{y}[n] = \mathbf{h}[n] \circledast \mathbf{s}[n] + \mathbf{w}[n] \quad (3.28)$$

where $\mathbf{h}[n]$ is the MIMO channel matrix with the size of $N_r \times N_t$ whose elements of i and j correspond to the channel gain between i^{th} receive and j^{th} transmit antennas. N_t and N_r are the number of transmit and receive antennas respectively. In the frequency domain, the following

$$\mathbf{Y}[k] = \mathbf{H}[k]\mathbf{S}[k] + \mathbf{W}[k], \quad k = 1, 2, \dots, N \quad (3.29)$$

narrow band signal model exists for each subcarrier k . $\mathbf{H}[k]$ is the channel matrix corresponding to the k^{th} subcarrier. ML estimator is written for the each element of $\mathbf{H}[k]$ as

$$\hat{h}_{i,j}[k] = \frac{[Y_{i,1}[k] \quad Y_{i,2}[k] \quad \dots \quad Y_{i,N_{SS}}[kk]] (\mathbf{p}_{LTF}^j)^T}{N_{SS} S_{LTF}^j[k]} \quad (3.30)$$

where $Y_{i,1}[k]$ is the i^{th} received stream sample of the 1^{st} LTF symbol for the k^{th} subcarrier, $S_{LTF}^j[k]$ is the j^{th} transmitted stream LTF symbol of the k^{th} subcarrier and \mathbf{p}_{LTF}^j is the j^{th} row of the $\mathbf{P}_{LTF}^{N_{SS}}$ defined in Table 3.4. The superscript T means transpose. As an example, the channel coefficients of 2×2 MIMO OFDM system are estimated as follows,

$$\begin{aligned}\hat{h}_{1,1}[k] &= \frac{Y_{1,1}[k] - Y_{1,2}[k]}{2S_{LTF}^1[k]}, & \hat{h}_{1,2}[k] &= \frac{Y_{1,1}[k] + Y_{1,2}[k]}{2S_{LTF}^2[k]} \\ \hat{h}_{2,1}[k] &= \frac{Y_{2,1}[k] - Y_{2,2}[k]}{2S_{LTF}^1[k]}, & \hat{h}_{2,2}[k] &= \frac{Y_{2,1}[k] + Y_{2,2}[k]}{2S_{LTF}^2[k]}\end{aligned}\quad (3.31)$$

The channel coefficients of all data and pilot subcarriers in 2×2 MIMO OFDM system are found using the Equation 3.31.

Therefore, MIMO channel matrix is estimated by using the ML algorithm in the frequency domain. However, this process may not yield robust results in some channels where the coherence bandwidth is too large compared to the signal bandwidth. In such environments, estimator performance can be increased by decreasing the noise effect on the estimated channel coefficients in the time domain. In our testbed, two different methods have been implemented to increase the performance of ML channel estimator. These are,

- Least Squares (Model Based) estimator
- Time Domain Truncation (TDT) estimator

3.4.4.1 Least Squares Estimator

In this method, a linear relationship is established between the channel coefficients estimated in the frequency domain and the time domain [45]. This relationship can be expressed as,

$$\hat{\mathbf{H}}_{i,j} \approx \mathbf{T} \mathbf{h}_{i,j} \quad (3.32)$$

where $\hat{\mathbf{H}}_{i,j}$ is the channel coefficients estimated with ML method for all subcarriers, $\mathbf{h}_{i,j}$ is the channel coefficients depending on the maximum channel delay spread and \mathbf{T} is the Fourier transform matrix which maps $\mathbf{h}_{i,j}$ time samples to $\hat{\mathbf{H}}_{i,j}$ frequency components. Note that \mathbf{T} is in the form of $(N - N_{null}) \times L$, $\mathbf{h}_{i,j}$ is $L \times 1$ and $\hat{\mathbf{H}}_{i,j}$ is

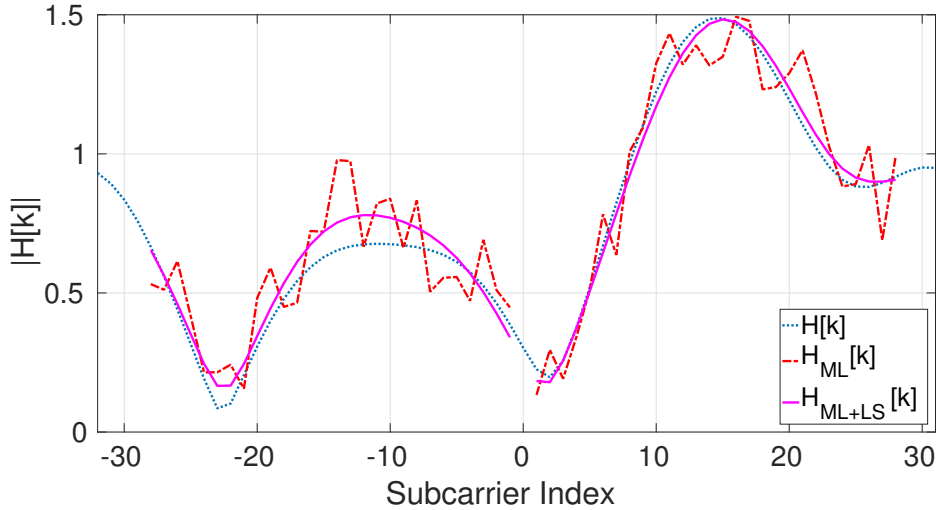


Figure 3.21: Comparison between ML and ML+LS estimator

$(N - N_{null}) \times 1$. L is the estimated maximum delay spread. Then, least squares (LS) solution of Equation 3.32 is,

$$\hat{\mathbf{h}}_{i,j} = (\mathbf{T}^H \mathbf{T})^{-1} \mathbf{T}^H \hat{\mathbf{H}}_{i,j} \quad (3.33)$$

So, the channel coefficients in the domain are estimated with LS method by using the ML estimation result. Upgraded channel coefficients in the frequency domain are obtained by using the transform matrix \mathbf{T} as,

$$\hat{\mathbf{H}}_{i,j} = \mathbf{T} \hat{\mathbf{h}}_{i,j} \quad (3.34)$$

Figure 3.21, illustrates a simulation example of channel estimator results for SISO scenario with the perfect channel coefficients $H[k]$. Frequency selective channel is used with 5 taps⁴. Maximum delay spread for LS estimator is assumed as 7 taps ($L = 7$). As seen, LS method increases the performance of the channel estimator.

3.4.4.2 TDT Estimator

Compared to the LS method, TDT is a simpler estimation algorithm. As is evident from its name, ML estimated channel coefficients are transformed to time domain and then truncation is performed according to maximum channel delay spread. As known,

⁴In the simulator, discrete time channel $h[n]$ is used with 5 samples length. Sampling rate is same for transmitter, channel and receiver.

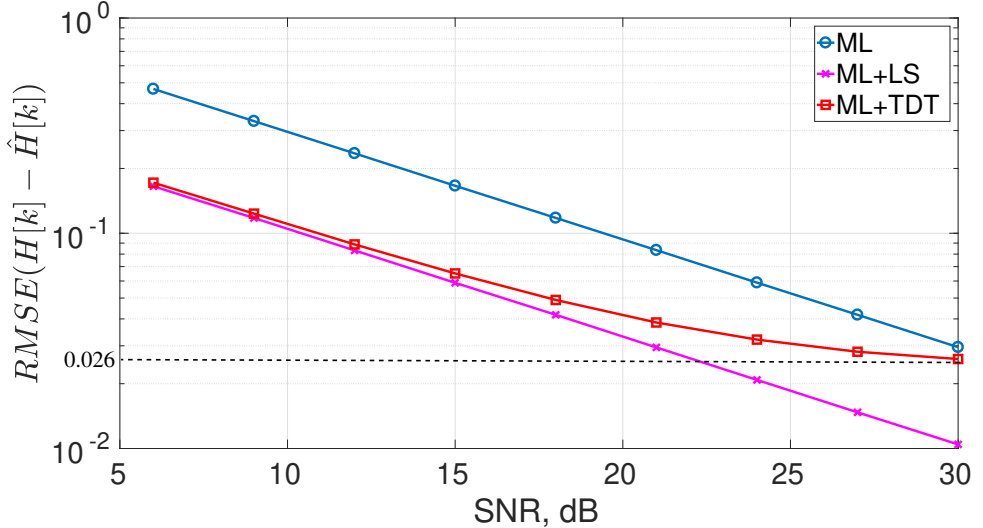


Figure 3.22: Performance of the channel estimators

when IFFT is applied to $\hat{H}[k]$, we obtain time domain representation of estimated channel response which is in length of OFDM symbol duration. So depending on the maximum delay spread of channel, remaining part of the estimated channel response is nulled as

$$\hat{\hat{h}}_{i,j}[n] = \begin{cases} \hat{h}_{i,j}[n], & n < L \\ 0, & n \geq L \end{cases} \quad (3.35)$$

where L is the estimated maximum channel delay spread. After this operation, time domain channel coefficients are converted to frequency domain via FFT.

$$\hat{H}_{i,j}[k] = \sum_{n=0}^{L-1} \hat{\hat{h}}_{i,j}[n] e^{-j2\pi nk/N}. \quad (3.36)$$

Performances of channel estimators are shown in Figure 3.22. RMSE of estimated channel coefficients are found from Monte Carlo trials under a 3-tap Rayleigh channel model in SISO scenario. Both LS and TDT methods increase the ML estimator performance up to $\text{SNR} = 30$ dB. Since ML+TDT curve has an asymptotic limit which is approximately 0.026, ML method has better performance for higher SNR values. On the other hand, ML+LS method yields a substantial improvement for all values of SNR. As SNR gets smaller, both methods give similar performance.

3.4.4.3 Maximum Channel Delay Spread Estimator

In both LS and TDT algorithms, it is assumed that the length of channel impulse response (L) or maximum channel delay spread is known. For this reason, this parameter must be estimated on the receiver side. The noise variance is used to estimate the length of the channel for both methods [46]. For the LS estimator,

$$\hat{L}^{LS} = \operatorname{argmin}_L \left(E\{|\hat{H}_{i,j}^{ML} - \hat{H}_{i,j}^{LS}(L)|^2\} - \sigma_W^2 \right) \quad (3.37)$$

is used to estimate L . In this equation, $\hat{H}_{i,j}^{LS}(L)$ is the LS estimated channel coefficients for different L values and σ_W^2 is the noise variance.

In TDT method, the power of estimated time domain channel taps are compared with noise variance respectively. L is estimated for the first value that remains below the noise variance. Then truncation is performed by leaving some margin from this value.

3.4.5 MIMO Equalizer

In a single carrier communication system, an equalizer is necessary when there is an ISI problem caused by channel delay spread. Such channels are also called frequency-selective. With equalization, the ISI problem is alleviated so the frequency-selective channel turns into flat spectrum with maximizing the SNR of the equalized signal. Assuming that there is no ICI problem after a good frequency synchronization in MIMO OFDM system, the resulting communication model will be

$$\mathbf{Y}[k] = \mathbf{H}[k]\mathbf{S}[k] + \mathbf{W}[k]. \quad (3.38)$$

Thanks to OFDM, each received subcarrier sample can be modeled as a flat type (with no ISI) narrowband channel in a frequency selective channel condition as seen in Equation 3.38. However, in MIMO, each received stream includes the combination of all transmitted streams with corresponding channel coefficients, hence spatial interference occurs at receiver.

MIMO equalizer removes this spatial interference for proper demodulation. In our testbed, linear type equalizers are used because they are generally less complex to implement [47]. These are

- Zero Forcing (ZF) Equalizer,
- Minimum Mean Square Error (MMSE) Equalizer.

3.4.5.1 ZF

Since the channel is estimated for each subcarrier k for an OFDM symbol, a ZF equalizer filter is found by the LS solution of $\|\mathbf{Y}[k] - \mathbf{H}[k]\mathbf{S}[k]\|^2$ and can be written as [48]

$$\mathbf{M}[k] = \hat{\mathbf{H}}^\dagger[k] = (\hat{\mathbf{H}}^H[k]\hat{\mathbf{H}}[k])^{-1}\hat{\mathbf{H}}^H[k], \quad (3.39)$$

where the superscript \dagger means pseudo-inverse operation. Then this filter is applied to the received vector

$$\mathbf{M}[k]\mathbf{Y}[k] = \hat{\mathbf{H}}^\dagger[k]\mathbf{H}[k]\mathbf{S}[k] + \hat{\mathbf{H}}^\dagger[k]\mathbf{W}[k], \quad (3.40)$$

$$\mathbf{R}[k] = \mathbf{S}[k] + \hat{\mathbf{H}}^\dagger[k]\mathbf{W}[k]. \quad (3.41)$$

As seen, a ZF equalizer is ideal when the channel is noiseless. So it works well for high SNR conditions. However, when $\mathbf{H}[k]$ fades sharply for any subcarrier, or $\mathbf{H}[k]$ is ill conditioned the noise power will be increased significantly which is called the noise enhancement problem. This will decrease the performance of ZF equalizer. To mitigate the effect of noise enhancement, MMSE equalizer is preferred in the next section.

3.4.5.2 MMSE

This equalizer minimizes the average mean square error (MSE) of estimated symbols $S[k]$. That is, MMSE equalizer filter is found by minimizing $E\{|\hat{S}[k] - S[k]|^2\}$. This can be written as [47]

$$\mathbf{M}[k] = (\mathbf{H}^H[k]\mathbf{H}[k] + \sigma_W^2\mathbf{I})^{-1}\mathbf{H}^H[k], \quad (3.42)$$

where \mathbf{I} is the identity matrix whose size is determined by the number of transmit streams and σ_W^2 is the noise variance. In the absence of noise term, MMSE filter is identical to ZF filter. If the channel is highly attenuated for some subcarrier frequencies, $\sigma_W^2\mathbf{I}$ term blocks the noise from being enhanced. Figure 3.23 illustrates how the noise enhancement problem affects the system for both ZF and MMSE equalizers.

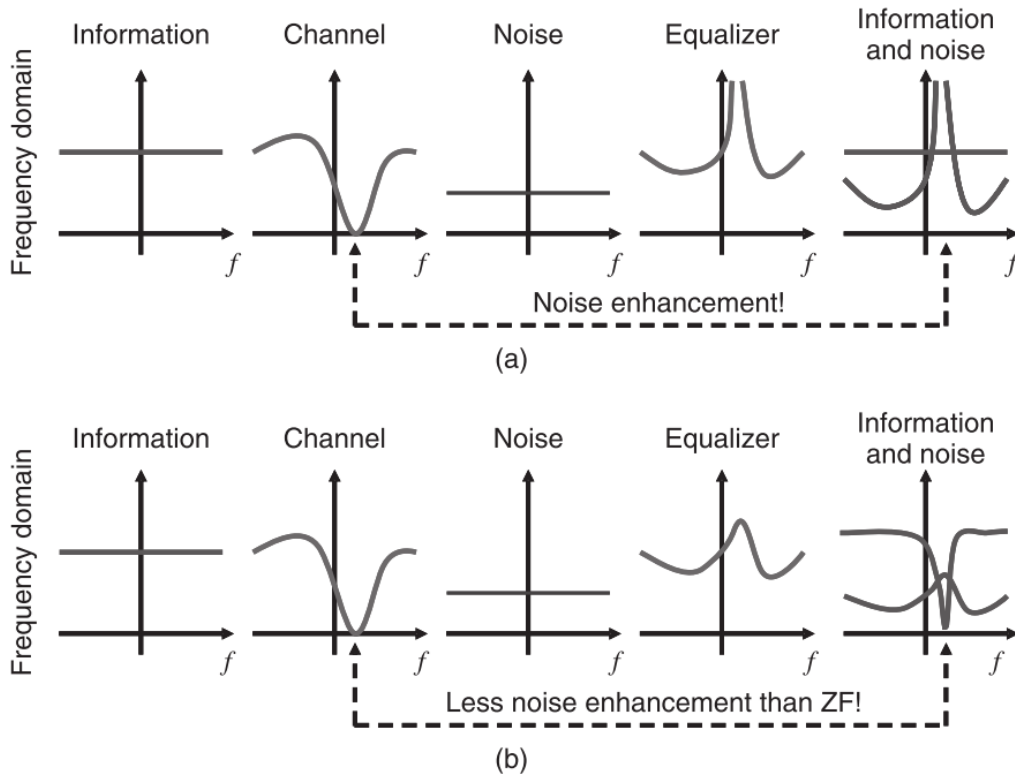


Figure 3.23: Noise Enhancement Problem in ZF (a) and MMSE (b) Equalizers [49]

3.4.6 Residual Phase Offset Estimator

After equalization, there may still be residual phase offset on the symbols that affects the detection performance. Pilot symbols are used to estimate this residual phase offset term. A mathematical model can be written as

$$\hat{X}[k] = X[k]e^{j\phi_{res}} + W[k] \quad (3.43)$$

where ϕ_{res} is the fixed residual phase offset term on symbols. Then, estimator detection metric is

$$\hat{\phi}_{res} = \arg \left\{ \sum_k \sum_{l=1}^{N_{SYM}} \hat{X}_l[k] X_l^*[k] \right\} \quad (3.44)$$

where $\hat{X}_l[k]$ is the estimated l^{th} pilot symbol whose subcarrier index is k . Lastly, $\hat{\phi}_{res}$ term is removed from equalized symbols by multiplying the conjugate of it:

$$\hat{\hat{X}}[k] = \hat{X}[k]e^{-j\hat{\phi}_{res}}. \quad (3.45)$$

3.4.7 Demodulator

Demodulator block computes the decision metric as either hard or soft according to the usage in our testbed. Hard decision is performed using the ML method. It works by finding the minimum distance between reference and observation symbols. Therefore, estimated symbols are mapped to Gray-coded binary data:

$$\hat{s} = \operatorname{argmin}_{s_i} |y - s_i|. \quad (3.46)$$

In soft decision, log-likelihood ratio (LLR) is computed for each bit of the estimated symbol. This can be written as,

$$LLR_i = \ln \left(\frac{\sum_{s_j \in B_0^i} e^{-\frac{|y-s_j|^2}{\sigma_n^2}}}{\sum_{s_j \in B_1^i} e^{-\frac{|y-s_j|^2}{\sigma_n^2}}} \right), \quad (3.47)$$

where B_0^i is the set of symbols with a binary 0 value at its i^{th} bit. For small values of σ_n^2 , singularities may occur in the equation above due to exponential function computations. For this purpose, approximate LLR is used. Approximation is based on the relation below [50],

$$\ln \left(\sum_j e^{-x_j} \right) \approx - \min_j x_j \quad (3.48)$$

and the resultant equation is

$$LLR_{i,App} = \min_{j, B_1^i} (|y - s_j|^2) - \min_{j, B_0^i} (|y - s_j|^2). \quad (3.49)$$

Figure 3.24 depicts BER performance of hard-decision and LLR methods for 16-QAM symbols under AWGN channel. Data bits are encoded with convolutional encoder whose generator polynomials are [133, 171] with constraint length 7. The coding rate is 1/2. Viterbi decoder is run with hard-decision binary data and LLR values separately. The plot shows that LLR metric outperforms HD for all SNR values. It is almost 2 dB better as SNR increases.

In MIMO scenario, above methods are applied to each stream separately. Apart from these MIMO-ML decision is also used in our testbed. This metric can be written as

$$\hat{\mathbf{x}} = \operatorname{argmin}_{\mathbf{x}_i} |\mathbf{y} - \mathbf{Hx}_i|. \quad (3.50)$$

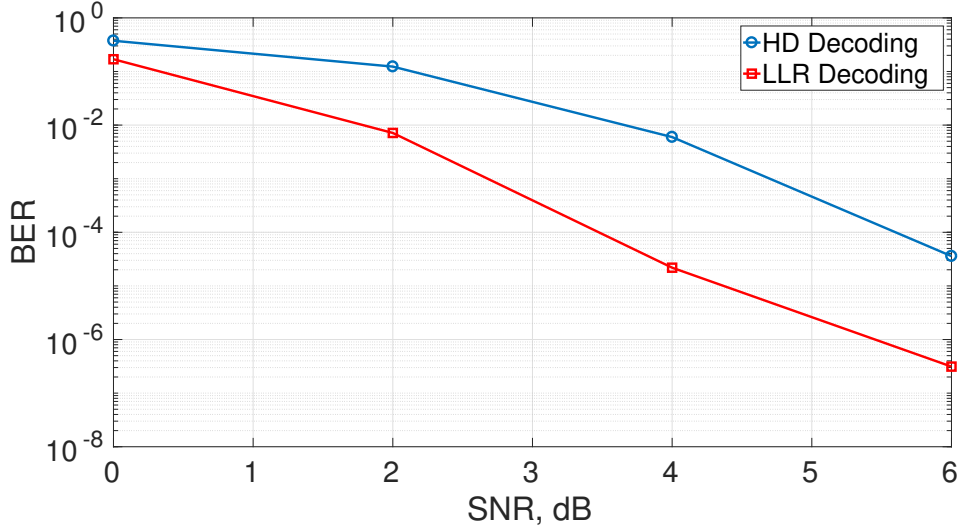


Figure 3.24: BER performance comparison between LLR and HD for 16-QAM symbols under AWGN

MIMO-ML detector tries to find the most possible symbol vector \mathbf{x}_i from the set of all possible vectors. For an M-QAM $N \times N$ MIMO system, detector must perform M^N computations. In order to decrease the computation complexity, we also implement group based detection using MMSE filtering with partial interference cancellation and then ML detection [51]. The idea is to model MIMO system as a group of multiple users transmitting and filter the received vector by suppressing each group separately. After that, ML detection is applied to these filtered vectors for small number of streams which decreases the computational complexity compared to MIMO-ML. A modified system model for group based decoding can be written as

$$\mathbf{y} = \mathbf{H}_1 \mathbf{x}_1 + \mathbf{H}_2 \mathbf{x}_2 + \mathbf{n} \quad (3.51)$$

where \mathbf{H}_i is the partial channel matrix including channel coefficients for a group of transmit antennas. For 4×4 MIMO system, \mathbf{H}_1 is 4×2 matrix including channel coefficients of first two streams. For filtering $\mathbf{H}_2 \mathbf{x}_2$, projection matrix onto the null space of \mathbf{H}_2 is generated as

$$\mathbf{W}_1 = \mathbf{I} - \mathbf{H}_2 \mathbf{P}_2 \quad (3.52)$$

where \mathbf{P}_2 is the MMSE filter for channel \mathbf{H}_2 :

$$\mathbf{P}_2 = (\mathbf{H}_2^H \mathbf{H}_2 + \sigma_n^2 \mathbf{I})^{-1} \mathbf{H}_2^H. \quad (3.53)$$

Then \mathbf{W}_1 is multiplied with \mathbf{y} and we have

$$\mathbf{W}_1\mathbf{y} = \mathbf{W}_1(\mathbf{H}_1\mathbf{x}_1 + \mathbf{H}_2\mathbf{x}_2 + \mathbf{n}), \quad (3.54)$$

$$\mathbf{y}_1 = \mathbf{W}_1\mathbf{H}_1\mathbf{x}_1 + \mathbf{W}_1\mathbf{n}. \quad (3.55)$$

Then ML detection is performed for each filtered group vector as

$$\hat{\mathbf{x}}_k = \underset{\mathbf{x}_{k_i}}{\operatorname{argmin}} |\mathbf{y}_k - \mathbf{W}_k \mathbf{H}_k \mathbf{x}_{k_i}|, \quad k = 1, 2 \quad (3.56)$$

where \mathbf{x}_{k_i} is the set of possible k^{th} group symbol vector. As seen, for an M-QAM 4×4 MIMO system, computation complexity reduced from M^4 to $2M^2$ by group based decoding. This advantage comes with a performance trade-off. The negative effect of partial interference cancellation is the loss of signal power after filtering with the projection matrix \mathbf{W}_k [51]. Since we have,

$$||\mathbf{W}_k \mathbf{H}_k \mathbf{x}_k|| \leq ||\mathbf{H}_k \mathbf{x}_k|| \quad (3.57)$$

This is equal only when \mathbf{H}_k 's are orthogonal to each other. Figure 3.25 highlights the performance of single stream ML, MIMO-ML and group MMSE MIMO-ML detectors under narrowband Rayleigh channel condition in 4-QAM 4×4 MIMO testbed. For single stream ML detection, MMSE equalizer is used. Channel estimation is performed with ML+LS algorithm. As seen, MIMO-ML gives the best BER (Bit Error Rate) performance. On the other hand, group based detection outperforms single stream ML but it has a huge performance loss compared to MIMO-ML algorithm with the advantage of decreased complexity.

3.4.8 Deinterleaver and Stream Deparser

The burst type errors introduced by channel are distributed over the whole packet by deinterleaving. By doing so, the real-time performance of the channel decoding process can be increased. Mathematically, inverse of the operations of the interleaver are applied to serial data for each spatial stream in MIMO scenario [7].

In MIMO scenario, deinterleaved parallel streams are recovered back to serial bit stream with stream deparsing. Subsequent operations are performed with single stream.

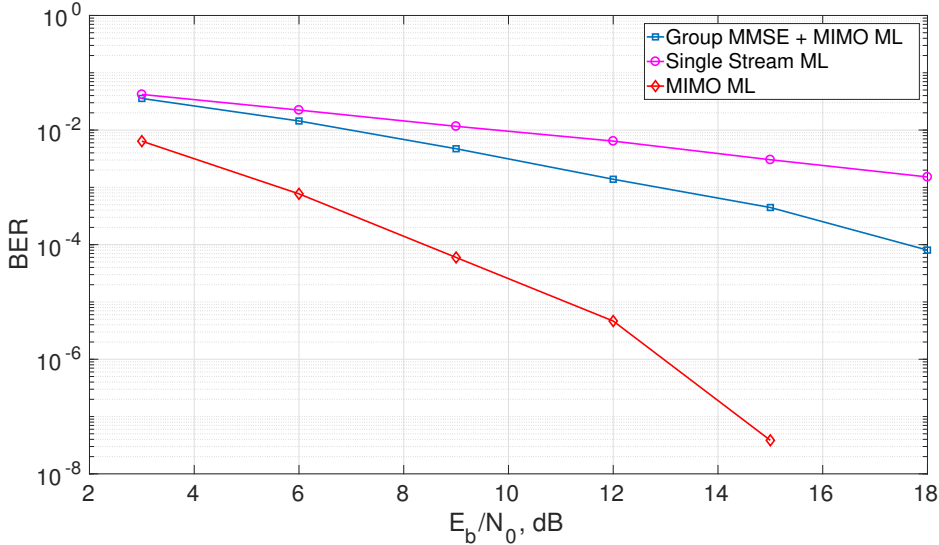


Figure 3.25: BER performance comparison between MIMO Detectors in 4-QAM 4×4 Communication Scenario

3.4.9 Channel Decoder

Convolutionally encoded data in the transmitter side is decoded by using the Viterbi algorithm. Basically, it estimates the binary data from computations of path metrics with ML algorithm by finding the most possible data path [52]. As explained in Section 3.3.3.1, puncturing patterns provide different coding rates for various modulation settings. In the receiver side, Viterbi decoder inserts zero observation in places of the encoded data bits and then decoding is performed. It works with both HD binary data and LLR values by computing Hamming and Euclidian distances for path metric calculation respectively. As it can be seen from the Figure 3.24, decoding performance is better with LLR compared to HD. Traceback depth value is chosen from the rule of $2.5(K - 1)/(1 - r)$ where K is the constraint length of convolutional code which is 7 in our testbed and r is the coding rate [53].

3.4.10 Descrambler and Padding Removal

Final operation on the receiver is to descramble the decoded data and to remove the padding bits. Descrambling operation is done according to the polynomial used in scrambling process. After padding removal, physical layer part is over and data bits are transferred to upper layer.

CHAPTER 4

MIMO-OFDM DATA LINK SIMULATOR IMPLEMENTATION AND PERFORMANCE RESULTS

This chapter will present the simulation work for our testbed. All transmitter and receiver PHY algorithms proposed in Chapter 3 are implemented in the simulation environment for building data link testbed simulator. In addition to these, some RF impairments and channel types are modeled to see the performance of our testbed in different conditions. This step is very critical before testing the data link on hardware and provides system designers to see the problems on early stages. Also, graphical user interface (GUI) is designed for testing our testbed algorithms easily in different communication scenarios. We preferred to use MATLAB software as the simulation environment.

4.1 Data Link Simulator Design

4.1.1 MATLAB Configuration

All transmitter/receiver blocks described in Figure 3.4 & Figure 3.10 with channel models and RF impairments are implemented modularly in MATLAB. Only for channel encoder/decoder, MATLAB's communication toolbox is used. The rest is implemented without using any specific functions of MATLAB. Figure 4.1 shows the functions generated in the simulator.

On MATLAB, the simulator is implemented based on object-oriented architecture. We wrote the classes for physical layer (*PHY*) and simulator (*SIM*). *PHY* includes all

configuration parameters of the data link like modulation type, OFDM pilot index, number of antennas etc. Likewise, all simulation parameters including channel configuration parameters are included in *SIM* class. All functions shown in Figure 4.1 runs with the objects constructed from *PHY* and *SIM* classes. A general simulation process block diagram is given in Figure 4.2.

4.1.2 RF Impairments

In our simulator, we account for some RF impairment to see the performance of data link testbed algorithms. These can be entitled as

- Residual RF impairments
- Phase noise
- Frequency offset
- Fractional time delay
- DC offset.

Transmitter and receiver devices suffer from a number of impairments which degrade the performance of communication. Although some of them can be compensated with some algorithms, there are still some residual parts remaining unaccounted for. These impairments can dramatically affect the performance of MIMO communication [54]. In the simulator, these residual parts are modeled for transmitter and receiver separately. The system model with residual impairments can be written as,

$$y = h * (s + n_{tx}) + n_{th} + n_{rx} \quad (4.1)$$

where n_{tx} is the noise term representing the sum of all transmitter residual RF impairments as i.i.d. Gaussian noise, n_{rx} is the receiver side of the residual RF impairments term which is also Gaussian and n_{th} is the thermal noise.

In the literature EVM (Error Vector Magnitude) is used to describe residual RF impairments. It can be written for a transmitter as

$$\text{EVM}_{tx} = \frac{E[|n_{tx}|^2]}{E[|s|^2]}, \quad (4.2)$$

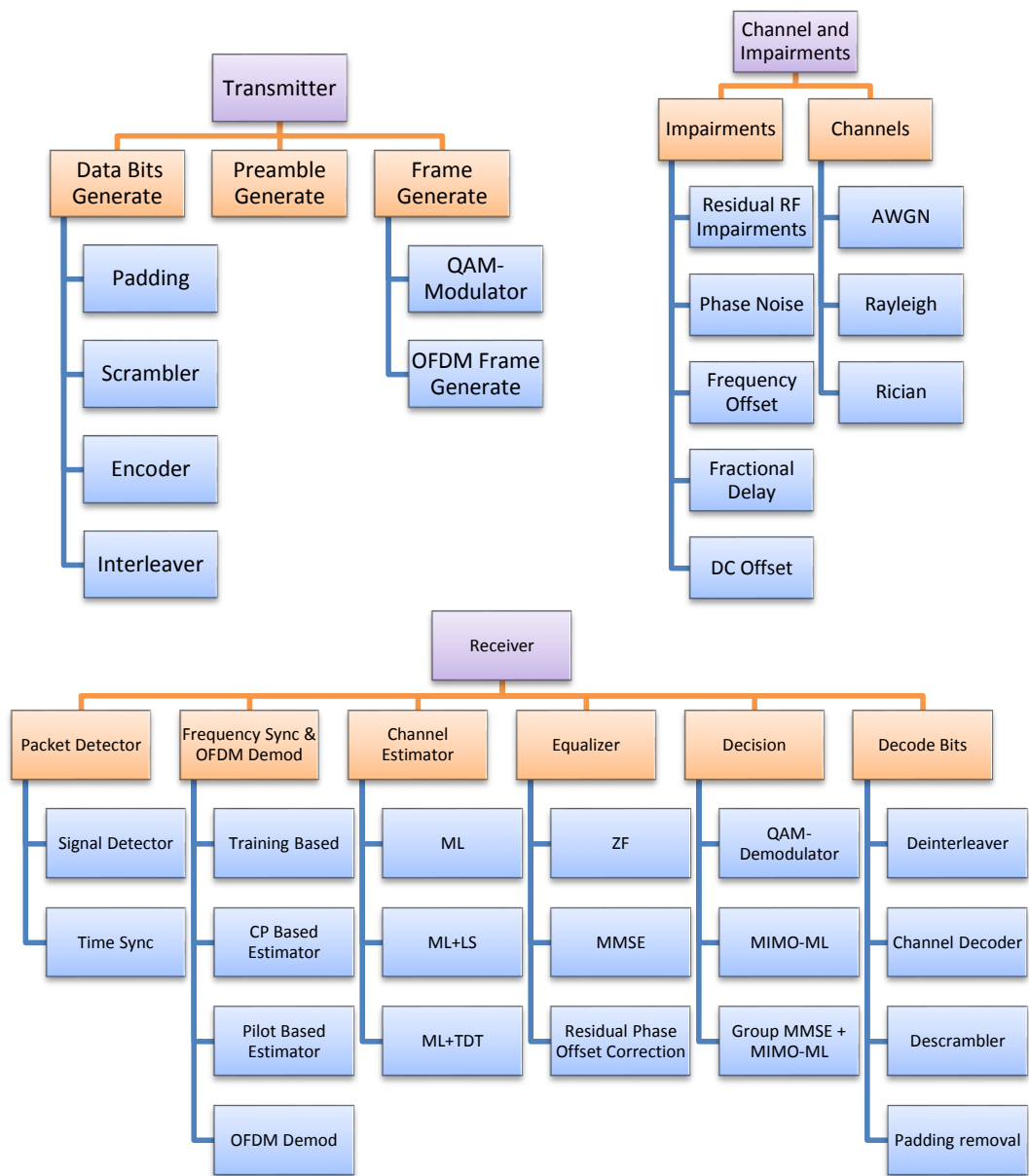


Figure 4.1: Data Link Simulator Software Functions Hierarchy

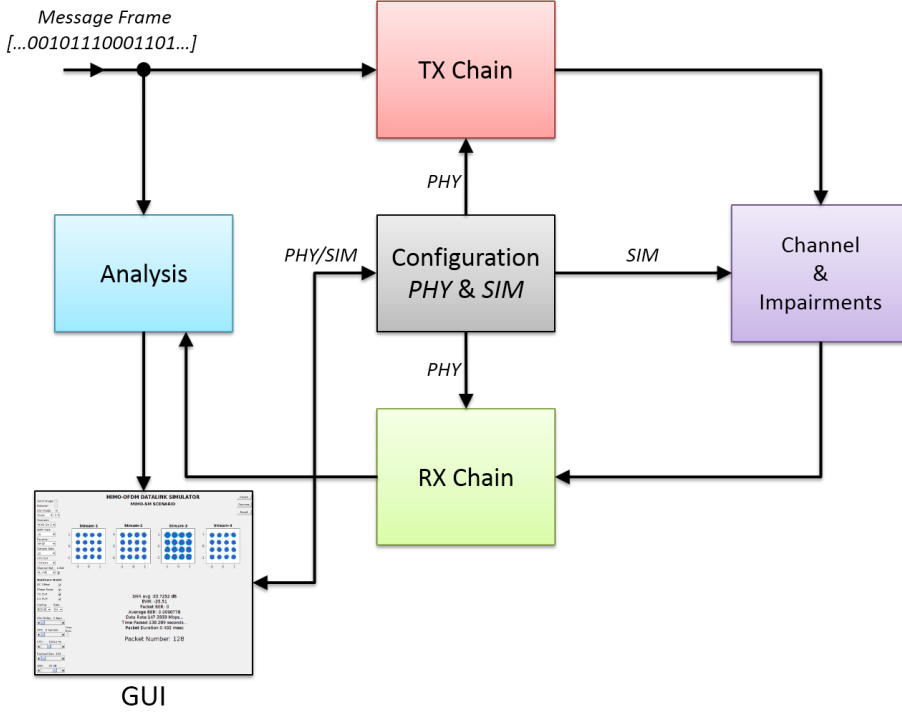


Figure 4.2: Data Link Simulator Process Diagram

similarly for receiver:

$$\text{EVM}_{rx} = \frac{E[|n_{rx}|^2]}{E[|s_{ref}^1|^2]} . \quad (4.3)$$

In the simulator, residual RF impairments are inserted to the signal according to EVM parameters setting.

In addition to residual RF impairments, phase noise is another RF problem that affects the communication performance and must therefore be modeled in the simulation environment. For this purpose, phase noise filter is generated [55]. Figure 4.3 shows the block diagram of the phase noise model function. It simply takes the input signal samples and multiplies with the generated Gaussian noise according to frequency offset and phase noise level values which determines the phase noise model. An example of tone signal under the effect of phase noise model generated in our simulator is plotted on Figure 4.4.

¹ s_{ref} is given as the reference signal. When measuring EVM on the receiver side, error signal power is divided by reference signal power. During this process, signal generator transmits the signal almost perfectly meaning that $s_{ref} \approx s$ and also thermal noise is kept on negligible level. So, EVM_{rx} equation is shown with s_{ref} term. In the simulator, $s_{ref} = s$ is taken and variance of n_{rx} term is found from EVM_{rx} value.

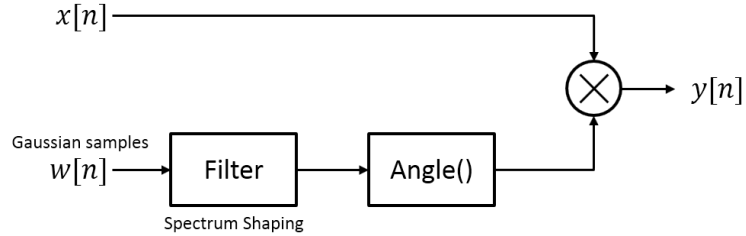


Figure 4.3: Phase Noise Model block diagram

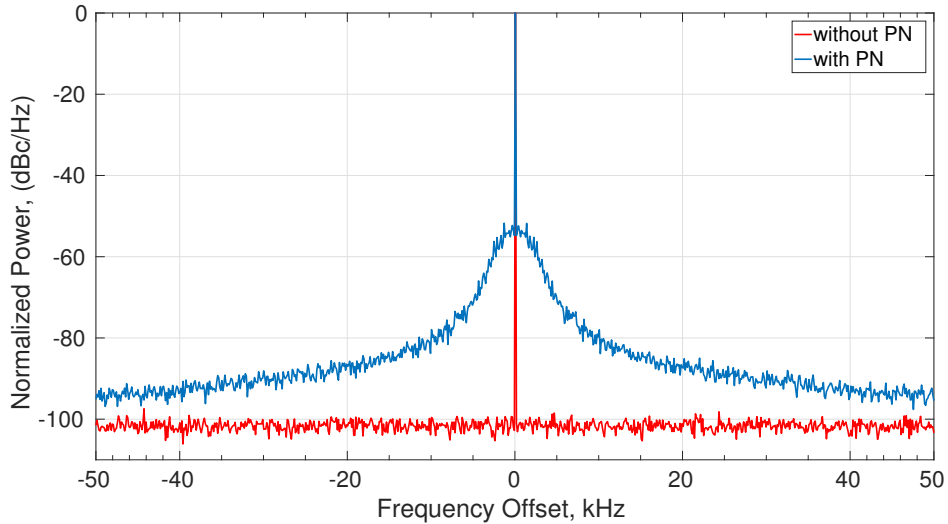


Figure 4.4: The spectrum of tone signal under the effect of phase noise model

Frequency offset term caused by non-ideal oscillators and Doppler frequency shifts is modeled by simply multiplying the received signal by $e^{j2\pi\epsilon/N}$ where ϵ is the normalized frequency offset value described in Section 3.4.3.

Another RF impairment model is the fractional time delay function. Since sampling clock frequencies of DAC and ADC are not coherent for transmitter and receiver respectively, there will always be some fractional delays if they work with equal sampling frequencies. The function runs with incoming samples by linearly interpolating them and then applying delay according to fractional input value. Lastly, samples are decimated to get the same sampling rate at output.

The last RF impairment model is DC offset which is one of the common problems in communication systems. Generally, it may be caused by leakage of the local oscillators as well as by the offset of the baseband signal in analog domain. Actually, it is encountered on both transmitter and receiver side. But, we assumed that the DC offset

produced in receiver side can be blocked by high pass filters and we only add DC term to transmitted signal. In our simulations, it is seen that in the existence of CFO, transmitter side DC offset will be in the form of tone signal whose frequency is CFO value and affects all the subcarriers of OFDM symbol when frequency synchronization is not good.

4.1.3 Channel Models

To see the performance of our testbed, we add channel models for LOS (Line-of-sight) and NLOS (None-line-of-sight) conditions. In our simulator, provided channels are AWGN, Rayleigh, and Rician.

AWGN channel model generates zero mean complex i.i.d. Gaussian samples according to input SNR value and summed with the transmitted signal. For testing algorithms and debugging purposes, AWGN channel model is extended to use with MIMO scenario. In that case, the channel is taken as identity matrix and noise is added to each stream separately as in

$$w_i \in \mathbf{w} \quad i = 1, 2, \dots, M \quad (4.4)$$

$$\mathbf{w} \sim \mathcal{CN}(0, \mathbf{I}\sigma_w^2) \quad (4.5)$$

$$\mathbf{y} = \mathbf{Hs} + \mathbf{w} . \quad (4.6)$$

Additionally, Rayleigh and Rician fading models are implemented as multi-tap channel filters. In Rayleigh channel model, the coefficients are chosen as,

$$h_{ij}[n] \in \mathbf{H}_{MXM}[n] \quad n = 0, 1, \dots, L - 1 \quad (4.7)$$

$$h_{ij} \sim \mathcal{CN}(0, 1) \quad i, j = 1, 2, \dots, M \quad (4.8)$$

where L is the channel length based on maximum delay spread and h_{ij} 's are zero mean normal distributed complex Gaussian samples. So, this model is reasonable when the channel is formed by independent scatterers and there is no line-of-sight path between transmitter and receiver. To simulate a channel where line-of-sight path exists and scatters are also available, Rician model is used. In this case, the coeffici-

ents are

$$h_{ij}[n] \in \mathbf{H}_{MXM}[n] \quad n = 0, 1, \dots, L - 1 , \quad (4.9)$$

$$h_{ij}[n] = \sqrt{\frac{\kappa}{\kappa + 1}} \sigma_n e^{j\theta_i} + \sqrt{\frac{1}{\kappa + 1}} \mathcal{CN}(0, \sigma_n^2) . \quad (4.10)$$

Here, κ is defined as the Rician fading factor, σ_n is the power of n^{th} channel tap and θ_i is the phase value of the line-of-sight path. In our simulator, for MIMO scenario, we assume that antennas are placed in linear geometry so that θ_i can be described as,

$$\theta_i = \frac{2\pi}{\lambda} d(i - 1) \cos(\phi_{tx}) \quad (4.11)$$

where λ is the wavelength, d is the inter-element (antenna) distance and θ_{tx} is the direction angle of the transmitter that is assumed to be uniformly distributed between 0 and 2π at each run in the simulator.

4.2 Data Link Simulator GUI

During simulation work, we implement GUI software in order to test the data link performance easily by changing various parameters without struggling on code script. Thanks to GUI, the user has a chance to analyze the testbed environment by setting with the following features.

- OFDM scenarios: SISO, 2×2 MIMO , 4×4 MIMO, 8×8 MIMO
- Channel model: AWGN, Rayleigh and Rician (by changing κ)
- Sampling rate: 5/10/20/30 MHz
- Modulation order: 4/16/64/256 QAM
- Equalizer: ZF and MMSE
- MIMO Detector: MIMO ML, Group MMSE + ML
- Frequency estimator: Training, CP and Pilot Based
- Channel estimator: ML, ML+LS and ML+TDT with CIR (Channel Impulse Response) Estimator check box

- Channel coder: HD and LLR Decoder with $1/2$, $2/3$, $3/4$ and $5/6$ coding rates
- Packet detector check box
- Payload length slider
- SNR slider
- Frequency offset slider
- Fractional delay slider with estimator check box
- Hardware RF Impairment model: EVM checkbox for RX/TX, phase noise, DC offset
- Channel delay spread slider
- Image sender check box
- GUI menu buttons: Pause, Resume and Reset

Therefore, all algorithms implemented for our data link testbed structure can be tested easily by selecting/setting desired modes/parameters on GUI. Also, it has the following visual outputs so that the user can observe the communication performance live.

- Constellation diagram
- Received image data
- Average/Packet BER
- Packet SNR (Average packet for MIMO)
- EVM
- Data rate
- Packet duration
- Simulation time

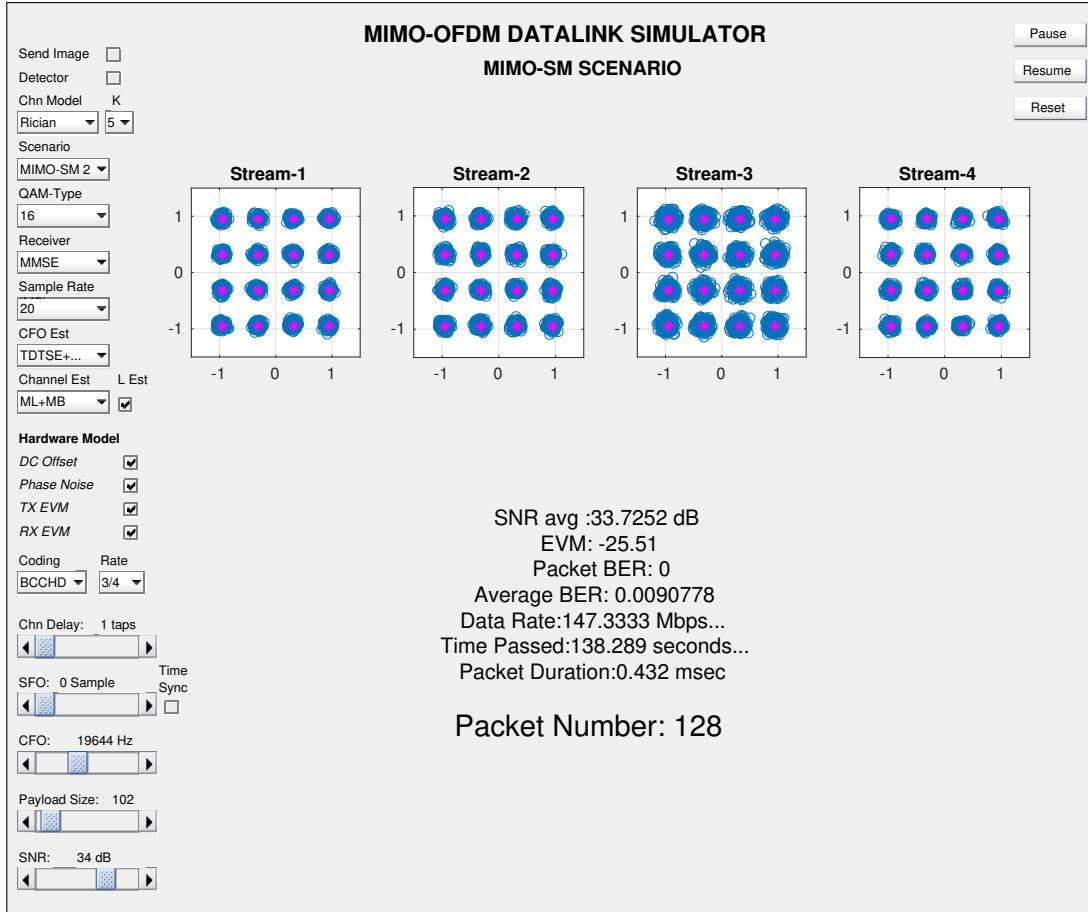


Figure 4.5: Data Link Simulator GUI software snapshot

Figure 4.5 shows a snapshot from the data link simulator GUI window. As seen, 16-QAM 4×4 MIMO-OFDM scenario runs in the simulator. Constellation diagrams are shown for each stream after equalization is performed. The signal bandwidth is set to 20 MHz. MMSE type equalizer is used with training + pilot based frequency estimators. For the channel estimator, ML+LS algorithm is selected. In the coding side, binary convolutional code is used with 3/4 coding rate and the decoder is using hard decision binary estimates. The channel is one-tap Rician with $\kappa = 5$ and SNR = 34 dB. Also, some of impairments are activated. Frequency offset is set to approximately 19.6 kHz and hardware models for DC Offset², Phase Noise³ and TX/RX EVMs⁴ are checked. In addition, 128 packet communication is performed in total and some of analysis parameters are printed on GUI window.

²DC offset is modeled as -60 dBc.

³Phase noise filter is generated at frequency offsets of 0.1, 1 MHz with corresponding -90 , -110 dBc noise levels respectively.

⁴EVM values are taken as -36 dB for both TX and RX sides.

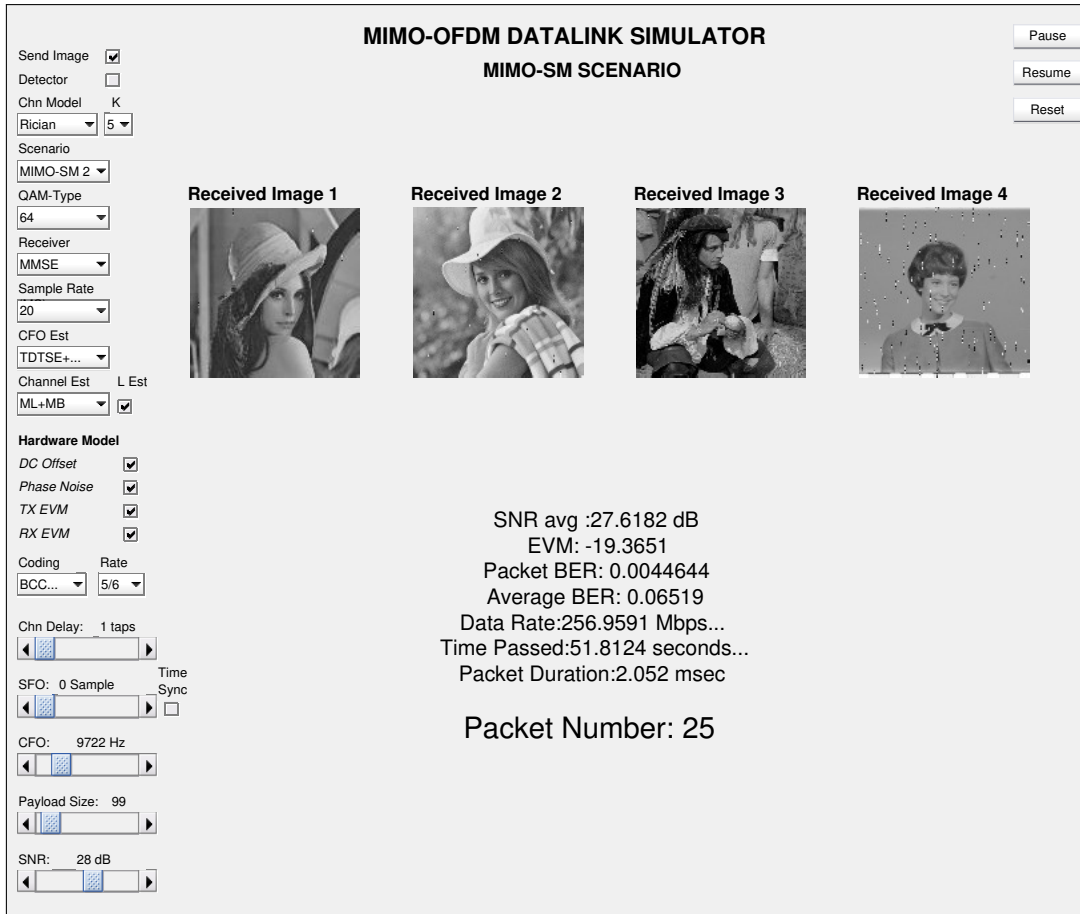


Figure 4.6: Data Link Simulator GUI software snapshot (Image sender is active)

Another snapshot from the GUI is shown in Figure 4.6. This time, *Image Sender* is activated. Normally, simulator generates uniformly distributed binary sequence as data. In this mode, image data is transformed to serial bit stream and used as data bits. As seen from the figure, some bits are estimated wrongly because of low SNR (28 dB) regime with higher order modulation (64-QAM) so that distortions occur on some part of the images.

4.3 Simulation Results

Monte Carlo simulations are performed in different use cases of our testbed. For the performance criteria, BER metrics are calculated and plotted against E_b/N_0 . In our simulator, noise is added to the signal according to SNR value. Therefore, the relation

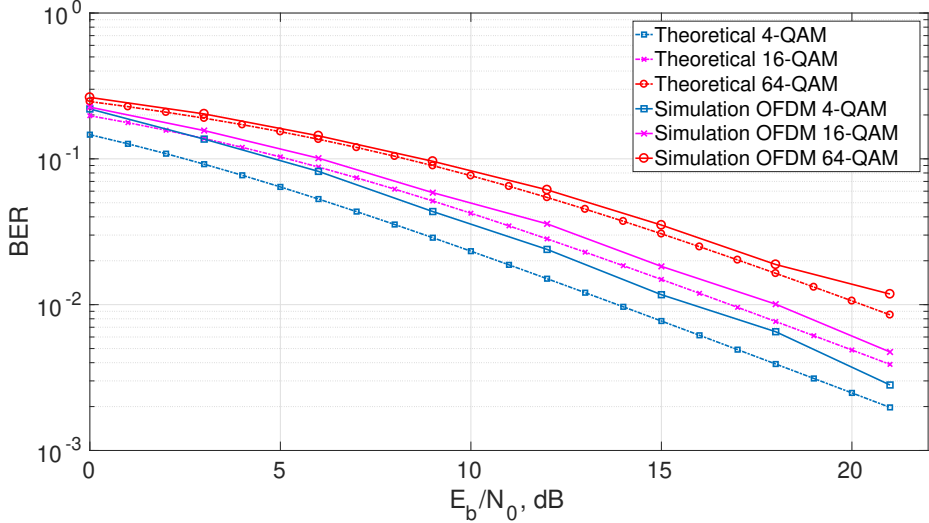


Figure 4.7: Simulation results for the BER performance of our data link in different modulation orders under Rayleigh channel model

between E_b/N_0 and SNR can be written as,

$$\frac{E_b}{N_0} = \text{SNR} \times \frac{N}{N_{DSC}} \times \frac{1}{N_{SS}} \times \frac{1}{R_{BCC}} \times \frac{1}{\log_2(M)} \quad (4.12)$$

where N is the FFT length, N_{DSC} is the number of data subcarriers, N_{SS} is the number of spatial streams, R_{BCC} is the code rate, and M is the modulation order.

In Figure 4.7, uncoded BER performance of our data link is presented in different modulation orders for SISO scenario. Additionally, theoretical BER results are added for comparison. In the simulator, the channel is set to one tap (flat fading) Rayleigh distribution and some RF impairment models are activated⁵. Frequency offset is set to 25 kHz for 20 MHz signal bandwidth. On the receiver side, training based coarse estimator is used with pilot based algorithm for frequency synchronization. For the channel estimation, ML+LS algorithm is run. Equalization and decision are performed with MMSE and single-stream ML⁶ respectively. As can be seen from the figure, 4-QAM outperforms higher order modulations when E_b/N_0 increases as expected. But one interesting thing to observe that 4-QAM differs from others in comparison with its theoretical performance. It is almost 2 dB worse than theoretical BER curve. This is due to the fact that frequency synchronization is done using BPSK modulated pilots and from the relation between E_b/N_0 and SNR, we know that for the same E_b/N_0 values, as the modulation order increases, SNR also increases. Then, synchronization performance is better at higher SNR value so that the difference will be less at higher

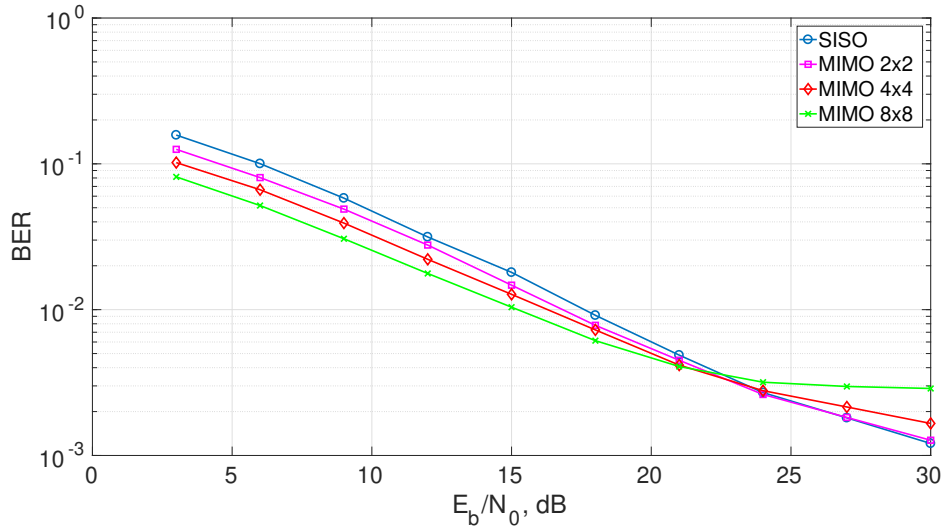


Figure 4.8: Simulation results for the performance of MIMO spatial multiplexing scenarios under flat fading Rayleigh channel model

order modulation schemes.

The performance of MIMO spatial multiplexing scenarios are given in Figure 4.8 along with SISO scenario. The same configuration is used with this simulation and modulation type is set to 16-QAM. The plot shows that MIMO with higher number of antennas used has better performance at low E_b/N_0 values. However, as for higher E_b/N_0 , after all scenarios almost equal BER results at $E_b/N_0 = 24$ dB, performance curves for MIMO scenarios starts flattening due to RF impairments (especially phase noise and residual impairments). Therefore, SISO scenario outperforms others as being less affected from those impairments because of having lower SNR value at the same E_b/N_0 , that is, RF impairments still do not dominate.

We also simulate the performance of MIMO scenarios under frequency selective channel conditions in Figure 4.9. The channel is set to Rayleigh with 3 taps. Modulation order is 16. It is observed that higher order MIMO scenarios yields better BER performance up to $E_b/N_0 = 21$ dB. Similar to previous simulation results, performance degradation occurs for higher E_b/N_0 values because of residual impairments and phase noise. As it is seen, the performance of 8×8 MIMO scenario is first effected due to having highest SNR at the same E_b/N_0 value compared to other scenarios.

⁵We used the same models for DC Offset, phase noise and EVM as in Figure 4.5

⁶ML detector is applied to each MIMO stream separately in single-stream ML.

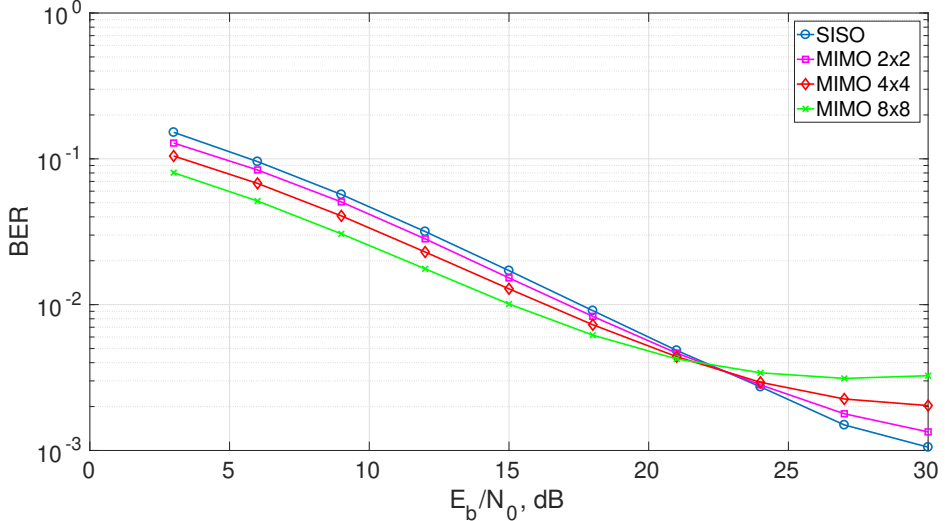


Figure 4.9: Performance of MIMO scenarios under frequency selective Rayleigh channel model

Because, similar to previous simulation, as SNR increases, RF impairments start dominating so that performance curves are flatten in order depending on the SNR values of each MIMO scenario.

Figure 4.10 shows BER analysis of MIMO scenarios under Rician channel where strong LOS path exists with $\kappa = 5$. Modulation order is set to 4. As seen, SISO scenario has the best performance on this channel model compared to MIMO. Since Rician model is used, the channel matrix \mathbf{H} is in poor condition including approximately correlated vectors $\mathbf{h}_i = [h_{i1}, h_{i2}, \dots, h_{iM}]^T$ where M is the number of transmit antennas.

In Figure 4.11, BER performance of different modulation orders are evaluated with channel coding at SISO scenario. BER values are calculated for 4/16/64 QAM modulation types with 1/2, 3/4 and 5/6 coding rates respectively. Decoder uses LLR outputs of the demodulator and flat fading Rician channel model is used with $\kappa = 9$. The plot shows that 4-QAM with coding rate 1/2 gives the best performance amongst others. Since the Rician channel runs with $\kappa = 9$, that is, the LOS path is very strong and the stochastic term is weak, we observe good performance results with channel coding.

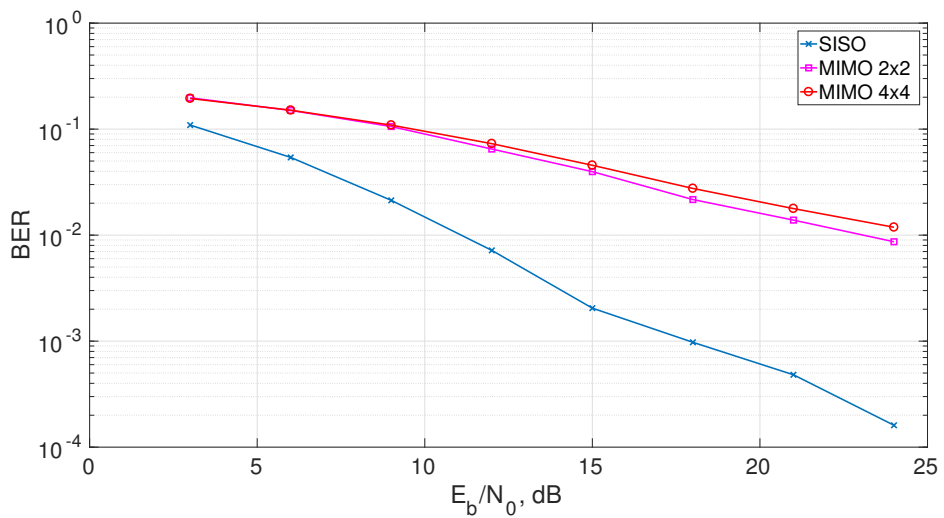


Figure 4.10: Performance of MIMO scenarios under flat fading Rician channel ($\kappa = 5$) model

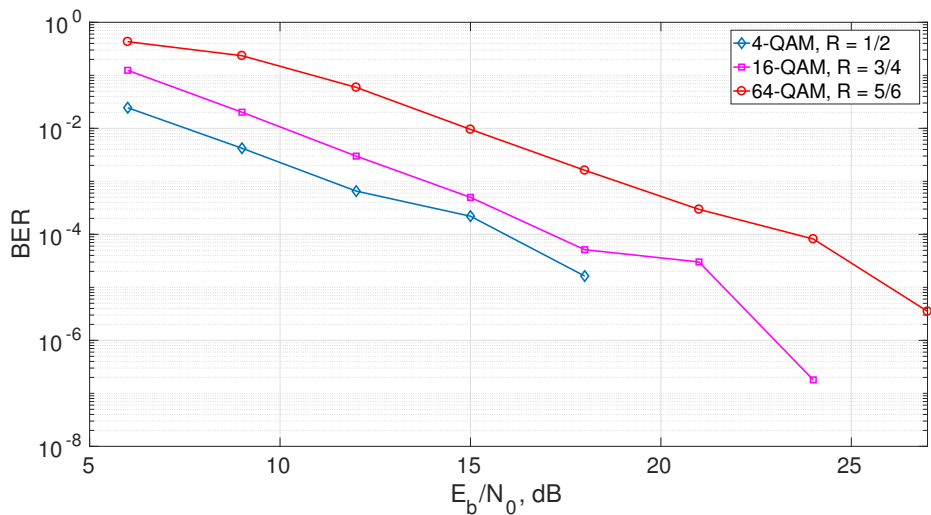


Figure 4.11: Performance of different modulation types with channel coding at SISO scenario under flat fading Rician channel ($\kappa = 9$)

In the previous simulations, diversity gains are not achieved in MIMO scenarios as it is seen. In Figure 4.12, BER performance of the coded MIMO scenarios are compared under flat fading Rayleigh channel for 4-QAM modulation type with 1/2 coding rate. Thanks to stream parsing with channel coding, diversity gain is achieved for transmitter side. In [56] [57] [58], the maximum transmit diversity gain is given as

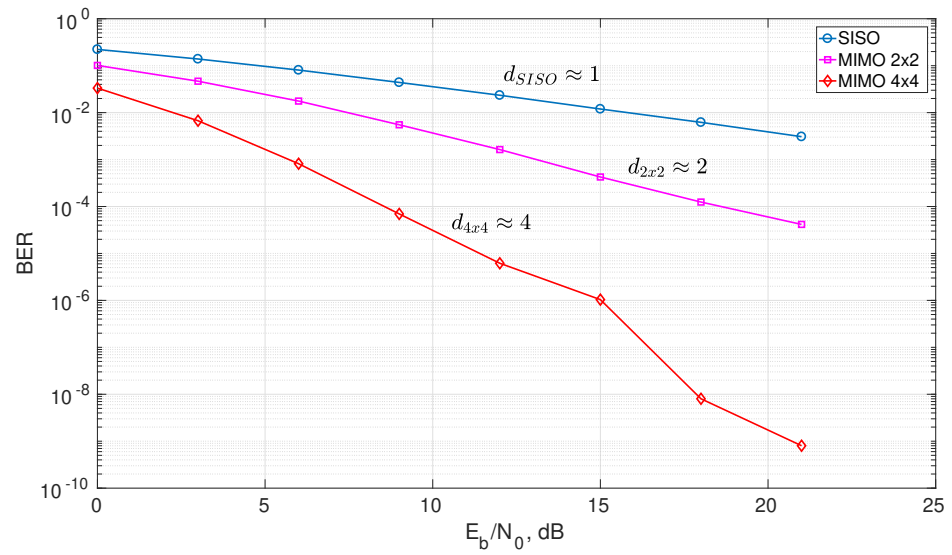
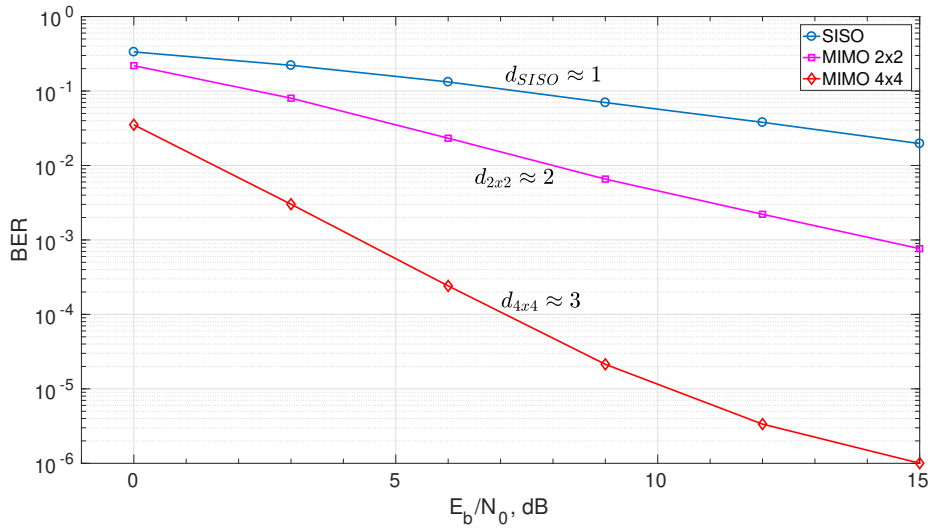
$$\nu = 1 + \lfloor Ln_t(1 - R) \rfloor \quad (4.13)$$

where L is the length of channel which is 1 for our case, n_t is the number of transmit antennas and R is the coding rate. It is observed that transmit diversity gains are approximately achieved with 1/2 coding rate for 2×2 and 4×4 MIMO scenarios.

Also, in Figure 4.13, same simulation is performed with uncoded bits. This time, detector is changed to MIMO-ML instead of single-stream ML. With MIMO-ML detector, diversity can be achieved at the receiver side which is coming directly from the number of antennas without using channel coding [56]. As seen, diversity gains are approximately obtained for 2×2 and 4×4 MIMO scenarios.

Depending on the results in Figure 4.12 and Figure 4.13, the maximum achievable diversity order for the MIMO-OFDM system is the product of transmit diversity gain ν which is coming by channel coding and receive diversity gain n_r obtained by MIMO-ML detector as the number of receive antennas. Therefore, as expressed in [56], we can write the maximum diversity gain for the MIMO-OFDM system as

$$d_{MIMO-OFDM} = (1 + \lfloor Ln_t(1 - R) \rfloor)n_r . \quad (4.14)$$



CHAPTER 5

TESTBED IMPLEMENTATION

In chapters 3 and 4, MIMO-OFDM data link algorithms, their implementation and analysis results on the simulation environment are given. In this chapter, we present how MIMO-OFDM data link testbed is implemented on SDR platform.

Nowadays, many studies have been carried out for the next and newest mobile wireless standard called 5G. Among the discussions on frequency deployments of 5G, 3.5 GHz is the starting point [17][59][60]. For this reason, we performed data link and channel analysis tests in the frequency of 3.5 GHz.

In our testbed, we test SISO and MIMO 2×2 scenarios by using USRP B210 [16] from Ettus Research company, an SDR device, which is able to transmit/receive from both channels coherently. GNU Radio is used for communicating with USRPs for setting its RF and digital parameters, signal transmission and acquisition purposes. Signal generation and demodulation process is performed on MATLAB by using the data link simulator environment. In the following sections, we will explain the testbed setup in detail.

5.1 Testbed Setup

Testbed setup diagram is described in Figure 5.1. On the computer, baseband OFDM signal is generated by MATLAB environment using the simulator and recorded to binary files. Then, GNU Radio is used to send generated signal to USRP for transmitting at desired frequency. On the other side, USRP down converts the RF signal to

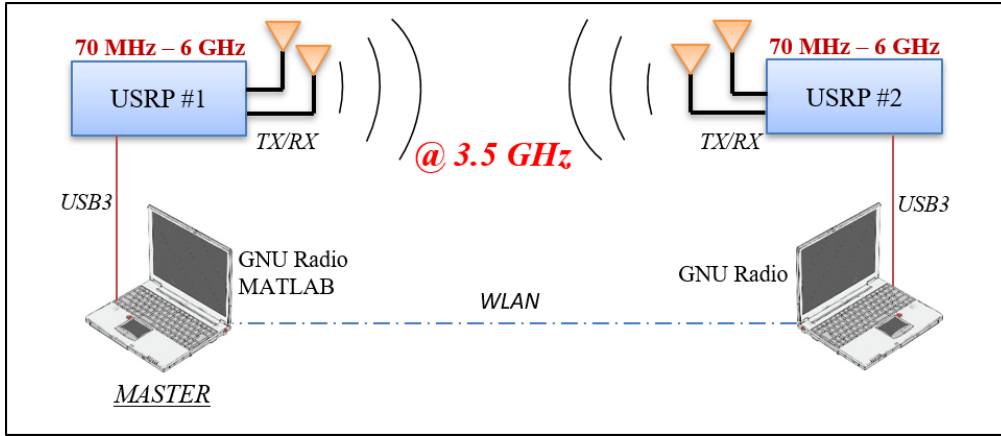


Figure 5.1: Testbed Setup Diagram

the baseband and send it to the computer for being recorded to specific file via GNU Radio. Postprocessing is performed with the simulator in MATLAB.

One computer in the testbed acts as master; that is, the entire control is provided by the master computer. Both computers are in the same WLAN network so that master can control the other one easily using the SSH protocol.

5.2 USRP B210

Universal Software Radio Peripheral (USRP) is a family of SDRs produced and sold by a company called Ettus Research. In this study, we used the USRP B210 model. It provides a fully integrated single board environment covering frequencies from 70 MHz up to 6 GHz. The B210 is designed with ADI's direct conversion transceiver AD9361 [61] which is able to stream up to 56 MHz of real time RF bandwidth including both signal chains with coherent MIMO capability. The device includes Spartan6 XC6SLX150 FPGA [62], responsible for controlling AD9361 and onboard signal processing operations. It is connected to host PC with fast speed USB3 interface. Thanks to USRP Hardware Driver (UHD), users start developing their applications directly without writing custom drivers. It is a cross-platform driver that can run on Linux, Windows, and MacOS. UHD comes with a common API which is fully supported by the GNU Radio software framework. The general block diagram of the B210 is shown in Figure 5.2. Additionally, Table 5.1 gives the specifications of the device.

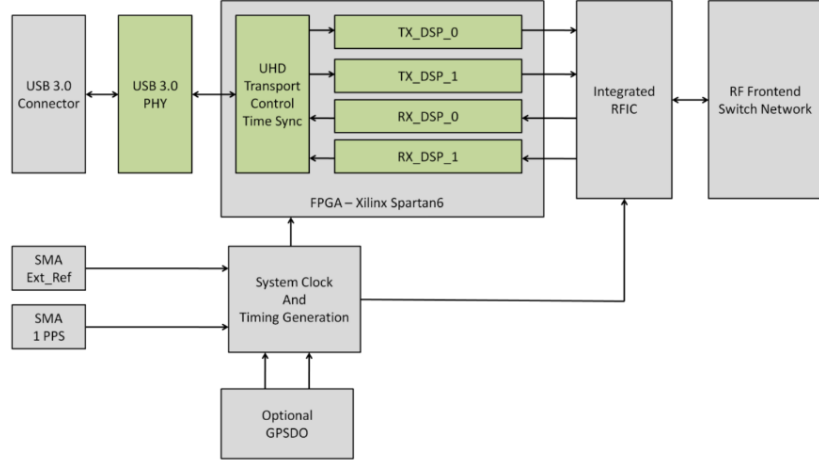


Figure 5.2: The general block diagram of the USRP B210 board [16]

5.3 3.5 GHz Antennas

Specific antennas working at 3.5 GHz frequency band were used for this thesis study. With the advantages of light weight and easy fabrication, linearly polarized rectangular microstrip patch antennas were chosen as antenna type. The work in [63], was used as reference for the antennas. Figure 5.3, depicts the 3D gain pattern of microstrip patch antenna whose resonance frequency is 3.5 GHz. From the simulation results, we see that the maximum achievable gain is 5.12 dBi in z direction. Also, 3

Table 5.1: Specifications of USRP B210 Board

Spec	Type	Unit
Frequency	70 - 6000	MHz
ADC Sample Rate (max)	61.44	MS/s
ADC/DAC Resolution	12	bits
SFDR	78	dBc
Host Sample Rate (16bits)	61.44	MS/s
Frequency Accuracy	± 2	ppm
With GPS Unlocked	± 75	ppb
With GPS Locked	<1	ppb
Phase Noise @3.5 GHz	1	deg RMS
Output Power	>10	dBm
RX Noise Figure	<8	dB
Dimensions	9.7x15.5x1.5	cm
Weight	350	g

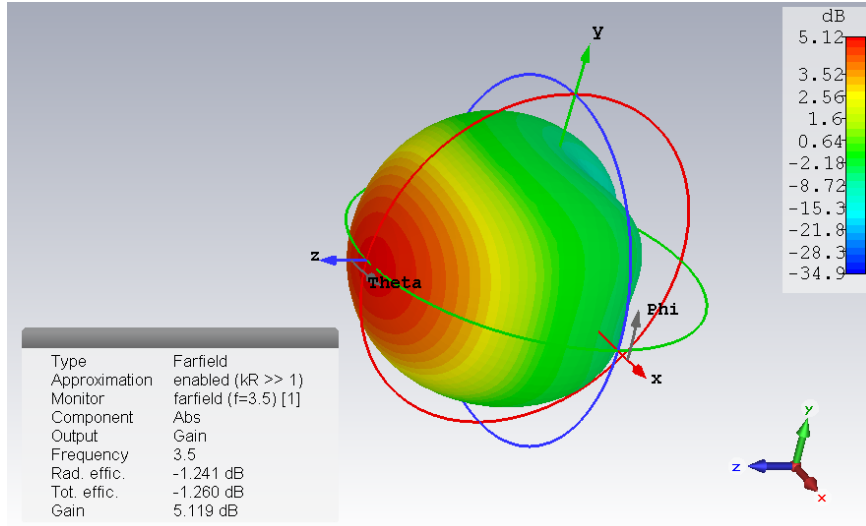


Figure 5.3: 3D Gain radiation pattern of 3.5 GHz rectangular microstrip patch antenna

dB beamwidth is approximately 95° for elevation, 83° for azimuth angles. This high beamwidth values allow high scattering environment even in LOS case which serves well for MIMO applications.

All design and implementation work was carried out by the company Anketek [64]. Four antennas (for using in 2×2 MIMO) were manufactured by using PCB prototyping machine. As for the antenna substrate, Rogers 4003 [65] was preferred. Figure 5.4 shows the manufactured antennas. As seen on the image, the feed point of the antennas are on the edge of the substrate and L shaped SMA connectors are used to connect the antennas to the USRPs.

After manufacturing, we also measured S11 of the antennas at their operating frequency band. Fieldfox N9918A combination analyzer was used to make measurements in VNA (Vector Network Analyzer) mode. S11 curves are shown in Figure 5.5. All four antennas give similar performance. However, they suffer from narrow bandwidth which is approximately 40 MHz¹. This is a general major drawback of the microstrip antennas due to high quality factor. Since the bandwidth of our data link system is limited to 20 MHz, the antennas with narrow bandwidth will not affect our testbed study.

¹It refers to the range of frequencies over which the antenna has -10 dB or lower S11 value.

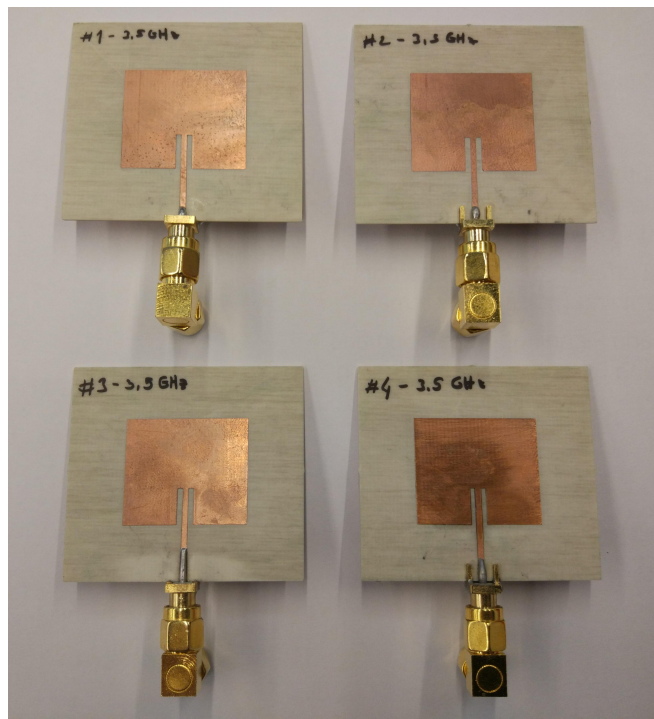


Figure 5.4: Manufactured microstrip patch antennas (Female type SMA Connector is soldered to the feeding point and connected to the B210 with L type Male-Male SMA connector)

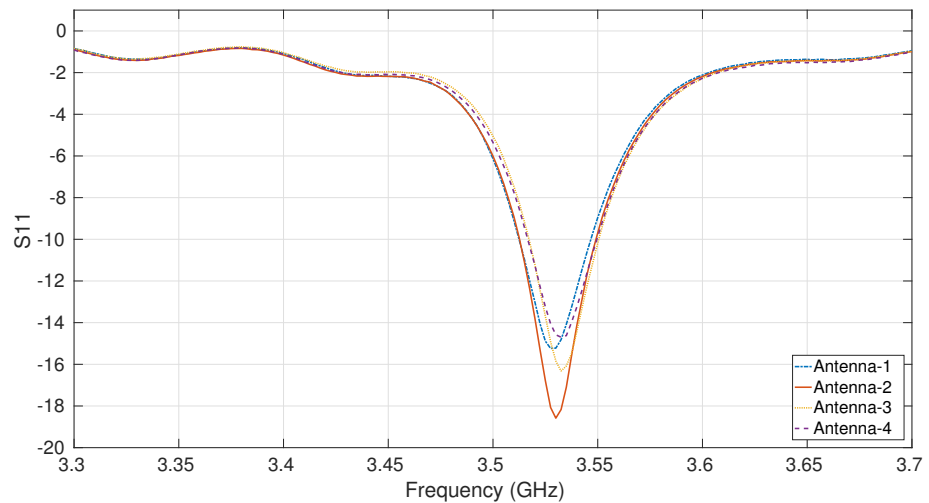


Figure 5.5: Measured S₁₁ values of the manufactured microstrip patch antennas

5.4 Signal Transmission/Acquisition with GNU Radio

GNU Radio is a software framework that the user can design and create flow-graphs including radio signal processing applications. In this study, we used GNU Radio for signal transmission and acquisition purposes. As known, all baseband processing is performed on MATLAB. Hence, in our testbed, the baseband MIMO-OFDM signal which is saved to a binary file is transmitted by the B210 hardware via GNU Radio. And then, the other B210 hardware which is also controlled by GNU Radio takes the RF signal transmitted, down converts to the baseband and records it for post processing on MATLAB.

GNU Radio infrastructure is written totally in C++. However, the flow-graphs can be written in C++ and Python (version 2) programming language. In our testbed, we wrote different flow-graphs in Python for controlling and data transfer operations. These are:

- **Transmitter flow-graph:** Includes SISO and MIMO signal transmission and controlling the B210 hardware,
- **Receiver flow-graph:** Includes SISO and MIMO signal acquisition for static and dynamic measurement scenarios and controlling the B210 hardware.

5.4.1 Transmitter Flow-graph

Transmitter flow-graph is responsible for:

- Reading the binary SISO/MIMO baseband signal file and send the I&Q samples to the B210 hardware,
- Configuring the B210 (Sampling rate, TX Gain, carrier frequency).

The binary file is read by using *file_source* class from GNU Radio library[29]. For configuring the B210 as a transmitter, *usrp_sink* class of UHD API is used[29]. The python script takes command-line arguments as TX gain, carrier frequency, sampling rate, and file type. Figure 5.6 shows how the script runs in the Unix command-line.

```

ufuk->>python mimo_tx.py --h
linux; GNU C++ version 6.3.0 20170406; Boost_104200; UHD_003.010.002.000-3-g122bfae1
usage: mimo_tx.py [-h] [-tx TX] [-fs FS] [-fc FC] [-mod MOD]
MIMO TX Test Code, it takes 3 arguments. 1st TX Gain, 2nd Sample Rate, 3rd fc
optional arguments:
-h, --help show this help message and exit
-tx TX TX Gain in the range [0,89] (dB)
-fs FS Sample Rate in MHz
-fc FC Carrier Frequency in MHz
-mod MOD Modulation Order, e.g. 16
ufuk->>python mimo_tx.py -tx 60 -fs 10 -fc 3500 -mod 4
linux; GNU C++ version 6.3.0 20170406; Boost_106200; UHD_003.010.002.000-3-g122bfae1
-- Detected Device: B210
-- Operating over USB 3.
-- Initialize CODEC control...
-- Initialize Radio control...
-- Performing register loopback test... pass
-- Performing register loopback test... pass
-- Performing CODEC loopback test... pass
-- Performing CODEC loopback test... pass
-- Setting master clock rate selection to 'automatic'.
-- Asking for clock rate 16.000000 MHz...
-- Actually got clock rate 16.000000 MHz.
-- Performing timer loopback test... pass
-- Performing timer loopback test... pass
-- Setting master clock rate selection to 'manual'.
-- Asking for clock rate 12.000000 MHz...
-- Actually got clock rate 12.000000 MHz.
-- Performing timer loopback test... pass
-- Performing timer loopback test... pass
-- 1) catch time transition at pps edge
-- 2) set times next pps (synchronously)
-- Asking for clock rate 10.000000 MHz...
-- Actually got clock rate 10.000000 MHz.
-- Performing timer loopback test... pass
-- Performing timer loopback test... pass
TX Gain: 60
Sample Rate: 10 MSps
Clock Rate: 10 MHz
Carrier Frequency: 3500 MHz
Tx Data Files:
/home/ufuk/Thesis/tx_works/txData/28-May-2018_MIMO_OFDM_TX_unfilt_4-QAM_CHN_1_#1.dat
/home/ufuk/Thesis/tx_works/txData/28-May-2018_MIMO_OFDM_TX_unfilt_4-QAM_CHN_2_#1.dat
Press Enter to start]
ufuk

```

Figure 5.6: Transmitter Flow-graph python script usage

After the user runs the script with proper values of arguments and press the *Enter* button, the B210 starts transmitting the baseband signal continuously in accordance with the arguments entered until pressing the *Enter* button again.

5.4.2 Receiver Flow-graph

Receiver flow-graph is responsible for:

- Configuring the B210 (Sampling rate, RX Gain, carrier frequency)
- Writing the baseband SISO/MIMO I&Q samples to the binary file/s.

To configure the B210 as a receiver, *usrp_source* class of UHD API is used. Moreover, I&Q samples are written to a binary file by using the *file_sink* class from GNU Radio library. The user writes the input parameters together with python script file name into the command-line. The parameters are RX Gain, sampling rate, carrier fre-

```

ufuk>>python mimo_rx.py --h
linux; GNU C++ version 6.3.0 20170406; Boost_106200; UHD_003.010.002.000-3-g122bfae1
usage: mimo_rx.py [-h] [-rx RX] [-fs FS] [-fc FC] [-nsamp NSAMP]
                  [-nfile NFILE] [-mod MOD]
MIMO RX Test Code, it takes 6 arguments. 1st TX Gain, 2nd Sample Rate, 3rd fc,
4th Num of Recorded Samples, 5th Data File ID, 6th Modulation Order
optional arguments:
  -h, --help    show this help message and exit
  -rx RX        RX Gain in the range [0,89] (dB), e.g 43
  -fs FS        Sample Rate in MHz, e.g 12
  -fc FC        Carrier Frequency in MHz, e.g 2450
  -nsamp NSAMP  Number of Recorded Samples in MS, e.g 2
  -nfile NFILE  Recorded Data File ID, e.g 3
  -mod MOD     Modulation Order, e.g 16
ufuk>>python mimo_rx.py -rx 50 -fs 3500 -nsamp 2 -nfile 1 -mod 4
linux; GNU C++ version 6.3.0 20170406; Boost_106200; UHD_003.010.002.000-3-g122bfae1
-- Detected Device: B210
-- Operating over USB 3.
-- Initialize CODEC control...
-- Initialize Radio control...
-- Performing register loopback test... pass
-- Performing register loopback test... pass
-- Performing CODEC loopback test... pass
-- Performing CODEC loopback test... pass
-- Setting master clock rate selection to 'automatic'.
-- Asking for clock rate 16.000000 MHz...
-- Actually got clock rate 16.000000 MHz.
-- Performing timer loopback test... pass
-- Performing timer loopback test... pass
-- Asking for clock rate 48.000000 MHz...
-- Actually got clock rate 48.000000 MHz.
-- Performing timer loopback test... pass
-- Performing timer loopback test... pass
-- 1) catch time transition at pps edge
-- 2) set timer next pps (synchronously)
-- Setting master clock rate selection to 'manual'.
-- Asking for clock rate 10.000000 MHz...
-- Actually got clock rate 10.000000 MHz.
-- Performing timer loopback test... pass
-- Performing timer loopback test... pass
RX Gain: 50
Sample Rate: 10 MSps
Clock Rate: 10 MHz
Carrier Frequency: 3500 MHz
Number of Recorded Samples: 2 MS

Files Created:
/home/ufuk/Theesis/rx_works/rxData/04-06-2018_MIMO_OFDM_RX_4-QAM_CHN_1_#1.dat
/home/ufuk/Theesis/rx_works/rxData/04-06-2018_MIMO_OFDM_RX_4-QAM_CHN_2_#1.dat
Press Enter to start]

```

The code runs with arguments

User can see the configuration parameters

Binary files recorded

Figure 5.7: Receiver Flow-graph python script usage

quency, record length, file ID, and modulation type. Figure 5.6 shows how the script runs in the Unix command-line. Once the user runs the script properly and press the *Enter* button, the B210 starts recording baseband signal samples with the user defined configuration.

CHAPTER 6

TESTBED WORK

This chapter presents our testbed study. With our testbed, we did data link tests for the implemented MIMO-OFDM physical layer and channel analysis for indoor/outdoor environments at static and dynamic channel conditions. We used two laptops connected to the B210s via USB3 and one of them controls the testbed platform. The antennas were connected to the TX/RX¹ ports of the B210 with the distance of $0.7\lambda_c$ between them. For all test cases, the carrier frequency is set to 3530 MHz where the antennas yield best S11 performance. Figure 6.1, shows the testbed setup platform for one side (TX or RX).

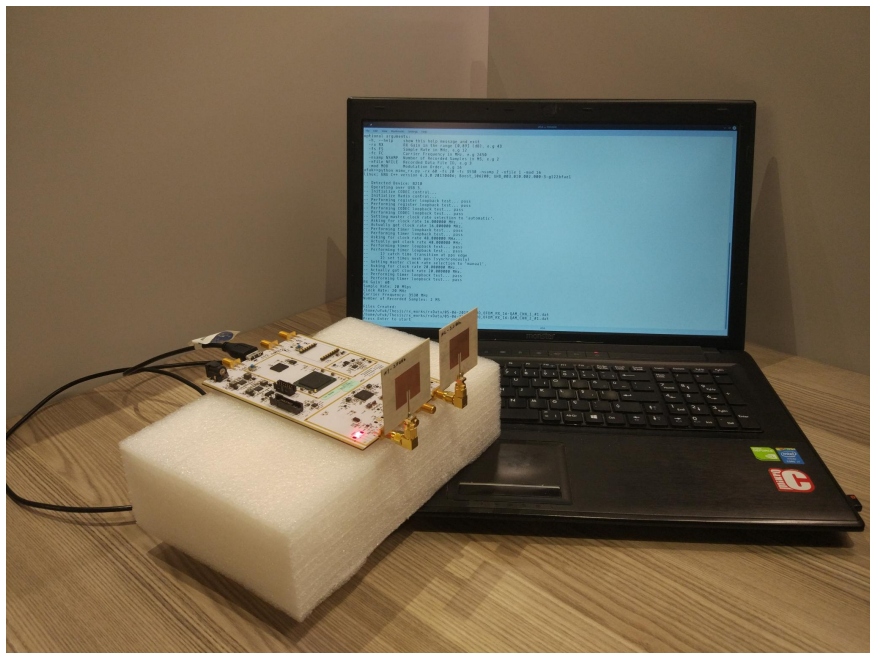


Figure 6.1: The testbed setup platform for one side

¹TX/RX port can be used as both transmitter and receiver by programming the B210.



Figure 6.2: An example of the indoor data link testbed scenarios

6.1 Data Link Tests on SDR Platform

For the data link tests, we set up our testbed in the indoor and outdoor environments where the channel is generally NLOS. We ran the python scripts for SISO and 2×2 MIMO scenarios. In order to analyze the test after each run in MATLAB, we implemented a testbed data link GUI software by using our MIMO-OFDM simulator. From this GUI, user can choose some of the algorithms implemented for our MIMO-OFDM receiver to see the performance of the data link under chosen structure.

In Figure 6.2, an example of the indoor data link testbed scenarios is shown. As seen, the test was carried out in an office room where there are a lot of obstacles between radios that creates NLOS condition. A snapshot from the data link testbed GUI that shows the analysis results of the indoor scenario (Figure 6.2) tests is given in Figure 6.3. As it is seen, 16-QAM 2×2 MIMO-OFDM testbed data link scenario is run on the GUI software. The user can change equalizers and channel/frequency estimators, also activate fractional time synchronization and CIR estimator algorithms. The recorded data file name is also shown at the bottom of the GUI window. As for the results of 2×2 MIMO data link test in this indoor scenario, calculated EVM values from equalized symbols are very close to the measured average SNR showing that we

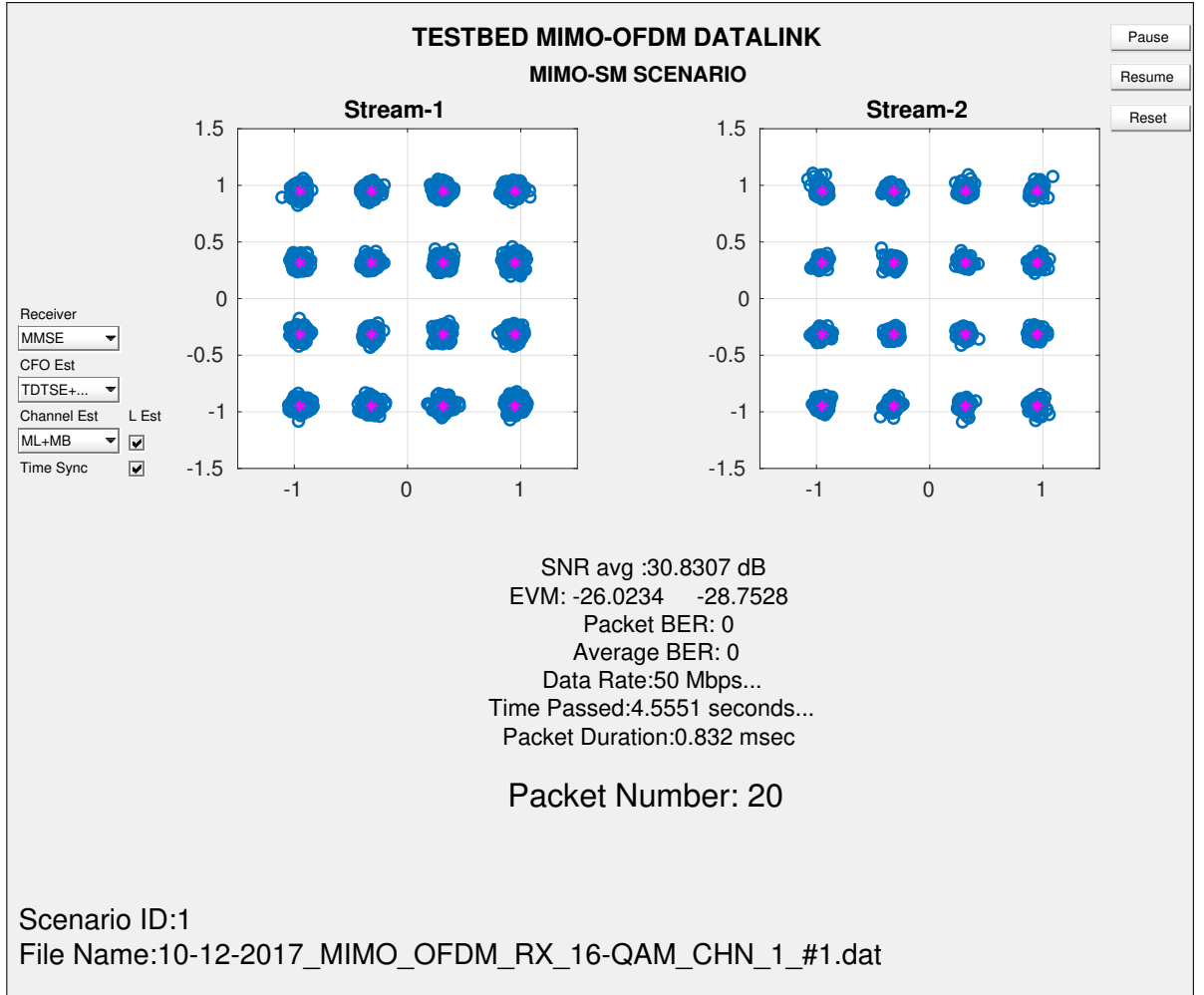


Figure 6.3: A snapshot from the data link testbed GUI running 16-QAM 2×2 MIMO-OFDM scenario

observe a good MIMO channel environment in this office room with an NLOS placement of radios. The bandwidth of the signal is set to 10 MHz and achieved data rate from this data link approaches 50 Mbps with approximately 800 μ sec packet duration. The best EVM performance is obtained with the configuration shown in Table 6.1.

Similarly, we deployed our testbed platform in various environments including indoor and outdoor. According to the placement of radios, we set proper TX PA (Power Amplifier) and RX LNA (Low Noise Amplifier) gain parameters. Also, the tests were performed in different bandwidth options such as 5, 10 and 20 MHz and in different modulation orders, e.g., 4/16/64 QAM. In order to manage and control all measurements, we made a configuration file including all measurement scenarios with its parameters and descriptions. With this file, we can have all the information related with

Table6.1: MIMO-OFDM Data Link Testbed Configuration

Parameter	Configuration
Fractional Time sync.	Enabled
Coarse frequency sync. (dB)	Training based estimator
Fine frequency sync. (dB)	Pilot based estimator
Channel Estimation	ML+LS
Equalizer	MMSE

Order	Data No #	Date	Mode	BW (MHz)	TX Gain	RX Gain	Mod	Channel	Chn. State	Notes	Tx Data No: #	Photo Link
13	8	12/12/2017	MIMO	10	67	65	4	Indoor	5	object.put btw radios, snr 28, evm -26	3	link 13
57	4	03/06/2018	MIMO	5	85	65	64	Outdoor	1	better with fs=5, snr 24, evm -23	2	link 57
68	1	05/06/2018	SISO	20	85	70	16	Indoor	1	snr 30, evm -26	5	link 68
78	1	09/06/2018	MIMO	20	85	70	16	Indoor	1	snr 25, evm 13, LOS channel	5	link 78
79	3	09/06/2018	MIMO	20	89	70	64	Outdoor	2	snr 33, evm 23-26	7	link 79
85	5	10/06/2018	SISO	20	80	70	4	Outdoor	1	snr 19, evm 17	7	link 85

Figure 6.4: Testbed configuration file

that specific measurement. A part of the configuration file is shown in Figure 6.4. As it is seen, in each row, we registered the RX/TX data ID, date, communication mode, bandwidth, TX/RX gain, modulation order, channel environment, channel state, description and testbed photo link for each specific measurement. For example, when we perform a data link test in an environment, a photo is taken to show how the channel looks like. In order to run our data link analysis GUI, RX data ID, measurement date and communication mode parameters are used to play corresponding recorded binary data of that specific measurement. For BER and EVM analysis operations, TX Data ID is used. Other parameters, such as bandwidth, TX/RX Gain, channel and channel state², are registered for detailed analysis of our testbed data link.

6.2 2×2 MIMO Channel Analysis

This section presents the channel analysis work for indoor and outdoor environments. As known, performance of MIMO communication depends on the correlation between channel coefficients. In other words, MIMO is favorable when differences occur in the propagation conditions between TX-RX antenna pairs. To understand the

²Channel state indicates different positioning of radios in the same environment. We use this notation to differentiate and identify each measurement case for fair comparison.

relation between MIMO channel and capacity, let us consider 2×2 MIMO model:

$$\underbrace{\begin{bmatrix} y_1 \\ y_2 \end{bmatrix}}_{\mathbf{y}} = \underbrace{\begin{bmatrix} h_{11} & h_{12} \\ h_{21} & h_{22} \end{bmatrix}}_{\mathbf{H}} \underbrace{\begin{bmatrix} x_1 \\ x_2 \end{bmatrix}}_{\mathbf{x}} + \underbrace{\begin{bmatrix} n_1 \\ n_2 \end{bmatrix}}_{\mathbf{n}} . \quad (6.1)$$

Under the constraint of $\text{tr}(\mathbf{HH}^H)$, the capacity is maximum when the channel vectors are independent. This condition holds if \mathbf{H} is diagonal ($\mathbf{H}=\mathbf{D}$), that is,

$$\underbrace{\begin{bmatrix} y_1 \\ y_2 \end{bmatrix}}_{\mathbf{y}} = \underbrace{\begin{bmatrix} h_{11} & 0 \\ 0 & h_{22} \end{bmatrix}}_{\mathbf{D}} \underbrace{\begin{bmatrix} x_1 \\ x_2 \end{bmatrix}}_{\mathbf{x}} + \underbrace{\begin{bmatrix} n_1 \\ n_2 \end{bmatrix}}_{\mathbf{n}} , \quad (6.2)$$

$$y_i = h_{ii}x_i + n_i , \quad i = 1, 2 . \quad (6.3)$$

In practice, the probability that such conditions occur is small in general ³. Then, what we can do is to diagonalize the matrix \mathbf{H} by applying precoding and postcoding operations at transmitter and receiver respectively [22]. This is obtained by adding precoding \mathbf{W}_t and postcoding \mathbf{W}_r matrices to the matrix \mathbf{H} , such that

$$\mathbf{D} = \mathbf{W}_r \mathbf{H} \mathbf{W}_t . \quad (6.4)$$

\mathbf{W}_t and \mathbf{W}_r are computed by performing singular value decomposition (SVD) of \mathbf{H} . Then, with SVD operation, channel matrix \mathbf{H} can be represented as

$$\mathbf{H} = \mathbf{U} \mathbf{D} \mathbf{V}^H \quad (6.5)$$

where \mathbf{D} is a diagonal matrix whose diagonal terms are also the square roots of the eigenvalues of \mathbf{HH}^H and \mathbf{U} and \mathbf{V} are unitary orthonormal matrices, such that

$$\mathbf{U} \mathbf{U}^H = \mathbf{I} , \quad \mathbf{V} \mathbf{V}^H = \mathbf{I} . \quad (6.6)$$

Additionally, the columns of \mathbf{U} are orthonormal eigenvectors of \mathbf{HH}^H and similarly the columns of \mathbf{V} are orthonormal eigenvectors of $\mathbf{H}^H \mathbf{H}$. Hence, from (6.6), \mathbf{W}_t and \mathbf{W}_r are computed as

$$\mathbf{W}_r = \mathbf{U}^H \quad \text{and} \quad \mathbf{W}_t = \mathbf{V} . \quad (6.7)$$

Then we have,

$$\mathbf{y} = \mathbf{W}_r \mathbf{H} \mathbf{W}_t = \mathbf{D} \mathbf{x} + \tilde{\mathbf{n}} , \quad (6.8)$$

$$y_i = \sqrt{\lambda_i} x_i + \tilde{n}_i , \quad i = 1, 2 . \quad (6.9)$$

³For 2×2 MIMO case, if different polarized antennas are used (e.g. one is vertical, the other is horizontal), then the channel is more similar to diagonal. Since the cross-polarization gains will be much small e.g. -20 dB.

where $\tilde{\mathbf{n}}$ is zero-mean, Gaussian, with i.i.d. noise vector and $E[\tilde{\mathbf{n}}\tilde{\mathbf{n}}^H] = \mathbf{I}$.

To complete the discussion of MIMO capacity, we write the capacity for SISO system as

$$C_{SISO} = \log_2(1 + |h|^2\rho) \quad (6.10)$$

where h is the complex channel gain and ρ is the average signal to noise ratio of the system, such that $\rho = \frac{E[|x|^2]}{E[|n|^2]}$. Assuming that there is no channel information at transmitter (power is uniformly allocated), for the MIMO scenario with N_t transmit and N_r receive antennas ($N_r \times N_t$), the capacity is [22]

$$C_{MIMO} = \sum_{i=1}^M \log_2\left(1 + \frac{\rho}{N_t}\lambda_i\right), \quad M = \min(N_r, N_t). \quad (6.11)$$

In order to show how eigenvalues of channel matrix \mathbf{H} affects performance of MIMO system, let us consider three different scenarios for 2×2 MIMO case. In the first scenario, consider that we have LOS channel and \mathbf{H} is found to be as

$$\mathbf{H} = \begin{bmatrix} 0.5 & 0.5 \\ 0.5 & 0.5 \end{bmatrix} \quad (6.12)$$

and eigenvalues (λ_i) of $\mathbf{H}\mathbf{H}^H$ are 1 and 0. For the second case, we assume that there are very small differences between antenna pairs, such that

$$\mathbf{H} = \begin{bmatrix} 0.51 & 0.49 \\ 0.47 & 0.52 \end{bmatrix} \quad (6.13)$$

and we have $\lambda_1 = 0.9903$ and $\lambda_2 = 0.0012$. Lastly, when we have significant differences between antenna pairs, for example,

$$\mathbf{H} = \begin{bmatrix} 0.65 & -j0.3 \\ j0.35 & -0.6 \end{bmatrix}, \quad (6.14)$$

then the eigenvalues are $\lambda_1 = 0.5473$ and $\lambda_2 = 0.4477$ which corresponds to the NLOS condition. As a consequence, having evaluated all three cases:

- When there is a LOS condition, MIMO has no advantage and all the power is transmitted through one antenna (λ_1).
- We start taking advantage of the MIMO system, while the channel gains are differentiated.

Based on the conclusions above, we did some experiments at indoor and outdoor environments by using our testbed data link. For all tests, the bandwidth of the signal is set to 20 MHz and modulation order is 4. On the receiver side, frequency synchronization is performed with training and pilot based estimators and channel is estimated with ML+LS algorithm. The capacity of the channel is computed with equation 6.11. Without loss of generality $E[|x|^2] = 1$ is taken and eigenvalues of $\mathbf{H}\mathbf{H}^H$ is found by $\hat{\mathbf{H}}_{ML+LS}$. In order to evaluate the characteristics of the channel, we also implemented a testbed channel analysis GUI software. This GUI shows detailed channel estimation results with capacity plot for all subcarriers of MIMO-OFDM system. Additionally, we registered all the measurements to our configuration file for channel analysis study as we already used in our data link tests.

6.2.1 Indoor Channel Analysis

Indoor channel analysis tests were carried out in an office room. We placed the radios where the channel is at LOS and NLOS conditions. Figure 6.5 shows the LOS and NLOS scenarios of our testbed. For each scenario, SISO, 2×2 MIMO data links were run with testbed channel analysis GUI. Also, dynamic measurements were taken for showing the capacity change in time when there are small movements⁴ of one of the radios in our testbed.

A snapshot from the testbed channel analysis GUI is given in Figure 6.6 for an NLOS condition test. As can be seen from the figure, channel coefficients are plotted in both frequency and time domains. From the estimated channel matrix, eigenvalues of $\hat{\mathbf{H}}\hat{\mathbf{H}}^H$ and the corresponding channel capacity results are shown for each subcarrier. Additionally, MMSE equalized symbols are plotted on the constellation diagram for each stream.

In this NLOS condition test, we observe that the channel matrix is well-conditioned, that is, both eigenvalues are strong which makes the condition number⁵ small. Compared to the SNR value, computed EVMs are almost 5-6 dB smaller and the average

⁴In the dynamic measurement scenario, one of the radios are moved to the all directions in the order of wavelength of the operated carrier frequency which is 3530 MHz.

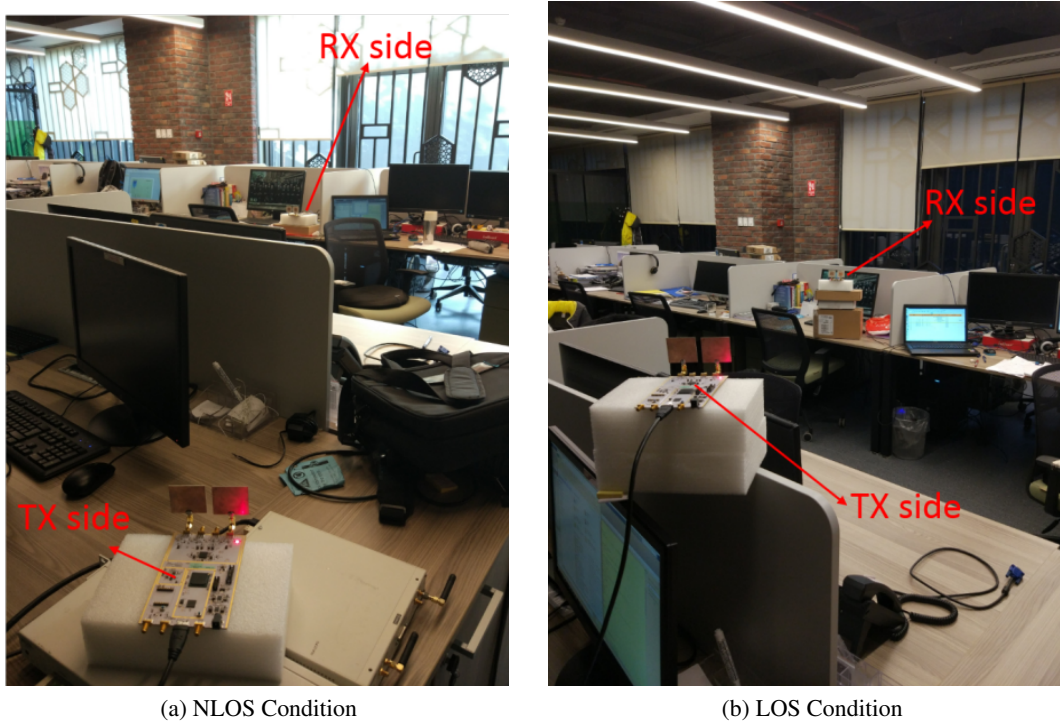


Figure 6.5: Indoor Channel Analysis Scenarios

capacity of all subcarriers is approximately 16 b/s/Hz .

In Figure 6.7, a similar snapshot from the testbed channel analysis GUI is given for LOS condition test. It is observed that the channel matrix is ill-conditioned meaning that only one eigenvalue is strong. Since the channel is ill-conditioned, noise enhancement problem degrades the performance of detection even with MMSE equalizer. Also, compared to the NLOS scenario, EVM values are almost 20 dB bigger at the similar SNR value and the average capacity is almost 5 b/s/Hz smaller.

In the NLOS condition, we also ran static and dynamic channel measurements. For dynamic case, we tested the effect of changing the position of radios in the order of wavelength to the channel capacity in SISO and MIMO (2×2) configurations. One of the radios (RX side is used for this test) was moved by approximately 10 cm in all directions continuously during the test. However, static measurements were carried out without moving the radios at all. Also, all measurements were performed with a

⁵Condition number (κ) of normal matrices (e.g. $\mathbf{H}\mathbf{H}^H$) can be computed as the ratio of the largest eigenvalue to the smallest eigenvalue such that $\kappa(\mathbf{A}) = \frac{\lambda_{\max}(\mathbf{A})}{\lambda_{\min}(\mathbf{A})}$. Large condition number indicates that the matrix is almost singular.

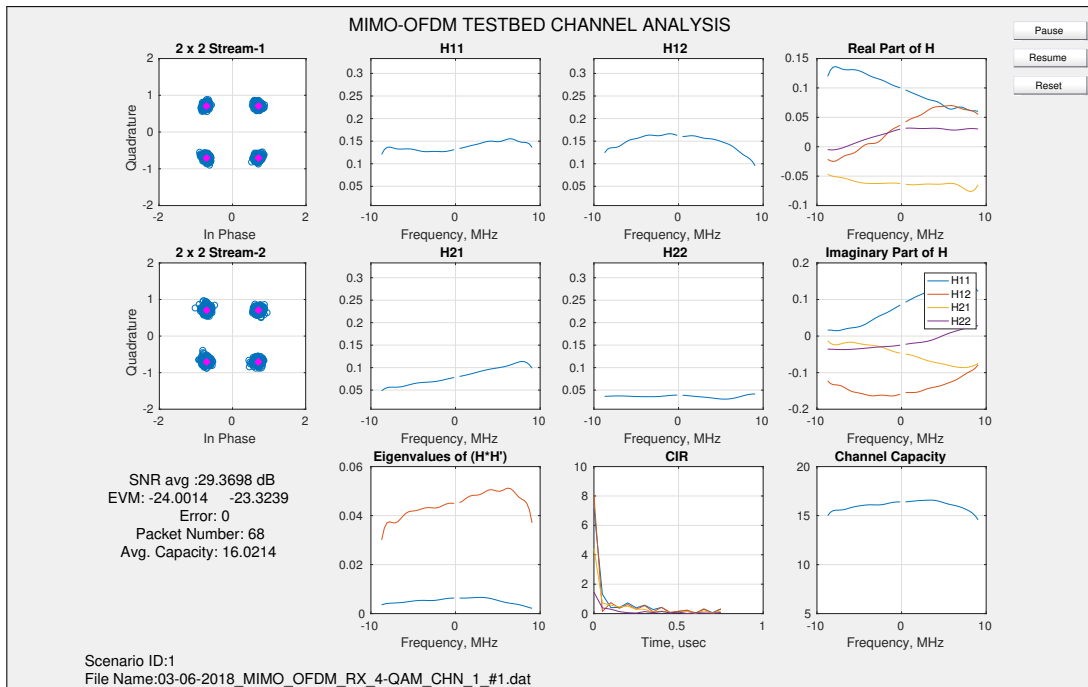


Figure 6.6: A snapshot from the testbed channel analysis GUI running 4-QAM 2×2 MIMO-OFDM indoor NLOS scenario.

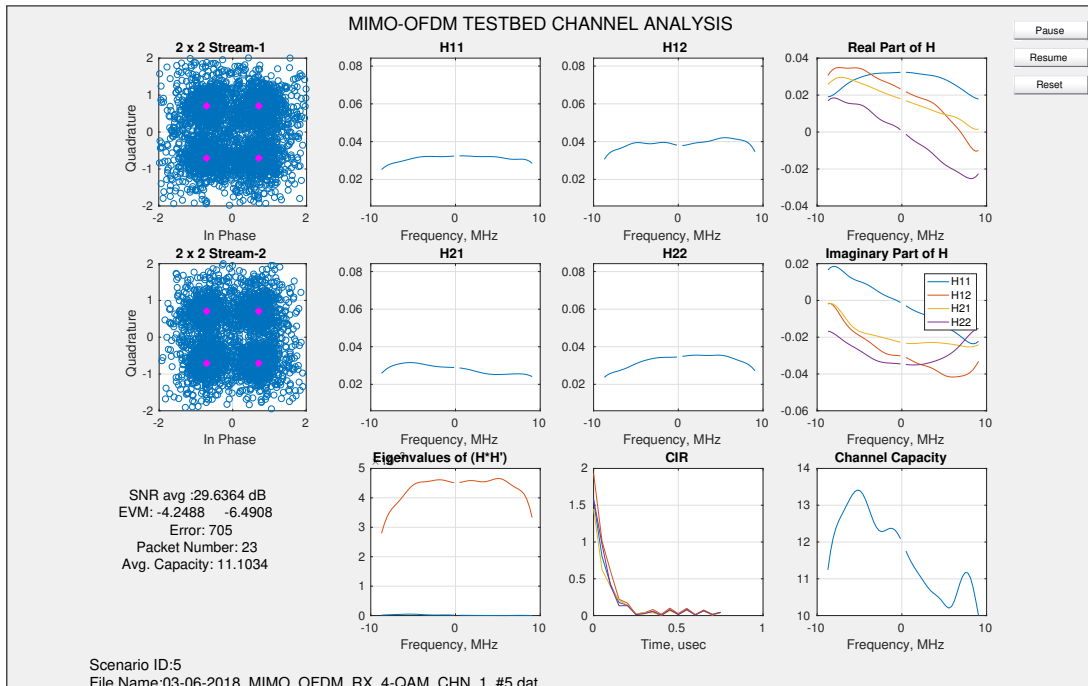


Figure 6.7: A snapshot from the testbed channel analysis GUI running 4-QAM 2×2 MIMO-OFDM indoor LOS scenario.

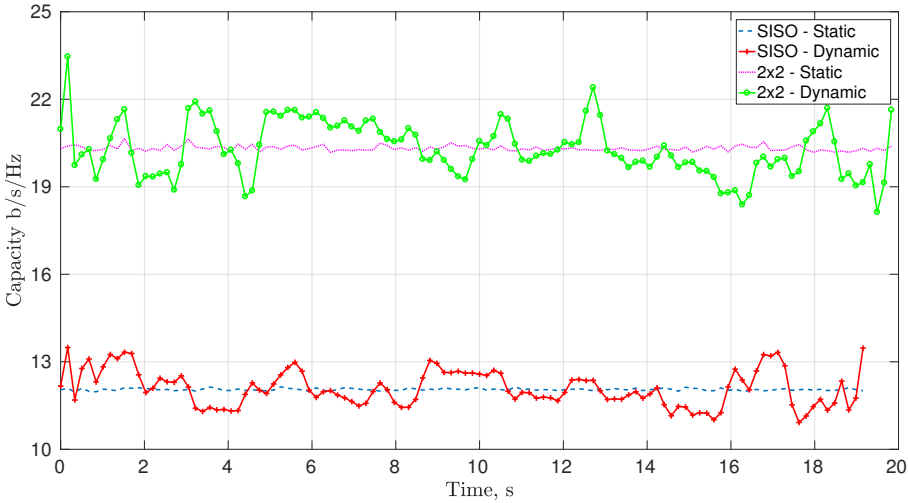


Figure 6.8: Indoor dynamic and static channel capacity performance in the NLOS condition

constant transmit power and we measured the average SNR for static cases as 36 dB. The results are shown in Figure 6.8. It is observed that the channel capacity of 2×2 MIMO is about 1.7 times that of the SISO system in the static case. For the dynamic case, the channel capacity is fluctuating around the case of static measurements. So, the average capacity change percentage (according to its mean) over time is about 5% for both MIMO and SISO. These results are expected since the changing the position of radio in the order of wavelength results with a different channel response (destructive or constructive gain for SISO and the channel matrix condition number (κ) for MIMO).

6.2.2 Outdoor Channel Analysis

For the outdoor tests, we performed channel analysis measurements in two different locations. The radios were placed at where there are objects between them resulting in a scattered environment. And also, LOS and NLOS conditions were created as we did in the indoor measurements. In these environments, SISO and 2×2 MIMO data links were run again with our testbed channel analysis GUI. For some scenarios, we took the measurements for dynamic and static cases which are similar to the indoor measurements. Additionally, measurements were taken when one of the radios was mobile following a predetermined trajectory.



Figure 6.9: Outdoor test environment #1

Figure 6.9 shows the first outdoor test environment. As it is seen, the radios were placed at where there are objects (e.g. windows, trees, stair rail) in between and with different altitudes. We took dynamic and static measurements in this configuration. For the dynamic case, the measurements were performed similar to that of the indoor scenario. In Figure 6.10, the measured channel capacities are plotted. We observe that the capacity in MIMO is about 1.7 times higher than SISO for static case. This result is the same with the indoor scenario. When we look at the dynamic case, it is seen that the values have higher variance around the mean value of static measurements for both SISO and MIMO scenarios. While the standard deviation of capacity values over time in MIMO scenario is 1.3 b/s/Hz , it is 0.6 b/s/Hz in SISO. Then, the average capacity change percentages are 10% for MIMO and 8% for SISO.

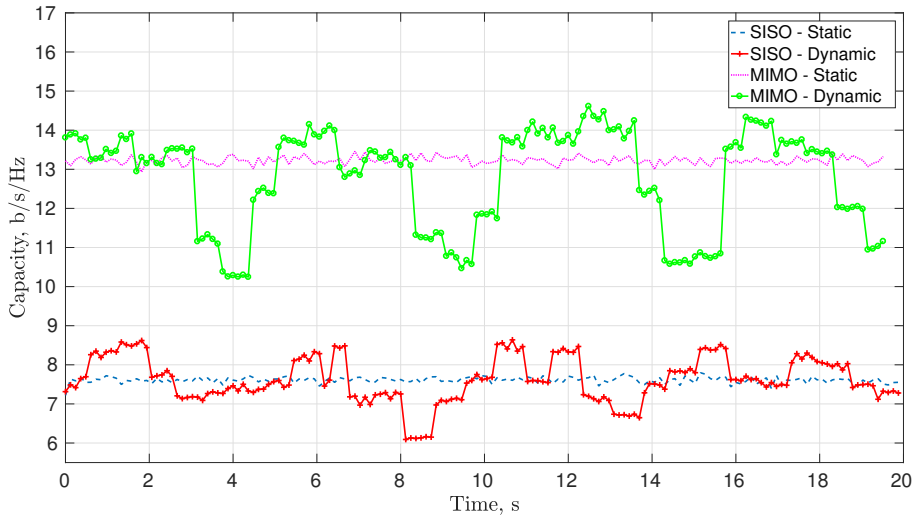


Figure 6.10: Dynamic and static channel capacity performance in the outdoor environment #1 (Average SNR is measured as 24 dB in static cases.)

We performed the same measurements in another environment which is shown with our test setup in Figure 6.11. It is seen that there are many objects (e.g. cars, trees, windows, etc.) causing scattered environment. As we did in the previous test, dynamic and static measurements were taken in this place too. For all configurations, the transmit power was kept constant. In static cases, the measured average SNR is 19 dB. The channel capacities of dynamic and static cases are given in Figure 6.12. As it is seen, the results are similar with the first outdoor environment. Since the average SNR is lower, corresponding channel capacities are also lower compared to the previous test. In addition, the standard deviation of capacity values in MIMO scenario is 1.5 b/s/Hz and it is 0.6 b/s/Hz in SISO. Corresponding capacity change percentages are 14% for MIMO and 11% for SISO.



Figure 6.11: Outdoor test environment #2

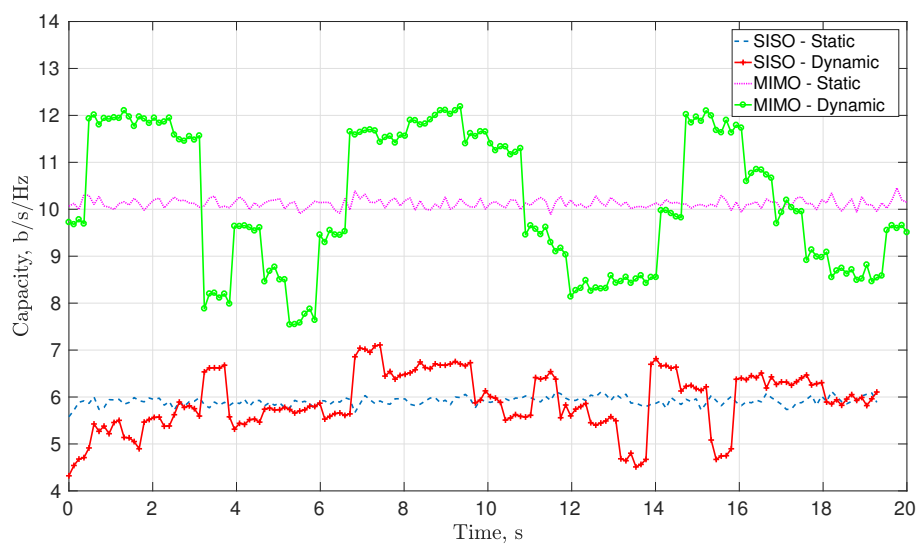
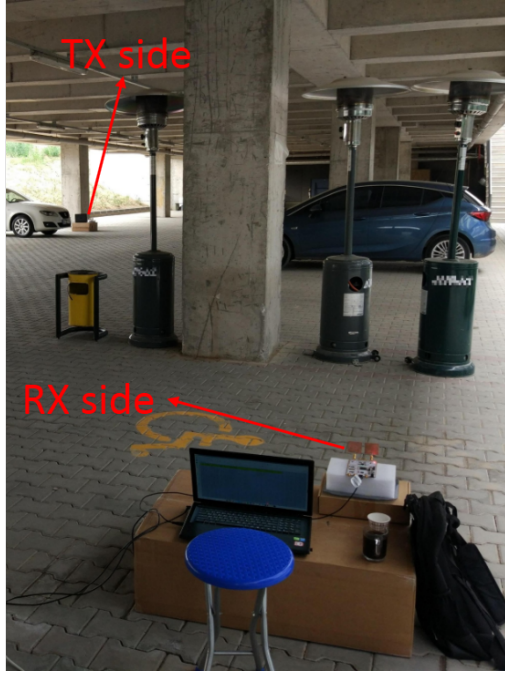
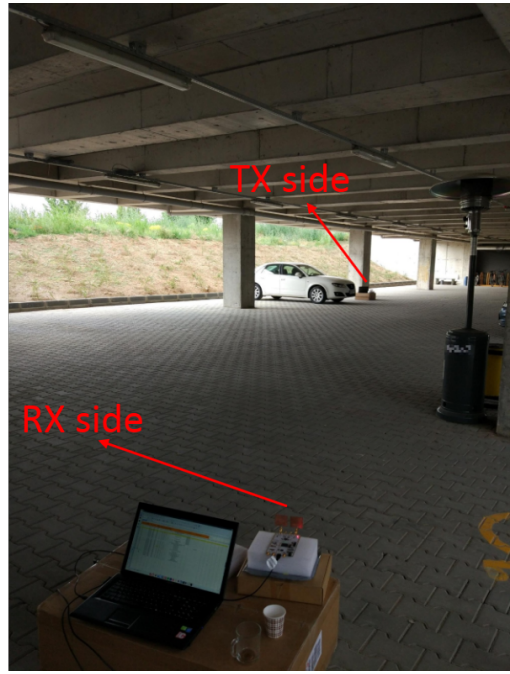


Figure 6.12: Dynamic and static channel capacity performance in the outdoor environment #2



(a) NLOS Condition



(b) LOS Condition

Figure 6.13: Outdoor test environment # 2: MIMO channel analysis tests for LOS and NLOS conditions

In the Test Environment #2, we changed the position of transmitter and took some measurements to show how MIMO performance is affected by LOS condition in the outdoor environment. For this purpose, we took two measurements that one is at LOS and the other is NLOS condition. Figure 6.13 shows our test setup in both channel conditions. In these test setups, only MIMO scenario was run and analysis results are given in Table 6.2. It is observed that MIMO is advantageous in the outdoor environment when the channel is in NLOS condition as expected. At the average SNR of 22.5 dB, EVM values for each stream is 9 dB better in NLOS compared to LOS condition. For the capacity comparison, NLOS is 3.3 b/s/Hz better on the average and this can be also understood from the channel matrix condition numbers ($\kappa(\mathbf{H}\mathbf{H}^H)$). In figures 6.14 and 6.15, snapshots are given from the testbed channel analysis GUI for the corresponding NLOS and LOS test measurements as an example.

Table6.2: Testbed channel analysis GUI results for the outdoor NLOS and LOS tests

Parameter (Average)	NLOS	LOS
SNR (dB)	22.5	
EVM ₁ (dB)	-16.5	-9.1
EVM ₂ (dB)	-18	-9.3
Capacity ($b/s/Hz$)	11.9	8.6
$\kappa(\mathbf{H}\mathbf{H}^H)$	9	245

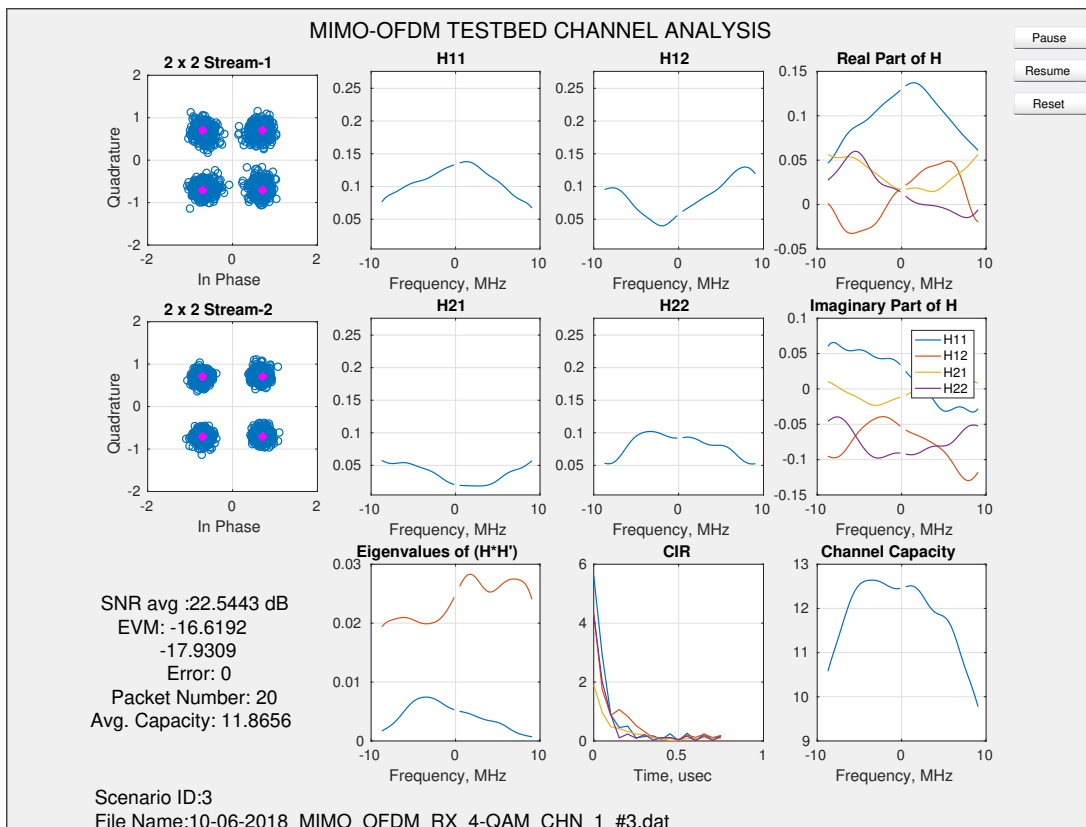


Figure 6.14: A snapshot from the testbed channel analysis GUI running 4-QAM 2×2 MIMO-OFDM outdoor NLOS scenario

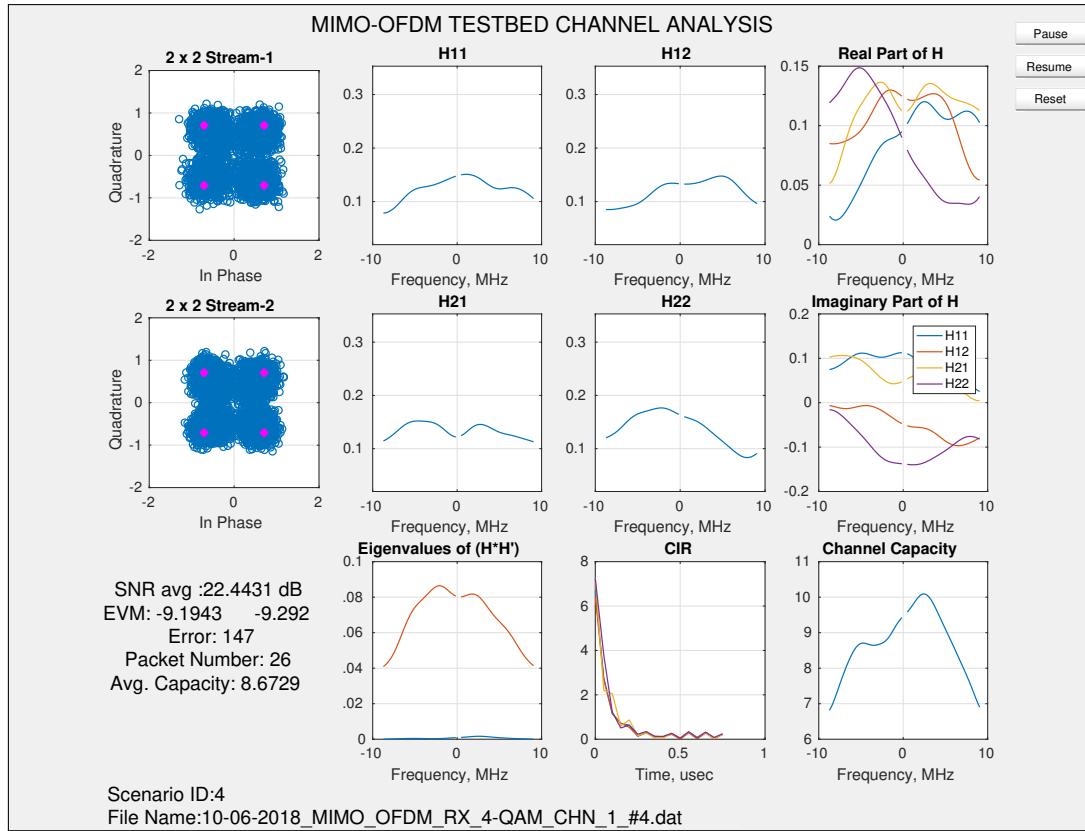


Figure 6.15: A snapshot from the testbed channel analysis GUI running 4-QAM 2×2 MIMO-OFDM outdoor LOS scenario

For the final measurement in the test environment #2, TX radio was left in the same place with that of our previous setup. We walked in a trajectory shown in Figure 6.17 with RX radio by taking measurements to show how the MIMO (2×2) channel matrix is effected. As seen from the plan, there is a closed garage area and a garden section in this test environment. The exterior of the building next to the garden is covered with windows and hence, it is expected that the channel will be highly scattered. Additionally, cars, walls and columns in the garage, trees in the garden and other objects will also increase the reflection in the environment together with the windows. We followed the points indicated by the numbers and proceeded to the building first, and then we completed the measurement by walking towards the stairs in parallel with the building. The yellow and red beams shown in the plan describes the direction of antennas during the measurement.

The performance of measured MIMO channel matrix is given in Figure 6.16 with computed condition numbers for $\mathbf{H}\mathbf{H}^H$. According to these results, it is observed

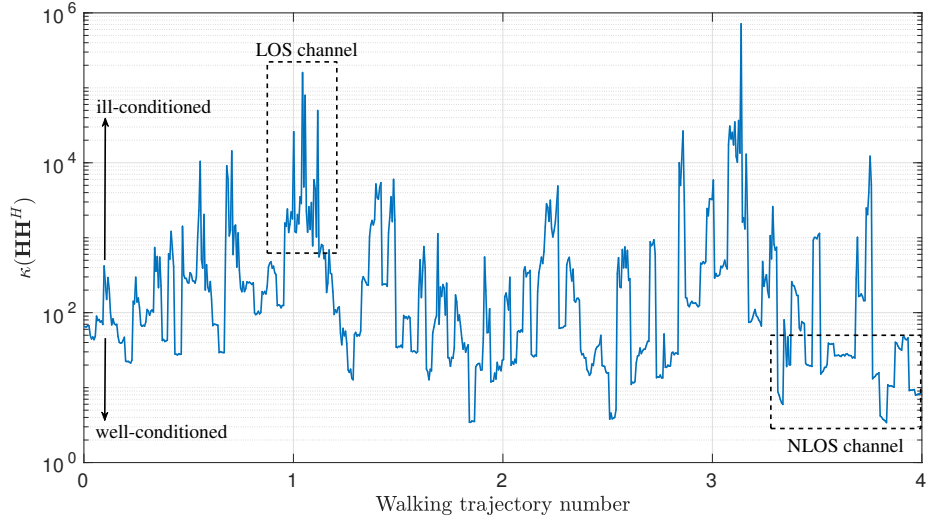


Figure 6.16: MIMO channel performance in the mobile measurement scenario

that the channel becomes ill-conditioned at where the antennas directly seeing each other as LOS condition, on the other hand it becomes well-conditioned at where the antennas looking at different directions and there are scattered objects in between creating an NLOS condition. Among all values, while the minimum value of κ is 3.5, the maximum becomes 3×10^5 . Also, we observe that the average κ value is around 80 hence it is more reliable to use SISO rather than MIMO in the most part of this walking trajectory.

6.2.3 Summary

2×2 MIMO channel analysis testbed study shows that in a rich scattered environment at 3.5 GHz, MIMO is advantageous in both indoor and outdoor scenarios with approximately 1.7 times capacity increase compared to SISO. In [66], 4×4 MIMO channel was analyzed with a 802.11a based OFDM testbed in an indoor environment at 5 GHz and it was shown that the capacity of 4×4 MIMO system is 3.4 times that of the SISO system which is similar to our findings for 2×2 MIMO configuration. Hence, based on the rich scattered NLOS measurement scenarios in this study, we observe good channel characteristics at 3.5 GHz for 2×2 MIMO systems. On the other hand, when the channel has a strong LOS characteristic, that is the $\kappa(\mathbf{HH}^H)$ is large, we observe that MIMO (with spatial multiplexing) is not advantageous. In

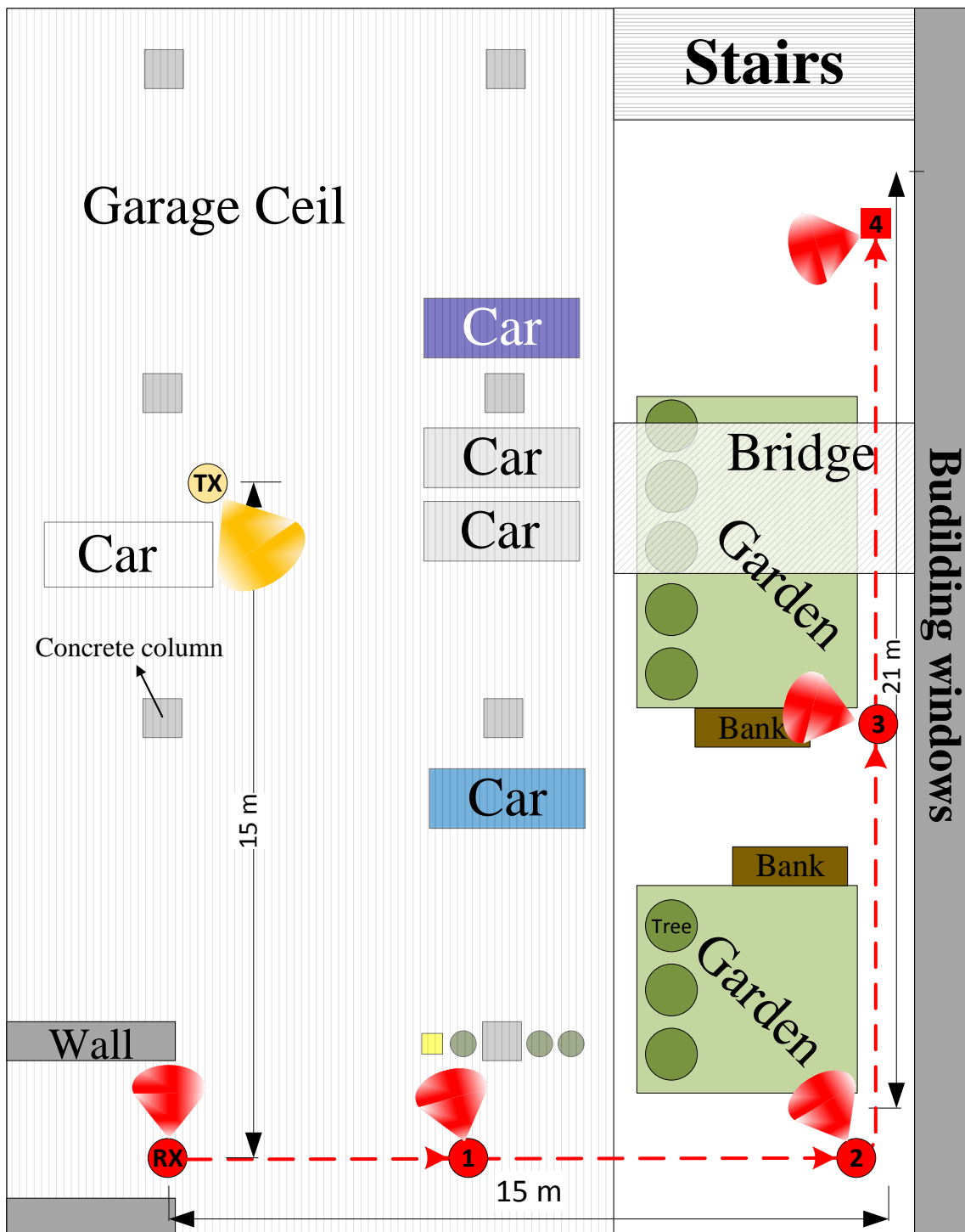


Figure 6.17: Outdoor environment # 2: Mobile measurement scenario walking trajectory plan

both indoor and outdoor environments, measured EVMs are much smaller compared to the NLOS case at the same average SNR value. In such cases, for a reliable communication, SISO is more advantageous than MIMO (with spatial multiplexing).

CHAPTER 7

SUMMARY, CONCLUSIONS AND FUTURE WORK

In this master's thesis, we study the physical layer design of MIMO-OFDM testbed data link system and its applications on SDR platform in 3.5 GHz.

In Chapter 2, we briefly summarize MIMO, OFDM and SDR technologies with their historical improvements and applications.

In Chapter 3, the physical layer design of our testbed data link is given. All signal processing blocks including transmitter and receiver structures are implemented in detail. On the receiver side, we propose various algorithms for frequency synchronization, channel estimation, equalization and detection operations. Additionally, we discuss their performance on MIMO-OFDM system.

In Chapter 4, to analyze our physical layer with various RF impairments and channel models, we present the implementation of the testbed data link simulator and its GUI software. The whole implementation process of our data link simulator and its GUI is given in a detailed manner. Also, simulations are performed for different application scenarios including SISO, MIMO for both coded and uncoded cases. We discuss the performance of SISO and MIMO scenarios under different channel conditions in terms of BER and diversity gains.

In Chapter 5, the implementation process of our testbed data link on SDR platform is presented.

In Chapter 6, Our testbed work is presented. We test our data link PHY in indoor and outdoor environments. In addition to data link tests, we also investigate the chan-

nel characteristics in SISO and MIMO scenarios in terms of channel capacity and condition number of the estimated MIMO channel matrix.

Within the scope of this thesis, the following important results are obtained:

- When designing a MIMO-OFDM data link system, it is vital to use cyclic shift diversity (CSD) for preamble part and rotated symbols for pilot subcarriers. By doing so, unintentional destructive beamforming is prevented on the receiver side and this increases the performance of MIMO-OFDM data link.
- For an OFDM system, fine estimation of the carrier frequency offset (CFO) in the frequency domain causes interference coming from non-orthogonal subcarriers due to CFO. Considering this fact, one should choose a fine estimator algorithm for your requirements. For our system, comparing CP based (in time) and pilot based (in frequency) estimators, pilot based estimators outperforms the other for our design criteria.
- For the channel estimation, we use the ML algorithm and increased the performance of ML by LS and TDT methods. Comparing both methods, ML+LS algorithm is used for our data link system in simulations and in SDR tests. Since we know that the performance is increased with ML+LS over ML in the simulations, it is also verified by testing our data link in SDR platform for a well synchronized MIMO-OFDM signal.
- We model some hardware impairments in our simulator such as residual RF impairments, phase noise, frequency offset, time delay and DC offset. Under those impairments, we compared the BER performance of OFDM system with theoretical results in Figure 4.7.
- In the simulations, we compare our data link in Rayleigh and Rician channel conditions for SISO and MIMO scenarios. We observe that MIMO performance degrades under Rician fading due to its LOS characteristics.
- In Figure 4.12, it is shown that transmitter side diversity gains for MIMO scenarios are obtained in MIMO-OFDM data link by channel coding with stream parsing operations. Also, in Figure 4.13, it is verified that receiver diversities are achieved by MIMO-ML detection.

- Our testbed data link system is successfully operated at indoor and outdoor environments in SISO and 2×2 MIMO scenarios at 3.5 GHz frequency band.
- Our testbed data link is also used for analyzing SISO and 2×2 MIMO channels in different environments at 3.5 GHz. From this tests:
 - We verify that MIMO is advantageous when channel is in NLOS condition for both indoor and outdoor environments.
 - We observe that the channel capacity of MIMO is approximately 1.7 times better than SISO in static measurements for our data link.
 - In a SISO/MIMO communication link, changing the position of radio on the order of wavelength results with a dramatical fluctuations on the channel capacity.
 - We show the performance of 2×2 MIMO channel by computing the condition number of estimated channel matrix ($\kappa(\mathbf{H}\mathbf{H}^H)$) in a mobile scenario. We observe that the channel characteristic is highly changing in this scenario and MIMO (with spatial multiplexing) is only advantageous when κ values are small.

In addition to the results obtained above, we consider some improvements to our study for future work. We can list those in below:

- We may improve our data link simulator by upgrading OFDM to new candidate waveforms (e.g. f-OFDM, FBMC, etc.) for 5G research studies.
- New algorithms can be implemented for channel estimation, frequency & time synchronization and we may compare their performance in our data link.
- We may add more hardware models (e.g. power amplifier, antenna coupling etc.) to the simulator so that simulations will produce results that are closer to the hardware tests.
- We can improve our testbed platform to some degree that analysis and measurements can be performed on-line rather than using recorded data.
- We can use different SDR devices (e.g. PicoSDR [67]) in order to improve our testbed for investigating 4×4 MIMO scenario with our data link structure.

REFERENCES

- [1] Internet Society. *Brief History of the Internet*. Retrieved from: <https://www.internetsociety.org/internet/history-internet/brief-history-internet/> [Accessed 25, Jul. 2018].
- [2] J. Nubarrón. *Evolution Of Mobile Technology: A Brief History of 1G, 2G, 3G and 4G Mobile Phones*. Bright Hub, December 1, 2011. Retrieved from: <https://www.brighthub.com/mobile/emerging-platforms/articles/30965.aspx> [Accessed 26, Jul. 2018].
- [3] Ye Li and Gordon L. Stüber. *Orthogonal Frequency Division Multiplexing for Wireless Communications*. Springer US, 1 edition, 2006.
- [4] E. Biglieri, R. Calderbank, A. Constantinides, A. Goldsmith, A. Paulraj, and H. V. Poor. *MIMO Wireless Communications*. Cambridge University Press, New York, NY, USA, 2007.
- [5] V. Tarokh, S. M. Alamouti, V. Koivunen, and K. Kim. MIMO-OFDM and its application. *Journal of Communications and Networks*, 9(2):109–111, June 2007.
- [6] LTE: Evolved universal terrestrial radio access (E-UTRA): Physical channels and modulation (3GPP TS 36.211 version 12.3.0 release 12). *ETSI TS 136 211 V12.3.0*, pages 1–126, 2014.
- [7] IEEE standard for information technology—telecommunications and information exchange between systems—local and metropolitan area networks—specific requirements—part 11: Wireless lan medium access control (MAC) and physical layer (PHY) specifications—amendment 4: Enhancements for very high throughput for operation in bands below 6 GHz. *IEEE Std 802.11ac(TM)-2013 (Amendment to IEEE Std 802.11-2012, as amended by IEEE Std 802.11ae-2012, IEEE Std 802.11aa-2012, and IEEE Std 802.11ad-2012)*, pages 1–425, Dec 2013.
- [8] F.-L. Luo and C. Zhang. *Major 5G Waveform Candidates: Overview and Comparison*, pages 616–. Wiley-IEEE Press, 2016.
- [9] R. W. Stewart, K. W. Barlee, D. S. W. Atkinson, and L. H. Crockett. *Software Defined Radio Using MATLAB & Simulink and the RTL-SDR*. Strathclyde Academic Media, UK, 2015.
- [10] M. Wenk. *MIMO-OFDM-testbed: challenges, implementations, and measurement results*. PhD thesis, 2010.
- [11] O. A. Nasr, O. Y. Takeshita, W. Zhu, and B. Daneshrad. Field trial results of a 4×4 MIMO-OFDM real time testbed. In *2010 IEEE International Conference on Communications*, pages 1–5, May 2010.

- [12] X. Lu, L. Ni, S. Jin, C. K. Wen, and W. J. Lu. Sdr implementation of a real-time testbed for future multi-antenna smartphone applications. *IEEE Access*, 5:19761–19772, 2017.
- [13] D. Nguyen. Implementation of OFDM systems using GNU Radio and USRP. Master’s thesis, 2013.
- [14] L. C. Tran, D. T. Nguyen, F. Safaei, and P. J. Vial. An experimental study of OFDM in software defined radio systems using GNU platform and USRP2 devices. In *2014 International Conference on Advanced Technologies for Communications (ATC 2014)*, pages 657–662, Oct 2014.
- [15] P. B. G. Baruffa, L. Rugini. Design and validation of a software defined radio testbed for DVB-T transmission. *Radioengineering*, 23(1):387–398, Apr. 2014.
- [16] Ettus Research. *USRP Hardware Driver and USRP Manual: USRP B2x0 Series*. Available at: http://files.ettus.com/manual/page_usrp_b200.html [Accessed 10, May 2018].
- [17] D. Goovaerts. *Nokia CTO confirms 3.5 GHz 5G launches on the way*. Available at: <https://www.mobileworldlive.com/latest-stories/nokia-cto-confirms-3-5ghz-5g-launches-on-the-way/> [Accessed 10, Jun. 2018].
- [18] R. Chang. Orthogonal frequency multiplex data transmission system. Jan. 6 1970. US Patent 3,488,445.
- [19] J. W. Cooley and J. W. Tukey. An algorithm for the machine calculation of complex fourier series. *Mathematics of Computation*, 19(90):297–301, 1965.
- [20] J. Wu and P. Fan. A Survey on High Mobility Wireless Communications: Challenges, Opportunities and Solutions. *IEEE Access*, 4(c):450–476, 2016.
- [21] N. Al-ghazu. A Study of the Next WLAN Standard IEEE 802 . 11ac Physical Layer, 2013.
- [22] E. Telatar. Capacity of multi-antenna gaussian channels. *European Transactions on Telecommunications*, 10(6):585–595, 1999.
- [23] G. J. Foschini. Layered space-time architecture for wireless communication in a fading environment when using multi-element antennas. *Bell Labs Technical Journal*, 1(2):41–59, Autumn 1996.
- [24] 3GPP. TS 136 211 - V14.2.0 - LTE; Evolved Universal Terrestrial Radio Access (E-UTRA); Physical channels and modulation (3GPP TS 36.211 version 14.2.0 Release 14). *ETSI*, 2017.
- [25] M. S. Gast. *802.11ac A Survival Guide*. 2013.
- [26] P. Johnson. New research lab leads to unique radio receiver. *E-Systems Team*, 4(4):6–7, 7 May 1985. Retrieved from: <http://chordite.com/team.pdf> [Accessed 29, Jul. 2018].
- [27] MathWorks. *MATLAB*. Available at: <https://www.mathworks.com/> [Accessed 10, Mar. 2018].

- [28] National Instruments. *LabVIEW*. Available at: <http://www.ni.com/en-tr/shop/labview.html> [Accessed 10, Mar. 2018].
- [29] GNU Radio. *GNU Radio Manual and C++ API Reference v3.7.10.1*, 2016. Available at: <https://www.gnuradio.org/doc/doxygen/> [Accessed 12, Jan 2018].
- [30] RTL-SDR. *ADALM-PLUTO SDR: Unboxing and Initial Testing*, August 16, 2017. Retrieved from: <https://www rtl-sdr.com/tag/gnuradio/> [Accessed 20, Feb 2018].
- [31] C. H. Yih. Analysis and compensation of DC offset in OFDM systems over frequency-selective rayleigh fading channels. *IEEE Transactions on Vehicular Technology*, 58(7):3436–3446, Sept 2009.
- [32] J. K. Bisla, N. Dhillon, and K. Sharma. Performance Evaluation of Punctured Convolutional Codes for OFDM-WiMAX System 1. 2(3):142–148, 2014.
- [33] Chia-Horng Liu. On the Design of OFDM Signal Detection Algorithms for Hardware Implementation. *GLOBECOM '03. IEEE Global Telecommunications Conference (IEEE Cat. No.03CH37489)*, 2(2):596–599, 2003.
- [34] C. E. Hajjar. *Synchronization Algorithms for OFDM Systems (IEEE802. 11a, DVB-T)*. PhD thesis, 2007.
- [35] T. M. Schmidl and D. C. Cox. Robust frequency and timing synchronization for OFDM. *IEEE Transactions on Communications*, 45(12):1613–1621, 1997.
- [36] Z. Liu and K. Yi. Symbol Timing Synchronization Using Interpolation-Based Matched-Filters. *Wireless Personal Communications*, 50(4):457–467, 2009.
- [37] M. García and C. Oberli. Intercarrier interference in OFDM: A general model for transmissions in mobile environments with imperfect synchronization. *EURASIP Journal on Wireless Communications and Networking*, 2009(1):786040, Nov 2009.
- [38] C. E. Hajjar. *Synchronization Algorithms for OFDM Systems (IEEE802. 11a, DVB-T)*. PhD thesis, 2007.
- [39] A. N. Mody and G. L. Stuber. Synchronization for MIMO OFDM systems. In *Global Telecommunications Conference, 2001. GLOBECOM '01. IEEE*, volume 1, pages 509–513 vol.1, 2001.
- [40] Q. Cheng. Performance study of residual carrier frequency offset estimation methods in OFDM WLAN systems. *Digital Signal Processing*, 2(3):981 – 993, 2013.
- [41] P. K. Nishad. Carrier frequency offset estimation in MIMO-OFDM systems. Master's thesis, National Institute of Technology Rourkela, 2013.
- [42] J. J. van de Beek, M. Sandell, and P. O. Borjesson. ML estimation of time and frequency offset in OFDM systems. *IEEE Transactions on Signal Processing*, 45(7):1800–1805, Jul 1997.

- [43] P. H. Moose. A technique for orthogonal frequency division multiplexing frequency offset correction. *IEEE Transactions on Communications*, 42(10):2908–2914, Oct 1994.
- [44] C. H. Lin, R. C. H. Chang, K. H. Lin, and Y. Y. Lin. Implementation of channel estimation for MIMO-OFDM systems. In *2010 International SoC Design Conference*, pages 99–102, Nov 2010.
- [45] I. T. Lu and K. J. Tsai. Channel estimation in a proposed IEEE802.11n OFDM MIMO WLAN system. In *2007 IEEE Sarnoff Symposium*, pages 1–5, April 2007.
- [46] V. D. Nguyen, H. P. Kuchenbecker, and M. Patzold. Estimation of the channel impulse response length and the noise variance for OFDM systems. In *2005 IEEE 61st Vehicular Technology Conference*, volume 1, pages 429–433 Vol. 1, May 2005.
- [47] A. Goldsmith. *Wireless Communications*. Cambridge University Press, 2005.
- [48] S. G. Kim, D. Yoon, S. K. Park, and Z. Xu. Performance analysis of the MIMO zero-forcing receiver over continuous flat fading channels. In *The 3rd International Conference on Information Sciences and Interaction Sciences*, pages 324–327, June 2010.
- [49] A. F. Molisch. *Wireless Communications*, chapter 16, page 348. 2 edition, 2011. Figure: Illustration of noise enhancement in zero-forcing equalizer (a), which is mitigated in an MMSE linear equalizer (b).
- [50] A. A. Hasan and I. D. Marsland. Low complexity LLR metrics for polar coded QAM. In *2017 IEEE 30th Canadian Conference on Electrical and Computer Engineering (CCECE)*, pages 1–4, April 2017.
- [51] X. Guo and X. G. Xia. On full diversity space-time block codes with partial interference cancellation group decoding. *IEEE Transactions on Information Theory*, 55(10):4366–4385, Oct 2009.
- [52] A. Viterbi. Error bounds for convolutional codes and an asymptotically optimum decoding algorithm. *IEEE Transactions on Information Theory*, 13(2):260–269, April 1967.
- [53] B. Moision. A truncation depth rule of thumb for convolutional codes. In *2008 Information Theory and Applications Workshop*, pages 555–557, Jan 2008.
- [54] C. Studer, M. Wenk, and A. Burg. MIMO transmission with residual transmit-RF impairments. In *2010 International ITG Workshop on Smart Antennas (WSA)*, pages 189–196, Feb 2010.
- [55] N. J. Kasdin. Discrete simulation of colored noise and stochastic processes and 1/f alpha; power law noise generation. *Proceedings of the IEEE*, 83(5):802–827, May 1995.
- [56] G. M. Guvensen and A. O. Yilmaz. A general framework for optimum iterative blockwise equalization of single carrier MIMO systems and asymptotic performance analysis. *IEEE Transactions on Communications*, 61(2):609–619, February 2013.

- [57] H. feng Lu and P. V. Kumar. Rate-diversity tradeoff of space-time codes with fixed alphabet and optimal constructions for psk modulation. *IEEE Transactions on Information Theory*, 49(10):2747–2751, Oct 2003.
- [58] V. Tarokh, N. Seshadri, and A. R. Calderbank. Space-time codes for high data rate wireless communication: performance criterion and code construction. *IEEE Transactions on Information Theory*, 44(2):744–765, Mar 1998.
- [59] C. Mu-Hyun. *South Korea’s 5G spectrum auction to start at \$3 billion.* Available at: <https://www.zdnet.com/article/south-koreas-5g-spectrum-auction-to-start-at-3-billion/> [Accessed 12, Jun. 2018].
- [60] S. Kinney. *Qualcomm, Nokia test 5G in the 3.5 GHz and 28 GHz bands.* Available at: <https://www.rcrwireless.com/20180207/5g/qualcomm-nokia-test-5g-tag17> [Accessed 13, Jun. 2018].
- [61] Analog Devices. *RF Agile Transceiver*, AD9361 data sheet, 2013. Rev. F.
- [62] Xilinx. *Spartan-6 FPGA*, XC6SLX150 data sheet, 2011. v2.0.
- [63] A. Mandal, A. Ghosal, A. Majumdar, A. Ghosh, A. Das, and S. K. Das. Analysis of feeding techniques of rectangular microstrip antenna. In *2012 IEEE International Conference on Signal Processing, Communication and Computing (ICSPCC 2012)*, pages 26–31, Aug 2012.
- [64] Anketek A.Ş. Founded in 2012. Available at: <http://www.anketek.com.tr/> [Accessed 27, Apr. 2018].
- [65] Rogers Corporation. *High Frequency Circuit Material*, RO4003 data sheet,.
- [66] K. Mizutani, K. Sakaguchi, J. ichi Takada, and K. Araki. Development of MIMO-SDR platform and its application to real-time channel measurements. *IEICE Transactions*, 89-B:3197–3207, 2006.
- [67] Nutaq. *PicoSDR 4 × 4*, 2018. Available at: <https://www.nutaq.com/picosdr4x4> [Accessed 22, Jul. 2018].

